Electromagnetic Field Computation and Photonic Band Gap Devices

by

Jerry Chia-yung Chen
B.S.E., Electrical Engineering & Computer Science, Princeton U. (1989)
S.M., Electrical Engineering & Computer Science, M.I.T. (1991)
E.E., Electrical Engineering & Computer Science, M.I.T. (1995)

Submitted to the Department of Electrical Engineering and Computer Science
in partial fulfillment of the requirements for the degree of

Doctor of Philosophy in Electrical Engineering

at the

MASSACHUSETTS INSTITUTE OF TECHNOLOGY

February 1996

Author .....
Department of Electrical Engineering and Computer Science
January 1996

Certified by .....
Hermann A. Haus
Institute Professor
Thesis Supervisor

Certified by .....
John D. Joannopoulos
Professor of Physics
Thesis Supervisor

Accepted by .....
Prof. Frederick R. Morgenthaler
Chairman, Departmental Committee on Graduate Students

Electromagnetic Field Computation and Photonic Band Gap Devices

by

Jerry Chia-yung Chen

B.S.E., Electrical Engineering & Computer Science, Princeton U. (1989)

S.M., Electrical Engineering & Computer Science, M.I.T. (1991)

E.E., Electrical Engineering & Computer Science, M.I.T. (1995)

Submitted to the Department of Electrical Engineering and Computer Science
on January 1996, in partial fulfillment of the
requirements for the degree of
Doctor of Philosophy in Electrical Engineering

Abstract

The increasing demand for high-speed telecommunications requires the design of improved integrated optical components. The variety and complexity of optical waveguides often does not allow for closed-form analytical treatment. Thus, numerical techniques are very important in determining device characteristics. In this thesis, we will focus on the generalization and optimization of eigenmode calculations and on the design and characterization of photonic band gap resonators and filters.

Thesis Supervisor: Hermann A. Haus
Title: Institute Professor

Thesis Supervisor: John D. Joannopoulos
Title: Professor of Physics

Acknowledgments

First of all, I would like to thank my advisor Prof. Hermann Haus. I appreciate his wisdom, ideas, guidance, support, and encouragement over the many years. He is, not only a brilliant scientist, but also a nice guy. Thanks! I have also enjoyed working for Prof. John Joannopoulos. He asks good questions and has good ideas. And I think he genuinely cares for his students. He has a special place in my heart. Prof. Erich Ippen is friendly and hospitable. I appreciate also his intuition and curiosity. I am grateful to all three professors for the opportunities of working in their groups! It was educational.

I also thank Prof. Leslie Kolodziejski for being a thesis reader. Her comments have improved this thesis.

To do the work in this thesis required the assistance of many people. With the beam propagation and eigenmode work, I enjoyed collaborating with Dr. Stephan Jüngling. Thanks for your friendship, the MATLAB tricks, and the lunches! Prof. Chulhun Seo is also a sympathetic and kind-hearted friend, who helped with the bending loss chapter. Dr. Karl Kissa at Draper Labs introduced me to beam propagation methods (BPM). Thanks for the summer job! I am grateful to Prof. Wei-ping Huang and Dr. Chenglin Xu for letting me use the kernel of their BPM program. It was very helpful.

Concerning photonic band gaps, Shanhui Fan and Dr. Bob Meade has taught me stuff on band gap theory and frequency domain methods. They are smart and prolific. I also applaud Dr. Pierre Villeneuve's work on 3D air bridges and Ilya Kurland's and Attila Mekis' investigations into 2D micro bends. Josh Winn wrote part of the scalar-like finite difference time domain (FDTD) program. Kevin Li wrote the perfectly matched layer FDTD code. I benefited from discussions on FDTD methods with Kevin and Dr. Robert Shin. I also enjoyed learning more about fabrication issues from Paul Martin, Ed (K.-Y.) Lim, Jay Damask, and Jee-hoon Yap Krska. Constantine (Costas) Tziligakis, Siegfried Fleischer, and Dave Dougherty challenged me to think about how to coupling light from their optical parametric oscillator

(OPO) to the air bridge. Dr. Brent Little helped with his analytic mode solver. Mr. Ken Jones of Thinking Machines gave suggestions on how to use the CM-5's CMAX program.

Dave Foss provided a 10 Mb/s internet drop for my HP workstation and a nice corner in the RLE terminal room. I also appreciate his advice and friendliness. Our super-secretary/artist, Cindy Kopf, helped draw a few figures. Dr. Kurt Schlager of TRW introduced me to his large bibtex file with countless FDTD references. I am grateful to the electrical engineering department (ECF) for giving our group disk space and for loaning me a computer table. This research also benefited from free supercomputer time at Cornell Theory Center (IBM ES 9000), M.I.T. Laboratory of Computer Science (TMC CM-5), Pittsburgh Supercomputer Center (Cray C90), and San Diego Supercomputer Center (Cray C90). And I am grateful to Office of Naval Research Fellowship, NSF 9012787-ECS, NSF DMR 90-22933, NSF DMR 94-00334, ARO DAAH04-93-G-0262, etc. for funding my research assistantship.

My office mate Farzana Khatri has been a good friend. She has advised me wisely, proofread my papers, and listened to my harangues. I enjoyed our conversations, emails, and dinners. I am going to miss her. Kohichi Tamura has also given advice, support, and encouragement. He reminds me of what is truly important. Thanks! Shu Namiki has blessed me with his hospitality, kindness, and wisdom. I enjoyed our discussions on job hunting, company life, and research directions. I enjoyed chatting to Siegfried Fleischer; he has good insights and programs C++ well. William Wong is a friendly and nice person, who inspires me to work harder. I appreciate John Moores' sense of humor. Here's to buffets, Cornell, and movies! Dave Dougherty and Charlie Hultgren also have a nice sense of humor; keep smiling! I appreciate Pat Chou's advice on AT&T. With Charles Yu I have had nice conversations. Gadi Lenz gives nice explanations of physical phenomena. And to the rest of the Optics Group, thanks! You have made graduate school more fun.

I am grateful to my friends at MIT's Chinese Christian Fellowship. In a sense, they have been a family away from home. My apartment-mate Tim Chow has given me emotional support, thought-provoking debates, and his friendship. Marilyn Chen

gives wise counsel and helpful encouragement. She is also a great listener. I appreciate Jeff Kuo's loyalty, prayers, and friendship! I enjoyed long talks and prayers with Tom Wang. Leigh Lien is my favorite psychiatrist; I enjoy our zwrite's. I also appreciate countless emails and letters from Stephanie Sung and Eric Birgbauer. Kevin Lee is supportive and encouraging. I enjoyed serving and chatting with Peter Huang, Carl Lim, Sam Leung, Melissa Lee, and Phil Lin. I will also remember the phone calls and dinners with Eric Won, Janet Tseng, Bonnie Ky, and Alice Liu. At Boston Chinese Evangelical Church I also met many non-MIT friends. Clara Chang is very supportive, kind-hearted, and sweet. I love talking to her. Walton Yuen provided great support; I miss praying with him, Tom and John. I also enjoyed Kenny Eng's small group; the people were friendly. I enjoyed phone calls and emails with Connie Lee, Adrian Hebard, Vivian Chin, Charlene Tong, Steve Lee, Adina Ho, and many others. I also enjoyed serving with the other leaders of Koinonia/ Oasis (the young adults group) and United Christian R/O (the MIT Christian "welcome wagon"). Thanks for making Boston a more friendly place!

I am grateful to my family for their love, support, and encouragement. They have helped make life more worthwhile. My parents have been a great help and role model. And my sister Teresa is my best friend. They mean a lot to me!

Finally, I would like to thank God. To me, He is "the Alpha and the Omega, the First and the Last, the Beginning and the End" (Revelations 22:13, Bible).

Contents

List of Figures

Chapter 1

Introduction

National data highway, interactive television, video on demand, massively parallel computers, and multimedia — these are some of today's buzzwords. Conceivably in the future, cable companies will offer over 500 channels to individual homes. Pay-per-view TV will offer movies, supplanting video rental stores. The more intellectually curious can use the internet to read books from electronic libraries and find facts from distant databases. Terminals will display more and more graphics, rather than text. Phones can send videos as well as voices. Most likely, the first tera-flop computer will not be a conventional vector supercomputer, but a parallel computer, where tasks are distributed among hundreds of processors. The rate data moves between these processors affects the parallel computer overall speed. All these trends depend on high capacity communication links.

How can today's telecommunications networks support these emerging technologies? Will optical fiber rise to the challenge? One possible solution, Time Division Multiplexing (TDM), maximizes the use of a given high speed link. In this scheme, several slower data streams are combined into one fast one. Since networks faster than 20 giga-bits per second (Gb/s) are difficult to make, researchers are now trying to place more than one data channel on a given fiber link. In Wavelength Division Multiplexing (WDM), these channels are differentiated by wavelength or color. Whether TDM or WDM or any other scheme is used, further advances are needed in optical devices — the fundamental building blocks of networks.

Optical devices send, receive and process data. Typical components are semiconductor lasers, optical amplifiers, tunable filters, detector arrays, fast switches, and directional couplers. As the performance of these devices increases, the cost of fabricating them usually rises. Consequently, the advantages of modeling and designing prototypes on computers become more and more apparent. This thesis focuses on computer modeling of optical devices, concentrating on beam propagation techniques and photonic band gap materials.

1.1 Beam Propagation Method

The Beam Propagation Method (BPM) solves the paraxial wave equation

$$2jkn_0\frac{\partial E}{\partial z} = \frac{\partial^2 E}{\partial x^2} + \frac{\partial^2 E}{\partial y^2} + k^2\left[n(x,y,z)^2 - n_0^2\right]E, \tag{1.1}$$

where $E(x,y,z)$ is the envelope of the field[1] distribution, z is the propagation direction, x and y are the transverse dimensions, k is the free space wave vector, and n_0 is the effective index. kn_0 equals k_z — the z component of the envelope's propagation constant. The paraxial wave equation comes from substituting the field $E(x,y,z)e^{-jkn_0z}$ into the Helmholtz or wave equation

$$\left[\frac{\partial^2}{\partial x^2} + \frac{\partial^2}{\partial y^2} + \frac{\partial^2}{\partial z^2} + k^2 n(x,y,z)^2\right]\left(Ee^{-jkn_0z}\right) = 0.$$

The Helmholtz equation is in the frequency domain so assumes single frequency or CW light. The assumptions behind paraxial wave equation (1.1) are:[2]

1. Paraxial approximation: the electromagnetic waves propagate in directions not far away from a reference axis z (waveguide axis);

2. Scalar approximation: all polarization effects are neglected.

[1] electric and magnetic fields in a scalar sense, neglecting polarization

[2] Thanks to Prof. Wei-ping Huang for listing these approximations

3. One-way approximation: the electromagnetic waves propagate unidirectionally, i.e., the reflections due to the index discontinuities along the waveguide axis are neglected;

4. Isotropic non-magnetic medium: the medium is described by $\epsilon = \epsilon(x, y, z)$ and $\mu = \mu_o$.

Compared to Maxwell's equations, the paraxial wave equation has some advantages. For example, the paraxial wave equation is first order with respect to z. So, if one specifies the fields at one transverse plane (such as $z = 0$), $E(x, y, 0)$, the BPM can calculate the fields at a neighboring plane $z = \Delta z$. Then from $E(x, y, \Delta z)$ BPM calculates $E(x, y, 2\Delta z)$. This process repeats until all other desired points are calculated. Since an $e^{-jkn_0 z}$ envelope with large sinusoidal oscillations is factored away, the remaining amplitude E is a slowly varying function of z. With a careful choice of n_0, E changes very little with z. As a result, these small changes can be described by a few points separated by large step sizes Δz. As a result, BPM is computationally very efficient. BPM can be run on personal computers. It is the standard numerical method for modelling guided wave optics. And in the last few years, many commercial BPM packages have been introduced. BPM has been used to calculate the propagation (specifically, transmission and dissipation) of light in 2D and 3D waveguides of arbitrary indices.

The term BPM was first applied to solutions of equation (1.1) using Fast Fourier Transforms (FFTs)[1] but recently the term has also described finite difference (FD)[2] and finite element (FEM)[3] implementations. FFT based ones were the "method of choice" in the 70's.[3] However, in the 80's finite difference was favored. Finite difference can model a waveguide's index discontinuities accurately, without Gibbs oscillations. Finite elements has the advantage of modelling waveguides that can not be decomposed into rectangles accurately (such as fibers). But this method does not have as large a following. FEM is harder to code. This thesis focuses on the popular

[3]I feel that FFT is the best method for modelling more gradual index changes such as those associated with nonlinearities like n_2.

finite difference implementation.

As BPM has became more popular, scientists have proposed some clever extensions. By assuming the spatial index profiles are piecewise constant, M. S. Stern has incorporated some polarization dependence. He calls his new scheme the semi-vectorial approximation.[4] W. P. Huang *et al.*[5] show that this approximation includes all the terms of the vector wave equation but neglects cross polarization terms. The governing equations are

$$j\frac{\partial \hat{E}_x}{\partial z} = \frac{1}{2n_o k}\left\{\frac{\partial}{\partial x}\left[\frac{1}{n^2}\frac{\partial}{\partial x}(n^2\hat{E}_x)\right] + \frac{\partial^2}{\partial y^2}\hat{E}_x + (n^2 - n_o^2)k^2\hat{E}_x\right\}$$

$$j\frac{\partial \hat{E}_y}{\partial z} = \frac{1}{2n_o k}\left\{\frac{\partial}{\partial y}\left[\frac{1}{n^2}\frac{\partial}{\partial y}(n^2\hat{E}_y)\right] + \frac{\partial^2}{\partial x^2}\hat{E}_y + (n^2 - n_o^2)k^2\hat{E}_y\right\}$$

for the electric fields and

$$j\frac{\partial \hat{H}_x}{\partial z} = \frac{1}{2kn_o}\left\{n^2\frac{\partial}{\partial y}\left(\frac{1}{n^2}\frac{\partial \hat{H}_x}{\partial y}\right) + \frac{\partial^2 \hat{H}_x}{\partial x^2} + (n^2 - n_o^2)k^2\hat{H}_x\right\}$$

$$j\frac{\partial \hat{H}_y}{\partial z} = \frac{1}{2kn_o}\left\{n^2\frac{\partial}{\partial x}\left(\frac{1}{n^2}\frac{\partial \hat{H}_y}{\partial x}\right) + \frac{\partial^2 \hat{H}_y}{\partial y^2} + (n^2 - n_o^2)k^2\hat{H}_y\right\}$$

for the magnetic fields.

In 1991, G. R. Hadley proposed the transparent boundary condition.[6,7] This assumes the second derivative of the fields normal to the computational domain edge are zero. By allowing nonzero fields at the edge, this boundary condition in practice reduces the domain size and improves the model fidelity. Previously, the fields at the edges of the computational domain were set to zero. Or periodic boundary conditions were employed. Some have pointed out that transparent boundaries can lead to instabilities.[8,9]

For a given step size Δz, the BPM methods solves (1.1) accurately for a small range of effective indices near n_0. This limits the propagation vectors to a small angular range.[4] To widen this range, researchers have proposed so-called "wide-

[4]Explanation: The magnitude of the wave vector is fixed at kn. Since its projection on the z axis is limited to a small range near kn_0, the range of angles is also small.

angle" extensions.[10–13] These methods add higher order terms that were considered negligible when deriving the paraxial wave equation.

P. Kaczmarski and P. E. Lagasse do not neglect back reflections. They model these reflections by running the BPM program in reverse. This bidirectional BPM[14,15] is models non resonant reflections admirably. Resonant reflections would require many BPM runs. A recent journal article[16] compares some of the fancier BPM programs.

The program described in this thesis solves the paraxial wave equation with the finite difference method in 3D spatial dimensions. It has the semi-vectorial extension and the transparent boundary condition. The kernel of this code came from Prof. Wei-Ping Huang's group at U. of Waterloo. This code solves the large sparse matrix associated with FD-BPM by ORTHOMIN.[17] To this code, I have changed the boundary conditions to allow for 1) $E = 0$, 2) normal derivative equals zero, and 3) periodic. In addition, we have built the user interface and analysis routines.

1.2 Eigenmodes from beam propagation

Normally, BPM has been used to calculate the propagation (specifically, transmission and dissipation) of light in 2D and 3D waveguides of arbitrary indices. But BPM can also be used to find the eigenmodes of a structure. For example, if at every BPM step, one calculates the overlap integral of the just-obtained field $E(x, y, x)$ with the initial field $E(x, y, 0)$, the peaks of the Fourier transform lie at the propagation constants of the transverse modes.[18] If one repropagates and beats with a propagation constant, one can extract the field distribution corresponding to that propagation constant.[19] If the BPM is implemented with finite difference or finite element, the eigenvalues and eigenvectors of the matrix, resulting from the discretization of the paraxial wave equation, are the propagation constants and eigenmodes of the waveguide. This linear system has been solved with the shifted inverse power method.[4,20] The Fast Fourier Transform also has been used to calculate the Green's function matrix.[21] The Lanczos method can speed up the calculation by reducing the size of the matrix.[22] These matrix methods can produce waveguide modes efficiently.

Recently, Yevick and Hermansson[23] showed that propagation along the imaginary axis can give the fundamental mode and its effective index quite efficiently. This method is quite general. It can calculate the mode of a lossless waveguide of arbitrary geometry and composition. Also, it applies not only to finite difference and finite element BPM but also to FFT BPM. The foundations of imaginary-distance propagation were laid when Yevick and Hermansson[24] suggested that BPM applied to the imaginary axis can give the fundamental mode of an optical waveguide. The fundamental mode has the largest propagation constant and thus experiences the most rapid oscillations in phase when traveling down the real axis. Propagation down the imaginary axis changes these sinusoidal variations in phase into exponential growths in amplitude. A sufficiently long imaginary propagation gives the fundamental mode — the mode with the most growth. Hawkins[25] related this imaginary-distance propagation of optical beams to the path integral formalism of quantum mechanics. Yevick and Hermansson applied this concept to the beam propagation method[23] and related it to variational techniques.[26] Jüngling *et al.* has extended this formalism to active waveguide devices.[27] Applying the imaginary-distance propagation technique, Xu *et al.*[28] obtained vector field modes and studied the effect of transverse grid sizes. Since fine meshes tend to be computationally intensive, Yevick and Hermansson[23] start with a coarse mesh. After few propagation steps, they refine the mesh in the transverse direction.

But to our knowledge, other groups have not considered the effect of the step size in the propagation direction. In chapter 2 we present a systematic study of all the input parameters. We formulate the first and only analytic model[9] that describes how these input parameters affect the method's stability and convergence. Using this model, we present two parameter sets that minimizes computer time significantly.[29] The accuracy of this analytic model has been verified by many computer runs.[9]

Though imaginary distance beam propagation method is a useful technique for calculating the fundamental mode, but sometimes information on higher order modes is desired. For example, knowledge of the second lowest mode tells whether the structure is single-moded or not. Yevick and Hermansson suggest the possibility of

obtaining higher order modes by applying the Prony method[24,21] but to our knowledge, they have not presented a numerical implementation of the Prony technique. Chapter 3 proposes and demonstrates another method — the power method — to calculate higher order waveguide modes.[30,31]

1.3 Finite Difference Time Domain

The Finite Difference Time Domain (FDTD) method is a general method, because it integrates Maxwell's equations

$$\nabla \times E = \mu \frac{\partial H}{\partial t} \tag{1.2}$$

$$\nabla \times H = \epsilon \frac{\partial E}{\partial t}. \tag{1.3}$$

If the fields are invariant or constant in the z direction, these equations reduce to

$$\begin{aligned} \frac{\partial E_z}{\partial y} &= \mu \frac{\partial H_x}{\partial t} \\ -\frac{\partial E_z}{\partial x} &= \mu \frac{\partial H_y}{\partial t} \\ \frac{\partial H_y}{\partial x} - \frac{\partial H_x}{\partial y} &= \epsilon \frac{\partial E_z}{\partial t} \end{aligned}$$

for TE[5] fields and

$$\begin{aligned} \frac{\partial H_z}{\partial y} &= \epsilon \frac{\partial E_x}{\partial t} \\ -\frac{\partial H_z}{\partial x} &= \epsilon \frac{\partial E_y}{\partial t} \\ \frac{\partial E_y}{\partial x} - \frac{\partial E_x}{\partial y} &= \mu \frac{\partial H_z}{\partial t} \end{aligned}$$

for TM[6] fields. Note the duality between E and H and between ϵ and μ.

The finite difference method divides the computational domain into rectangular

[5]Here, TE implies that the electric field E_z is normal to propagation direction
[6]Here, TM implies that the magnetic field H_z is normal to propagation direction

grids. For second order accuracy in the derivatives, E and H fields are displaced by half grid points in both space and time. This Lax-Windroff or Leapfrog geometry[7] has been applied to Maxwell's equations in 1966 by Yee.[34] Given electric and magnetic fields at an initial time, the FDTD program updates the fields, advancing the values forward in time. This algorithm is very efficient as only three fields need to be stored. It is also explicit in the sense that the latest time step depends only on previous time steps (not itself), so it is well suited for parallel computers.[35] But explicit schemes tend to be unstable if the time steps are too large.[8] The maximum time step is limited by the Courant-Friedrichs-Lewy (CFL) condition,[33]

$$\Delta T \leq 1/(|v|\sqrt{\Delta x^{-2} + \Delta y^{-2} + \Delta z^{-2}}) \tag{1.4}$$

where $|v|$ is the maximum phase velocity[9]

Although the FDTD method is accurate and general, it does have some limitations or built-in approximations. For example, many try to model unbounded geometries with a finite domain. The representation of these open boundary conditions tends to be approximate.

The most widely method, the Absorbing Boundary Condition (ABC), permits waves to leave the computational domain but "absorbs" the incoming waves. Mathematically, this can be represented by the one way wave equation. In operator form, this equation is

$$\frac{n}{c}\partial_{xt} - \frac{n^2}{c^2}\partial_t^2\partial_x - \frac{n}{c}\partial_t\sqrt{1 - \left(\frac{c\,\partial_y}{n\,\partial_t}\right)^2} = 0 \tag{1.5}$$

where $\partial_x = \frac{\partial}{\partial x}$ is the derivative operator with respect to x, n is the index of refraction and c is the speed of light in vacuum. This equation applies to fields hitting the boundary x = constant. Generalizations to the y = constant and to three dimen-

[7] Books by Ames[32] and Press *et al.*[33] describe this geometry in more detail.

[8] As a point of comparison, most BPM codes use the Crank-Nicholson scheme to advance forward in z. This scheme is implicit permitting large Δz steps, although at the expense of greater storage requirements.

[9] In our case, $|v| = c$ and $\Delta z = 0$.

sions are straight-forward. First order Taylor expansion of the square root[10] leads to Enquist and Majda's second order ABC,[37]

$$\frac{n}{c}\partial_{xt} - \frac{n^2}{c^2}\partial_t^2 + \frac{1}{2}\partial_y^2 = 0. \tag{1.6}$$

If the propagation direction is normal to x, the above equation simplifies to the first order ABC.

$$\partial_x - \frac{n}{c}\partial_t = 0.$$

For vector FDTD, Mur[38] uses one of Maxwell's curl equations $\mu\partial_t H_x = -\partial_y E_z$ to simplify (1.6) to

$$\frac{\partial E_z}{\partial x} - \frac{n}{c}\frac{\partial E_z}{\partial t} - \frac{c\mu}{2n}\frac{\partial H_x}{\partial y} = 0.$$

These waves incident on the ABC suffer from unwanted back reflections. These reflections tend to be very low for waves near normal incidence but can be severe for other angles. Higdon[39] have tried to tailor the ABC for other angles. Trefethen and Halpern[40] and Blaschak[41] have tried to expand the square root in (1.5) in more accurate ways, using Padé, least squares, Chebyshev, and Newman points. In this, Lindman[42] did some of the pioneering work. Expansion of that square root to fifth order have been reported[43] but these higher order schemes tend to suffer from instabilities.[44] One popular scheme — Mei and Fang's superabsorbing boundary condition[45] — improves the second order Mur ABC by canceling out a higher order error term. Researchers have also applied the concept of one-way wave equations to cylindrical and spherical coordinates.[46,47] Bringing the boundary condition right to the scattering object has been called on-surface radiation condition (OSRC);[48] this OSRC is particularly popular in FEM.

Last year, Berenger[49] introduced a new boundary condition, Perfectly Matched Layers (PML). Compared to ABC and OSRC, PML reduces spurious reflections by *orders* of magnitude. PML places a conductor at the border. But PML splits the

[10]Dr. Moore *et al.*[36] in (1.5) offers an intuitive explanation of this tricky derivation. They also give a good review of ABC and OSRC literature.

field components so that one component "sees" the conductor but another does not. With this extra degree of freedom, it is possible 1) to match the impedance so waves from all directions and frequencies do not reflect[11] and 2) to have the fields decay exponentially. The fields decay so sharply that the grid needs to be compressed in the conductor. The details of this grid compression are described elsewhere.[49,51] Where the mesh is truncated, the fields can be set to zero[49] or be terminated by ABC.[52,53] If the fields are set to zero as in a perfect electric conductor, the theoretical reflection equals the field value at this perfect conductor.

$$R(\theta) = \exp\left(-\frac{2}{n+1}\frac{\sigma_{max}\delta}{\epsilon\, c}\cos\theta\right),$$

where θ is the angle of incidence, $\sigma_{\max}$ is the maximum conductivity or the conductivity at the edge, ϵ is the electric permittivity, δ is the thickness of the conductor, n is order of the polynomial which describes the conductivity's spatial profile, and c is the speed of light. In practice, the actual reflectivity is greater than this theoretical value. The approximations in how the fields and conductivities are differenced in this absorbing layer lead to mismatched impedances, causing additional reflections. The conductivity is gently increased from zero near the solution domain to $\sigma_{\max}$ near the mesh edge. Using Berenger's notation,[49] the conductivity σ can be expressed as

$$\sigma(\rho) = \sigma_{\max}\left(\frac{\rho}{\delta}\right)^n,$$

where the distance ρ into the conductor varies from 0 at the edge of the solution domain to δ next to the perfectly conducting outer boundary. Following Berenger's lead, most have used quadratic ($n = 2$) gradations. Taflove's[54] and our[55] group have independently shown that quatric ($n = 4$) gradations suffer from even less reflections (see chapter 7). Berenger's formalism has since been expanded from 2D to 3D,[56] from free space to dielectric,[57] from Cartesian to curved coordinates,[58] from vector to parallel computers,[59] from time to frequency domain,[52,60] from finite difference

[11] However, De Moerloose and Stuchly[50] show that evanescent waves experience a spurious phase shift.

to finite element,[60] and from FDTD to TLM (transfer matrices).[61]

If one desires more information on FDTD, let me suggest some references. Three reviews summarizing the "state of the art" (as of 1995) stand out with its many references,[62] its broad expanse,[63] and its authoritative nature.[54] Prof. J. A. Kong's *Progress in Electromagnetic Research (PIER)* series[64] is also excellent. For something of a more tutorial nature, I suggest books by Kunz and Luebbers[65] and Taflove.[66] To get started, one can purchase FDTD codes with ABC boundaries form Lawrence Livermore National Lab (3D), Prof. Luebbbers, Prof. Taflove, Prof. Kong (2D), and Ansoft. These have varying sophistication in user interface. But there are no "commercial" codes available with the new PML boundaries.

For this thesis, I have worked on two FDTD programs — one scalar-like FDTD with ABC boundaries and one vector FDTD with PML boundaries. Josh Winn and I have developed the scalar-like FDTD (see chapter 5) code. This approach does not suffer from the additional complexity associated with staggered grids. Memory-wise, it is a bit more efficient since only one dielectric grid needs to be stored. Some have tried hybrid models using both scalar and vector FDTD.[67] To our knowledge, we[68,69] are the first to apply this scalar-like FDTD method to solve optical problems. In particular, we have developed a novel way to measure transmission and reflection[69] (chapter 5). We have also ported this code to a massively parallel computer.[35] And we have done the first detailed study of this code (chapter 6), comparing the parallel machine with a Cray computer. Unfortunately, the new PML boundary condition has not been yet adapted for scalar-like FDTD, so the simulations in chapters 5 and 6 use the standard ABC approach.

The other FDTD program is a vector implementation, coupled with our new quatric PML boundaries. Kevin Li wrote parts of this code. The benefits of this novel boundary condition[55] are described in chapter 7. Chapter 8 apply this new boundary condition to air bridge structures.[69–72] Our group is the first to apply FDTD methods to these photonic band gap materials.[68,73]

FDTD codes can calculate scattering, transmission, reflections, voltages, currents and impedances. These codes find diverse uses — modelling radar crossections, an-

tennas, electromagnetic compatibility, waveguides, etc. We apply FDTD to optical gratings and to photonic band gap materials.

1.4 Photonic band gaps

Index gratings such as hi-reflection (HR) coatings on optical lens, gratings in optical fibers, and distributed feedback (DFB) structures in semiconductors are commonly used to reflect light in a narrow frequency band. These wavelength specific mirrors are formed by alternating low and high index dielectric layers. Whenever light encounters a change in refractive index (or dielectric constant), some light is transmitted while the rest is reflected. In these gratings, the periods of index modulations are set[12] such that reflections from consecutive periods add in phase. This produces a strong overall reflection in a narrow frequency range, called the "stop band." And when light whose frequencies are in the stop band is incident on this grating, the transmitted light decays exponentially. Propagation is not permitted. These periodic structures can be modified so that one frequency within the stop band is transmitted (or anti-reflected). The introduction of a $\pi/2$ or $\lambda/4$ phase shift splits the grating in two so that the reflections from these two halves interfere destructively at that "one" frequency, producing a narrow transmission resonance.

A generalization of DFB gratings, photonic band gap (PBG) materials, can reflect light in more than one spatial dimension. A material is known to have a "complete" gap for a particular frequency if it reflects that frequency independent of its incoming angle (or propagation direction). Such materials tend to have periodicity as viewed from many directions. And typically, along a given direction or line, the index corrugations tend to be high, so a wide range of frequencies propagating in that given direction are reflected. In a photonic crystal, these frequency ranges, associated with each and every direction, overlap intersecting in a much smaller frequency band, called "complete" band gap. Other intuitive views of photonic band gaps compares them to energy band gaps in atomic crystals. Why much of the earlier studies of photonic

[12]to roughly half the wavelength

crystals borrowed computer codes, concepts (like Bloch waves and Floquet modes), and notation (from group theory) from solid state physicists! Prof. Joannopoulos *et al.*'s book[74] expounds on this analogy.

Just in this decade, a complete, 3D photonic band gap — that reflects light from all directions in three dimensional space — has been demonstrated experimentally.[75] These photonic crystals have been studied theoretically. The wave vector equation can be expressed as

$$\nabla \times \left(\frac{1}{\epsilon(\mathbf{r})} \nabla \times \mathbf{H}(\mathbf{r}) \right) = \left(\frac{\omega}{c} \right)^2 \mathbf{H}(\mathbf{r}), \tag{1.7}$$

where H is the magnetic field, ϵ is the electric permittivity, and $\mathbf{r}$ is the position vector. This linear eigenvalue equation can be cast as matrix form, by using a plane wave basis. The eigenvalues and eigenvectors of this matrix can lead to propagation constants ω/c and magnetic eigenmodes. This was first done for scalar waves[76,77] and then for the more accurate vector equations.[78] Recently, the M.I.T. group has improved the computational efficiency of these matrix operations.[79] Unfortunately, the plane wave method is not exact; its accuracy is limited. Truncating the basis set to a finite size makes it hard to model discontinuities in the permittivity.[80] This has prompted the investigation of other basis sets such as Hermite Gaussians.[80,81]

Recently, the transfer matrix[82] method has gained much popularity. The transfer matrix relates the transverse fields (x and y only), both electric and magnetic, of one unit cell to another. Bloch's theorem says that these fields differ only in phase so this transfer matrix is unitary. From the eigenvalues, one can extract the propagation constant k. This matrix can also be used to calculate the transmission and reflection at one frequency. The matrix can solve arbitrary geometries, including those with complex permittivities. The transfer matrix is a powerful and versatile method. Further details are described in Dr. Pendry's review.[83]

Less popular (but also powerful) methods are time dependent beam propagation method,[84] Green's function (or KKR),[85,86] and finite difference time domain.[69] In later chapters, this thesis will describe the FDTD method in more detail.

Early theoretical investigations explored various crystal structures in search of a 3D photonic band gap. The face centered cubic (FCC) crystal[87,88] received much early attention because of its spherical-like symmetry. But researchers found "complete" gaps first in diamond lattices[89] then in face centered cubic (FCC)[75] and simple cubic (SC)[90] crystals. Photonic band gaps also existed for 2D structures with arrays of cylinders,[91,92] triangles (or hexagons),[93,94] and rectangles.[92,93] Experimental verification has been performed at microwave frequencies.[88,95,75,96,97] As people realized the difficulty of fabricating such structures, work shifted to structures that can be more easily constructed[98,70,99] and more resistant to fabrication-related disorder.[100] Recently, some preliminary realization of near-optical photonic crystals have been reported, using GaAs/AlGaAs cylinders,[101] GaAs honeycombs,[102] GaAs/AlGaAs honeycombs,[103] fused fiber cores,[104] etched silicon,[105] and GaAs Yablonovite.[106]

If the periodicity is broken at one point, a transmission resonance is introduced within the band gap (or stop band). This "defect" resembles a grating's quarter-wave ($\lambda/4$) phase slip or a crystal's donor and acceptor modes.[107] Their transmission properties are described later in this thesis (chapter 8). Since the fields are localized or trapped by the grating or photonic band gap, the "defect" also resembles a high Q resonator.[108] John proposes[87] and reviews[109] this localization phenomenon. Recently, Ozbay *et al.*[110] found that photonic band gap resonators can confine light very efficiently — without much loss; Q's of 2000 have been measured. Because photonic crystals suppress those frequencies in the "stop band", Yablonovitch points out that these crystals can suppress spontaneous emission into those frequencies.[111] This has been observed experimentally by Martorell *et al.*[112] Also, radiative dipole—dipole interactions also have been suppressed.[113] The spontaneous emission properties can also be modified by the defect[114] and at the band edge.[115,116] Besides interesting quantum electrodynamics, these microcavities may form the basis of low threshold lasers, because their small size or high localization limits the number of carriers to be pumped and because their suppression of spontaneous emission limits the number of lasing modes. The use of such low threshold lasers have been proposed for squeezing experiments.[117] The suppression of radiation leads to more efficient antennae

substrates.[118] The suppression of this radiation can also help confine light along a particular path or in a waveguide. For example, light can travel in air surrounded by photonic crystals.[119,74] This is conceptually similar to the one dimensional confinement by Bragg stacks[120] and ARROW waveguides,[121] but photonic crystals are more general, also suppressing losses in micro-bends, Y-branches and S-bends.[122]

Our work on optical filters is built on the novel air bridge geometry,[69,108] first suggested by Prof. Joannopoulos. This air bridge acts as a high Q, micro cavity resonator[108] and as a narrow pass band filter.[69,72] Such a filter might find uses in wavelength division multiplexing (WDM) systems as a channel dropping filter,[123] where it would be able to distinguish between closely spaced frequency channels. Jay Damask[124–128] has done excellent research on these filters. Our work is different in that we use the high index contrasts of photonic band gap materials. As a result, we are forced to consider their radiation properties, using such rigorous numerical schemes as scalar-like and vector finite difference time domain. Our devices exhibit wide stop bands. And their short lengths allow them to be cascaded; many filters can fit within the stopband. Such devices would be able to select one narrow frequency from a data bus containing many frequency channels. Such frequency filtering would be useful in high bandwidth telecommunication systems. Our theoretical models and designs are being fabricated by Prof. Kolodziejski's group (thanks to Ed and Gale)[129,108] and measured by Prof. Ippen's group (thanks to Costas, Dave, and Seigfried).

Photonic band gaps is a growing and expanding field. For more details on the experimental and theoretical work, consult the recent reviews;[74,117,130] they are comprehensive and well-written.

1.5 Overview of thesis

The preceding sections of this chapter give an overview of beam propagation method and the finite difference time domain method. It also reviews prior photonic band gap research.

The next few chapters describes the imaginary distance beam propagation method — a way to calculate waveguide eigenmodes. In particular, chapter 2 describes a new analytical formalism that incorporates the salient features of this method. Using this formalism, we can optimize the calculations of eigenmodes. Chapter 3 extends this technique to the computation of higher order modes. Chapter 4 shows how this method can be applied to determine bending losses.

The next group of chapters deals with the finite difference time domain method and its applications to photonic band gap materials. In particular, chapter 5 describes how a scalar-like finite difference time domain program can analyze both the resonator and transmission characteristics. It also presents a new way to separate reflected and transmitted light. How well this program ports to a massively parallel supercomputer is described in chapter 6. Comparisons with single processor machines are also presented. Chapter 7 discusses the standard FDTD method and details our improvement to the Perfectly Matched Layer boundary condition. And chapter 8 presents two air bridge designs — one with very wide stop bands and one with narrow transmission resonances.

Chapter 9 summaries and concludes. Appendix A lists my publications. Appendices B and C teach how to use the beam propagation and the finite difference time domain programs.

Chapter 2

Imaginary Distance Beam Propagation Method

Summary:

Recently, it has been shown that if the paraxial wave equation is modified such that fields travel imaginary distances, the field resulting from an imaginary-distance propagation is the fundamental mode of an optical waveguide. For the finite difference beam propagation method, we derive the factor by which each eigenmode is amplified during one propagation step. This amplification factor places limits on the inputs — step size, input field, effective index guess, and implicitness parameter — and gives clues on how to optimize the inputs. In particular, we will identify and study two optimal sets of inputs, which can reduce computational time significantly. We can obtain the fundamental mode and its propagation constant within a few propagation steps.[1]

[1]Most of this chapter has been published in *IEEE J. Quantum Electronics*.[9]

2.1 Introduction

Transverse modes of optical waveguides can be calculated by a variety of methods,[131] which in general can be divided into two categories — analytic and numerical. Two popular analytic techniques, the effective index[132] and weighted index[133] methods, can give the mode distributions and propagation constants of scalar waves by assuming the fields have sinusoidal and/or exponential form. Variational methods assume more complicated trial functions.[134,135] Often these analytic methods are very efficient, leading to quick and intuitive results. For more complicated structures, one turns to numerical approaches such as the spectral index method,[136] which relies on Fourier decompositions, and the beam propagation method (BPM), which solves the paraxial wave equation by Fast Fourier Transform (FFT),[1] finite difference,[2] and finite element[137] techniques. Normally, BPM has been applied to calculate the propagation of light in 2D and 3D waveguides of arbitrary indices. But BPM can also be used to get the eigenmodes of a structure. For example, if at every BPM step, one calculates the overlap integral of the just-obtained field $E(x, y, z)$ with the initial field $E(x, y, 0)$, the peaks of the Fourier transform lie at the propagation constants of the transverse modes.[18] If one repropagates and beats with a propagation constant, one can extract the field distribution corresponding to that propagation constant.[19] If the BPM is implemented with finite difference or finite element, the eigenvalues and eigenvectors of the matrix, resulting from the discretization of the paraxial wave equation, are the propagation constants and eigenmodes of the waveguide. This linear system has been solved with the shifted inverse power method.[4,20]

Recently, Yevick and Hermansson[23] showed that propagation along the imaginary axis can give the fundamental mode and its effective index quite efficiently. This method applies not only to finite difference and finite element BPM but also to FFT BPM. The fundamental mode has the largest propagation constant so sees the most rapid oscillations in phase when traveling down the real axis. Propagation down the imaginary axis changes these sinusoidal variations in phase into exponential growths in amplitude. A sufficiently long imaginary propagation gives the fundamental mode

— the mode with the most growth. For a thorough review, see page 20 of the introduction.

Much of the previous work on imaginary distance beam propagation has been done with the finite difference method, which divides the solution domain into a mesh. Since fine meshes tend to be computationally intensive, Yevick and Hermansson[23] start with a coarse mesh. After few propagation steps, they refine the mesh in the transverse direction. However, we save computer time by noting that we can use a very large step size in the propagation direction. In the case of the propagation along the real axis, the maximum step size has to be chosen so that the interference or beating between modes can be resolved. Resolving the relative phases between modes limits the step size to an order of a wavelength. Imaginary propagation transforms these sinusoidal phase changes to exponential amplitude changes. The step size can be enlarged since this growth can be linearized over much larger distance. But, what are the limits to the propagation step size? And should the scheme be explicit or implicit? How does the input field affect the computation time? We will address these issues with analytical expressions and numerical results.

First we will describe how imaginary propagation modifies the paraxial wave equation and its solutions. Next, we show that the finite difference beam propagation method gives a slightly different solution. For large propagation step sizes, the discrepancy between the two schemes plays a big role. In the theory section, we will derive the gain or amplification that a given mode experiences each propagation step. From this amplification factor, we see that the ability to converge to the fundamental mode is determined by the size of the propagation step, the implicitness of the matrix solution, the guess for the propagation constant, and the nature of the initial field. In the discussion and results sections we will describe analytically and demonstrate numerically how these inputs can be optimized for fast convergence. Finally, we will derive and study two sets of inputs that give optimal convergence.

2.2 Theory

First we will review how imaginary propagation can give the fundamental mode of the paraxial wave equation. The paraxial wave equation comes from substituting the field $E(x,y,z)e^{-jkn_0z}$ into the Helmholtz or wave equation. BPM solves the paraxial wave equation

$$2jkn_0\frac{\partial E}{\partial z} = \frac{\partial^2 E}{\partial x^2} + \frac{\partial^2 E}{\partial y^2} + k^2\left[n(x,y,z)^2 - n_0^2\right]E,$$

where $E(x,y,z)$ is the envelope of field distribution, z is the propagation direction, x and y are the transverse dimensions, k is the free space wave vector, and n_0 is the effective index. Note that kn_0 equals k_z — the z component of the envelope's propagation constant. If we propagate along the imaginary axis jz, the paraxial wave equation becomes

$$\frac{\partial E}{\partial z} = \hat{G}E, \tag{2.1}$$

where

$$\hat{G} \equiv \frac{1}{2kn_0}\left(\frac{\partial^2}{\partial x^2} + \frac{\partial^2}{\partial y^2} + k^2\left[n(x,y)^2 - n_0^2\right]\right). \tag{2.2}$$

We seek the eigenmodes of waveguides but we must start with a guess for the eigenmode. In general, the input field is a superposition of the eigenmodes,

$$E(x,y,0) = \sum_{i=1}^{\infty} c^{(i)}E^{(i)}(x,y),$$

where $E^{(i)}(x,y)$ is the field distribution of the ith lowest order eigenmode and $c^{(i)}$ indicates the amount of the ith eigenmode in the input field. After a distance z, each mode sees some gain.

$$E(x,y,z) = \sum_{i=1}^{\infty} c^{(i)}E^{(i)}(x,y)e^{\hat{G}^{(i)}z}, \tag{2.3}$$

where $\hat{G}^{(i)}$ is the gain of the ith mode. Since $E^{(i)}$ is an eigenmode, its gain can be

expressed as

$$\hat{G}^{(i)} = \frac{k}{2}\frac{(n_{eig}^{(i)})^2 - n_0^2}{n_0}, \tag{2.4}$$

where $n_{eig}^{(i)}$ is the ith mode's effective index. The fundamental mode $E^{(1)}$ has the largest $n_{eig}^{(1)}$ so sees the most gain $\hat{G}^{(1)}$. Thus, the field resulting from a sufficient long propagation is essentially the fundamental mode; the higher order modes are negligibly small in comparison.

$$\lim_{z\to\infty} E(x,y,z) = c^{(1)}E^{(1)}(x,y)e^{\hat{G}^{(1)}z}.$$

Given $\lim_{z\to\infty} E(x,y,z)$, $n_{eig}^{(1)}$ can be evaluated in two ways. If $n_0 \approx n_{eig}^{(1)}$, the growth rate of E gives[28]

$$k\,n_{eig}^{(1)} \;=\; k\,n_0 + \lim_{z\to\infty}\frac{\ln[\int E(x,y,z+\Delta z)dxdy] - \ln[\int E(x,y,z)dxdy]}{\Delta z}.$$

For arbitrary n_0, $n_{eig}^{(i)}$ can be obtained from the integral[135]

$$(k\,n_{eig}^{(i)})^2 = \frac{\int\{k^2n^2(x,y)|E^{(i)}|^2 - |\frac{\partial E^{(i)}}{\partial x}|^2 - |\frac{\partial E^{(i)}}{\partial y}|^2\}dxdy}{\int |E^{(i)}|^2 dxdy}. \tag{2.5}$$

Values of this integral converge ($dn_{eig}^{(i)}/dz \simeq 0$) with further propagation, as the field $E(x,y,z)$ approaches the fundamental eigenmode. Since we are only interested in the fundamental mode, we only need to know the steady state or asymptotic solution. The intermediate or transient solutions do not matter. Therefore, one should skip over the intermediate solutions, taking the largest step size Δz possible. The step sizes are affected by stability. Will the electric field reach the eigenmode? The step sizes are also limited by convergence. Does a coarse discretization in z (such as (2.6)) adequately represent the differential equation (such as (2.1))?

To address these issues, we will examine the discrepancy between the difference and differential equations. Applying finite difference[138] to (2.1) gives

$$\frac{E_{n+1} - E_n}{\Delta z} = \alpha\hat{G}E_{n+1} + (1-\alpha)\hat{G}E_n, \tag{2.6}$$

where E_n represents the field at $z = n\Delta z$. The parameter α sets the degree of implicitness. If $\alpha = 0$, the scheme is fully explicit forward Euler. Setting $\alpha = 1$ corresponds to a fully implicit, backward Euler solution. The Crank-Nicholson case ($\alpha = 1/2$) is an average of these two schemes. Solving for E^{n+1} yields

$$E_{n+1} = \left(\frac{1 + (1-\alpha)\hat{G}\Delta z}{1 - \alpha\hat{G}\Delta z} \right) E_n.$$

As in the case of the differential equation solution, we can decompose the field into a sum of eigenmodes. The ith eigenmode $E^{(i)}(x, y)$ is amplified at each propagation step by a multiplication factor

$$A^{(i)} = \frac{1 + (1-\alpha)\hat{G}^{(i)}\Delta z}{1 - \alpha\hat{G}^{(i)}\Delta z}. \tag{2.7}$$

As a result, the field at $z = n\Delta z$ can be written as

$$E_n = \sum_{i=1}^{\infty} c^{(i)} E^{(i)}(x, y)(A^{(i)})^n. \tag{2.8}$$

For $\alpha = 1/2$, we plot on a logarithmic scale the absolute value of the amplification $|A^{(i)}|$ versus $\hat{G}^{(i)}\Delta z$ (figure 2-1). On the same figure we superimpose the equivalent "amplification factor" of the differential equation and mark the $\hat{G}^{(i)}\Delta z$ values of a few modes. The difference between (2.8) and (2.3) yields the global truncation error

$$\sum_{i=1}^{\infty} c^{(i)} E^{(i)}(x, y) \left[(A^{(i)})^{z/\Delta z} - e^{\hat{G}^{(i)} z} \right].$$

Note that as Δz approaches 0, the truncation error approaches 0. We neglect the discretization error in x and y since Δx and Δy are small. In contrast, the discretization in z affects the rate of convergence strongly. In the next section we will show how various parameters affect the number of propagation steps needed to obtain the fundamental mode $E^{(1)}(x, y)$.

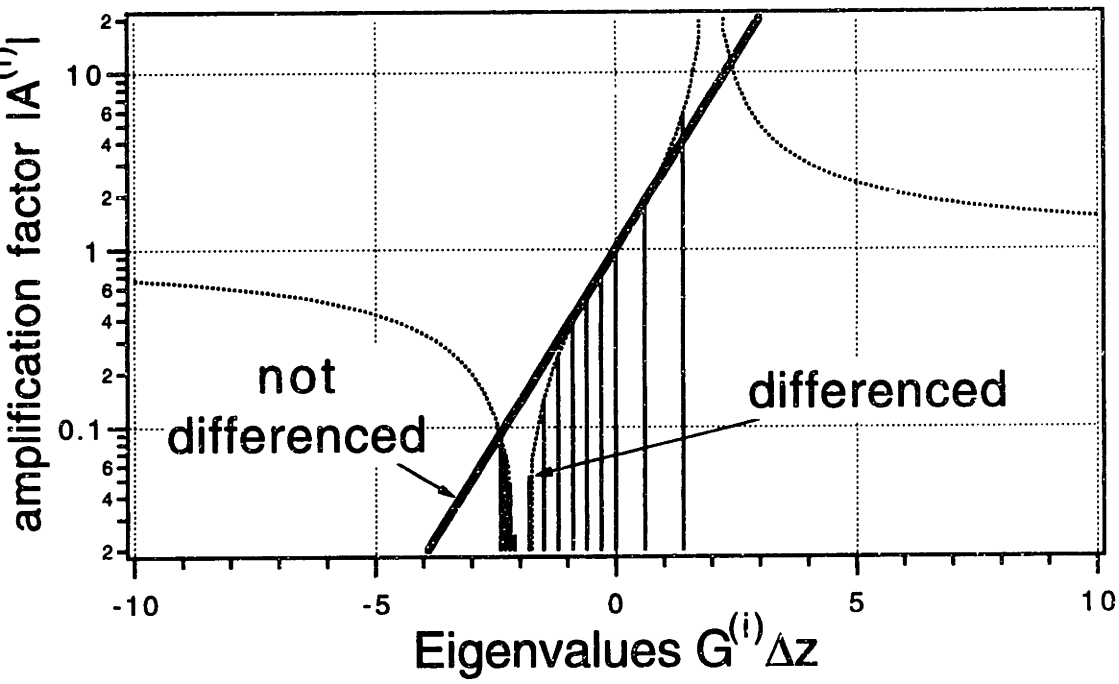

Figure 2-1: The absolute value of amplification factor $|A^{(i)}|$ when $\alpha = 1/2$ is graphed versus $\hat{G}^{(i)}\Delta z$ for a few representative eigenmodes. For comparison, the graph also includes the equivalent amplification when the paraxial wave equation is not differenced.

2.3 Discussion

The result of a long imaginary propagation is the eigenmode with the largest absolute value of the amplification factor. The sign of the amplification factor does not affect the simulation in the sense that the mode can be normalized and that the effective index calculation does not depend on the sign of field. So, to obtain the fundamental mode, we require that $|A^{(1)}| > |A^{(i)}|$ for $i \geq 2$. If the absolute value of the amplification factor $|A^{(i)}|$ for a mode i is just a little smaller than $|A^{(1)}|$, then the fundamental mode can still be obtained but a very long propagation is needed before the ith mode becomes negligible. On the other hand, if the second largest amplification magnitude is much smaller than $|A^{(1)}|$, $E^{(1)}(x, y)$ can be obtained quickly. The rate of convergence is proportional to $|A^{(1)}/A^{(j)}|$, where $|A^{(j)}|$ is second largest amplification factor magnitude. Normally, the amplification factor does not change rapidly with n_{eig} so the second lowest order mode has the second largest amplification factor ($j = 2$).

Then the rate of convergence varies with

$$\left|\frac{A^{(1)}}{A^{(2)}}\right| = \frac{|A^{(1)}|}{|A^{(1)}| - \frac{\partial|A^{(1)}|}{\partial\hat{G}^{(1)}}\frac{d\hat{G}^{(1)}}{dn_{eig}^{(1)}}(n_{eig}^{(1)} - n_{eig}^{(2)}) + \ldots}$$

$$= 1 + \frac{\partial \ln|A^{(1)}|}{\partial\hat{G}^{(1)}} k\frac{n_{eig}^{(1)}}{n_0}(n_{eig}^{(1)} - n_{eig}^{(2)}) + \ldots .$$

using $\frac{d\hat{G}^{(1)}}{dn_{eig}^{(1)}} = k\frac{n_{eig}^{(1)}}{n_0}$ and Taylor expansions. So, $|\frac{A^{(1)}}{A^{(2)}}|$ increases linearly with the slope $\partial \ln|A^{(1)}|/\partial n_{eig}^{(1)}$.

When maximizing the rate of convergence or $|A^{(1)}/A^{(2)}|$, we can vary any of the four inputs: the initial field $E(x, y, 0)$, the scheme parameter α, the effective index guess n_0, and the propagation step size Δz. In the each of the following paragraphs, we will explain how each parameter affects the possibility of and the rate of convergence.

- The **input field** $E(x, y, 0)$ is a superposition of the waveguide eigenmodes. A necessary condition for obtaining the ith mode is that the input field contains that eigenmode ($c^{(i)} \neq 0$). For example, if the substrate were symmetric, an asymmetric $E(x, y, 0)$ does not contain the symmetric mode $E^{(1)}(x, y)$ so the fundamental mode cannot be obtained. But an asymmetric input can lead to the second lowest order mode $E^{(2)}(x, y)$. And if the initial field is very close to the fundamental mode (that is, $c^{(1)}$ is large), then only a small number of steps are needed before the other modes are small relative to the fundamental.

- The **implicitness parameter** α can be set to any value between 0 and 1. Recall that $\alpha = 0$ denotes a fully explicit solution and that $\alpha = 1$ specifies a fully implicit scheme. Figure 2-2 plots the logarithm of amplification magnitude $|A^{(i)}|$ versus $\hat{G}^{(i)}\Delta z$ for various α's. The poles and zeros are at $\hat{G}_{pole}^{(i)} = 1/(\alpha\Delta z)$ and $\hat{G}_{zero}^{(i)} = -1/[(1-\alpha)\Delta z]$ respectively. Ideally, one should vary the other three parameters so the fundamental mode is at the pole — the region of highest slope. In practice, one should avoid the the pole. At the pole (2.6) reduces to

$$0 = 0 \cdot E_{n+1} = \left[1 + (1-\alpha)\hat{G}\Delta z\right] E_n.$$

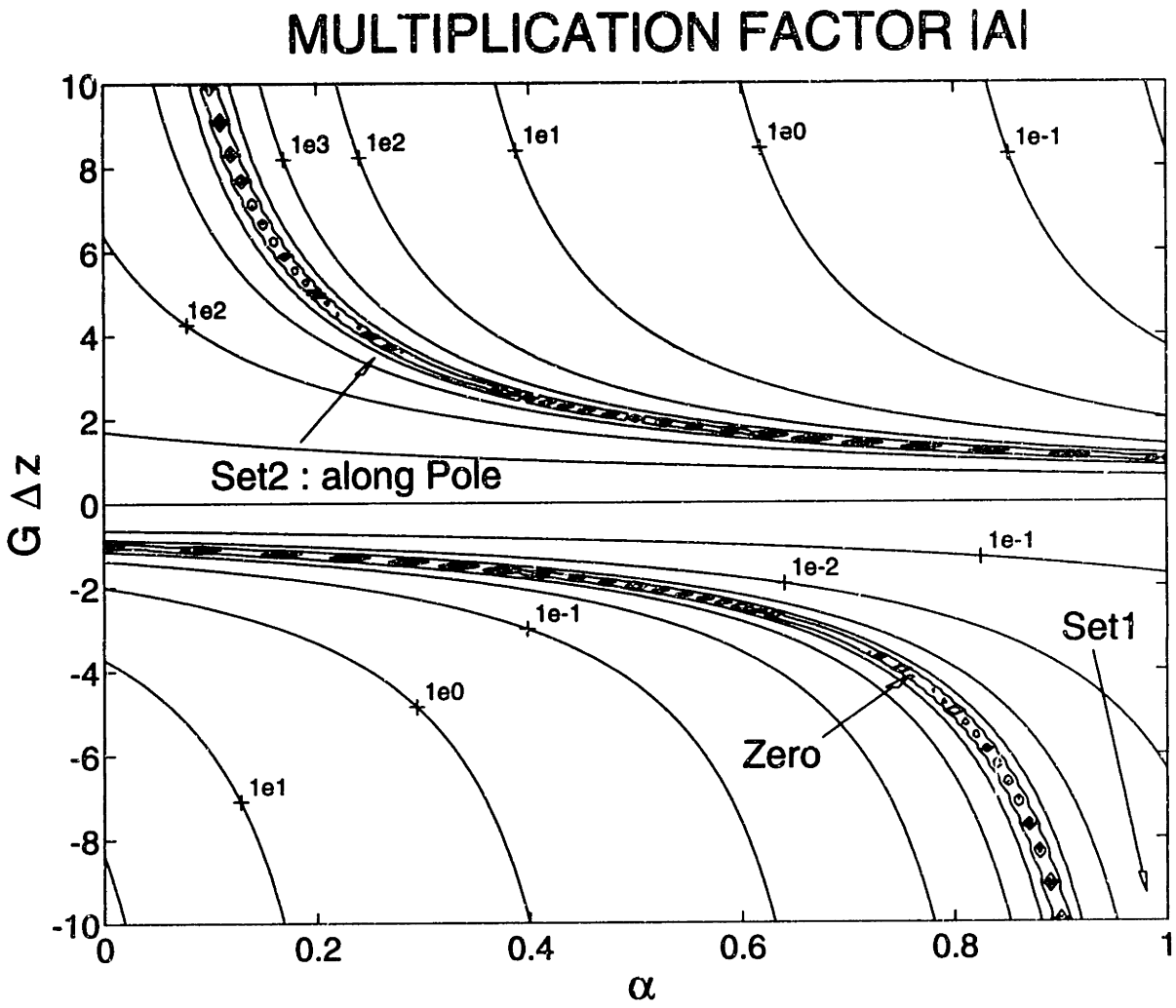

Figure 2-2: The logarithm of the amplification magnitude $|A^{(i)}|$ versus $\hat{G}^{(i)}\Delta z$ for various α's.

Note that E_{n+1} is undetermined; it is impossible to get a meaningful solution. However, one is guaranteed a meaningful solution if all the modes of the input field lie between the zero and the pole or in the area where $\partial|A^{(i)}|/\partial\hat{G}^{(i)}$ is positive. This scenario is easily achieved when $\alpha = 1$ since separation between the zero and the pole is infinite. When $\alpha \neq 1$, modes with large negative $\hat{G}\Delta z$ can be situated to the left of the zero. As a result, those modes can have an amplification magnitude that exceeds the fundamental's. If Δz is arbitrarily large, we can derive a minimum α to insure that the fundamental mode has the largest amplification.

$$|A^{(1)}| > |A^{(\infty)}| = |\frac{\alpha - 1}{\alpha}| = \frac{1 - \alpha}{\alpha}. \tag{2.9}$$

- The user also has the freedom to vary the **effective index** n_0, shifting and stretching the eigenvalue distribution $\hat{G}^{(i)}$. Equation (2.4) defines the relationship between $\hat{G}^{(i)}$ and n_0. For example, by setting n_0 to the index of the core (or cladding), one can set all the $\hat{G}^{(i)}$'s to be negative (or positive). For negative $\hat{G}^{(i)}\Delta z$, convergence is guaranteed when $\alpha = 1$. If $\hat{G}^{(1)}$ is positive, one can also set n_0 so the fundamental mode sees the highest gain. One tries to place the fundamental mode on the left side of the pole. If the fundamental $\hat{G}^{(1)}\Delta z$ is on the right hand side, a higher order mode may have a higher amplification magnitude and become the dominant mode. At the beginning of the simulation, the actual value of $n_{eig}^{(1)}$ is not known; there is large uncertainty in $\hat{G}^{(1)}$. To minimize the uncertainty in $\hat{G}^{(1)}\Delta z$, one should chose a small Δz to minimize the possibility of hitting the pole.

- One can also vary the propagation **step size** Δz. The distribution of eigenmodes in figure 2-1 spreads out with large Δz. So, for a given $|A^{(i)}|$ versus $\hat{G}^{(i)}\Delta z$ relationship, larger Δz's mean larger gain differences or faster convergence. Unfortunately, one cannot increase Δz without limit. First of all, for explicit solution ($\alpha = 0$) of the matrix equation (2.6), Δz is limited by the Courant-Friedrichs-Lewy condition.[33] Second of all, if $\hat{G}^{(1)} > 0$, then the ne-

cessity of avoiding the pole limits Δz to $1/(\alpha\hat{G}^{(1)})$. Lastly, the gain of the very high order modes must be smaller than that of the fundamental for convergence. This requirement — $|A^{(1)}| > |A^{(\infty)}|$ — leads to a restriction on Δz that is particularly severe for those schemes with small α.

Now understanding how these inputs — the initial field $E(x, y, 0)$, the scheme parameter α, the effective index guess n_0, and the propagation step Δz — affect convergence, we try to minimize computation time. We have identified two distinct regions where the slope $\partial \ln |A^{(1)}|/\partial n_{eig}^{(1)}$ is large. In such situations the fundamental mode can be obtained very quickly.

$$\frac{\partial \ln |A^{(1)}|}{\partial n_{eig}^{(1)}} = \frac{n_{eig}^{(1)}}{n_0} \frac{k\Delta z}{\left(1 + (1-\alpha)\hat{G}^{(1)}\Delta z\right)\left(1 - \alpha\hat{G}^{(1)}\Delta z\right)} \tag{2.10}$$

To maximize the slope in (2.10), we will examine two cases: $\hat{G}^{(1)} < 0$ and $\hat{G}^{(1)} > 0$.

optimal set #1: If $\hat{G}^{(1)} < 0$ or $n_0 > n_{eig}^{(1)}$, the slope is infinite when $1 + (1 - \alpha)\hat{G}^{(1)}\Delta z = 0$. But in this case, $\hat{G}^{(1)}$ is very close to $\hat{G}_{zero}^{(i)}$, where $A^{(i)} = 0$. So, the gain of the higher order modes (such as $\hat{G}^{(\infty)}$) may exceed the gain of the fundamental mode. When $|A^{(1)}| < |A^{(\infty)}|$, it is impossible to get the fundamental mode. To avoid the problems associated with the zeroes, we set $\alpha = 1$. Then the slope is maximized when $\Delta z \to \infty$. From (2.10), we obtain

$$\lim_{z\to\infty} \left.\frac{\partial \ln |A^{(1)}|}{\partial n_{eig}^{(1)}}\right|_{\alpha=1} = -\frac{k}{\hat{G}^{(1)}}\frac{n_{eig}^{(1)}}{n_0} = \frac{2n_{eig}^{(1)}}{n_0^2 - (n_{eig}^{(1)})^2}.$$

So, if $\alpha = 1$ and $\Delta z \to \infty$, any n_0 that exceeds $n_{eig}^{(1)}$ is acceptable. But if n_0 is closer to $n_{eig}^{(1)}$, convergence is faster. If $n_{eig}^{(1)}$ is not known, we set n_0 to the index of the core. Any input field is acceptable. Convergence is not only guaranteed but also very efficient. In summary, optimal set #1 is $\{\alpha = 1,\ n_0 > n_{eig}^{(1)}$ (eg., $n_0 = n_{core}),\ \Delta z \to \infty\}$.

optimal set #2: In the second scenario, $\hat{G}^{(1)} > 0$. The slope is maximum when the

denominator is zero. That implies that $1 - \alpha \hat{G}^{(1)} \Delta z = 0$ or

$$\alpha \frac{k}{2} \frac{(n_{eig}^{(i)})^2 - n_0^2}{n_0} \Delta z = 1^{-}. \tag{2.11}$$

Here many sets of α, n_0, Δz are possible. Unfortunately, the values of these sets depend on $n_{eig}^{(1)}$, which is the result or goal of the simulation. Fortunately, before the simulation starts, one usually can guess $n_{eig}^{(1)}$ to a tolerable precision $\Delta n_{eig}^{(1)}$. But to minimize the effect of given uncertainty $\Delta n_{eig}^{(1)}$ on (2.11), we try to maximize the difference $(n_{eig}^{(1)})^2 - n_0^2$; the uncertainty is a smaller percentage if the difference were larger. A large difference $(n_{eig}^{(1)})^2 - n_0^2$ implies a small Δz and a small α. The optimal set #2 is {small α, any n_0, small Δz} that satisfies equation (2.11).

In practice, set #1 is easier to implement but if $n_{eig}^{(1)}$ is known to be in a small range, set #2 may converge faster.

2.4 Results

To validate the theory, we consider a standard ridge-waveguide structure (figure 2-3), which has been defined by the COST-Working group I.[131] The computational area of $17.1\mu m$ in x (horizontal) and $3.5\mu m$ in y (vertical) direction is divided into a 172 by 71 grid. For the input field $E_x(x, y, 0)$ we chose a gaussian pulse of the form $e^{-(\frac{x-xc}{wx})^2-(\frac{y-yc}{wy})^2}$ with $wx = 1.6\mu m$ and $wy = 0.4\mu m$ and with the center (xc, yc) at $(8.5\mu m, 1.85\mu m)$ from the lower left corner. We solve the linear equation (2.6) in double precision, using ORTHOMIN,[17] a generalization of the preconditioned conjugate gradient algorithm.

In these simulations we employed Hadley's[6] transparent boundary condition (TBC). Since this boundary condition does not require the field to be zero at the borders but permits nonzero fields, much smaller computational grids can be used.[7] The consequent decrease in computational effort has led to the widespread popularity of TBC. However, TBC does assume the field at a given border point can be repre-

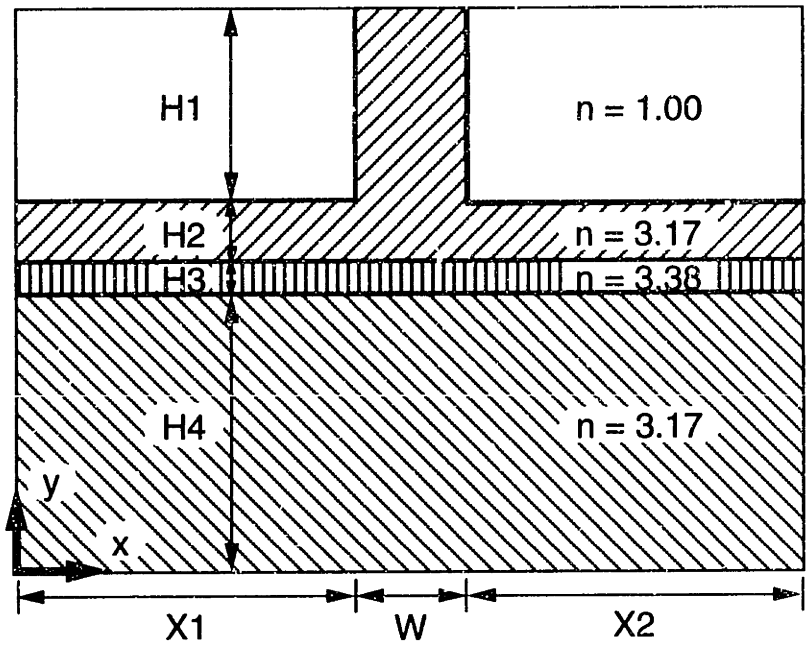

Figure 2-3: Ridge waveguide. H1 = 1.1775 μm, H2 = 0.4 μm, H3 = 0.2 μm, H4 = 1.7225 μm, W = 2.4 μm, X1 = 7.35 μm, X2 = 7.35 μm.

sented by a single, outgoing plane wave that leaves the computational window. When a pulse is composed of many wave vectors, this approximation can lead to instabilities associated with evaluating the wave vector k inaccurately.[8] Hoekstra *et al.*[13] have observed that these instabilities can lead to artificial gain at the borders. We find that sometimes the instabilities at the borders grow quite quickly, destroying the field profile. As a result, we cannot obtain a field or a $n_{eig}^{(1)}$ value that converges. Usually, the TBC is fairly stable.[7] And when instabilities do occur, they might be suppressed. For example, the noise on the borders may belong to higher order modes that see little gain. Or when E, k_x, and k_y at the borders are small, errors in calculating them do not make much of a difference. But a thorough, theoretical understanding of how TBC affects convergence is beyond the scope of this thesis; this theory does not include the effect of boundary conditions.

We vary α from 0 to 1 in increments of 0.05. The propagation step sizes Δz are 0.1, 0.14, 0.2, 0.3, 0.5, 0.7, 1.0, 1.4, ..., 100 μm. For n_0 we take two initial guesses: $n_0 = 3.1$ where $\hat{G}^{(1)} > 0$ and $n_0 = 3.3$ where $\hat{G}^{(1)} < 0$. For each α, n_0 and Δz, we

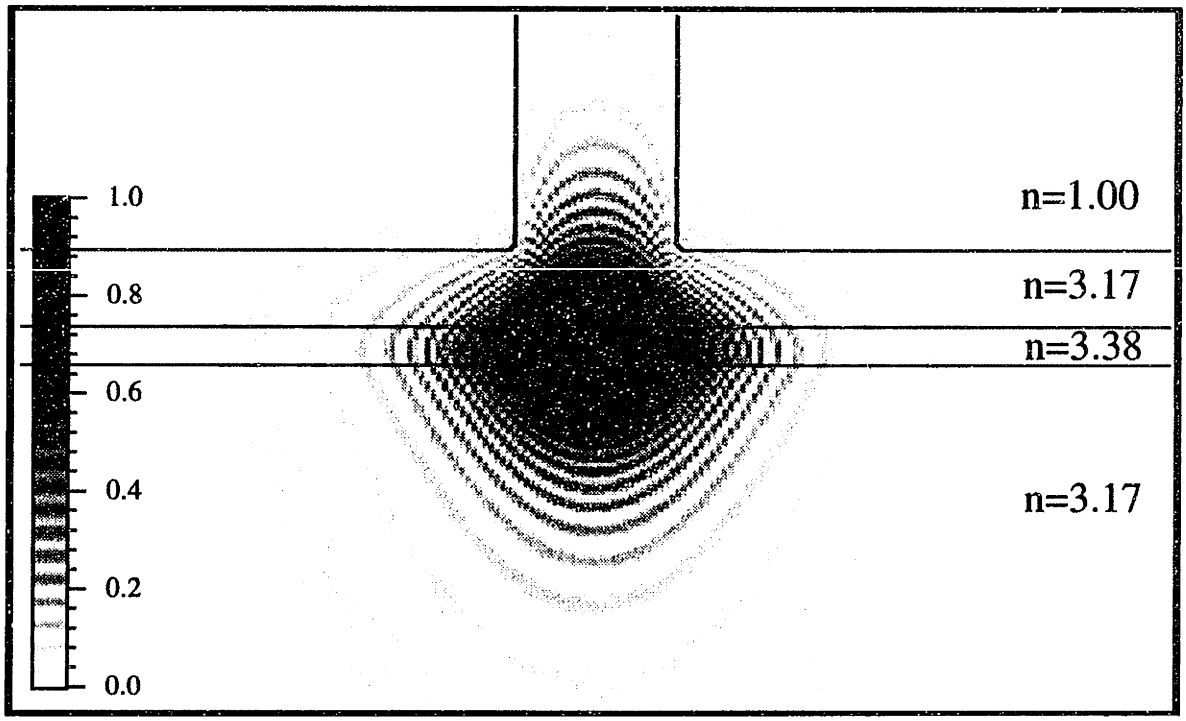

Figure 2-4: The amplitude of the fundamental eigenmode $E^{(1)}(x, y)$ is superimposed on the outline of the ridge waveguide. This is obtained in only 10 steps!

compute 50 propagation steps[2], using equation (2.6). After each propagation step, the value $n_{eig}^{(1)}$ is calculated using the integral (2.5). M is defined as the number of propagation steps at which the calculated $n_{eig}^{(1)}$ is 3.2035 or within 0.01% of the actual value. The actual $n_{eig}^{(1)}$ is 3.2038. This value compares favorably with the COST value of 3.2019. The fundamental eigenmode is shown in figure 2-4.

In figures 2-5 and 2-6 the number of propagation steps $M(\alpha, \Delta z)$ before $n_{eig}^{(1)}$ is within 0.01% of the actual value is plotted for $n_0 = 3.1$ and $n_0 = 3.3$ as a function of both α and step size Δz. No data is shown if $n_{eig}^{(1)}$ does not converge within 50 steps. The absence of data does not necessarily imply that the field will never converge; perhaps the fundamental mode will be dominant hundreds of steps later. When $n_0 = 3.1$, $\hat{G}^{(1)}\Delta z$ is positive. Therefore, figure 2-5 is related to the upper half

[2]The CPU-time for 50 propagation steps on a IBM RS6000 model 320H is 263 seconds and on a IBM ES9000-900 mainframe with vector hardware 66.6 seconds.

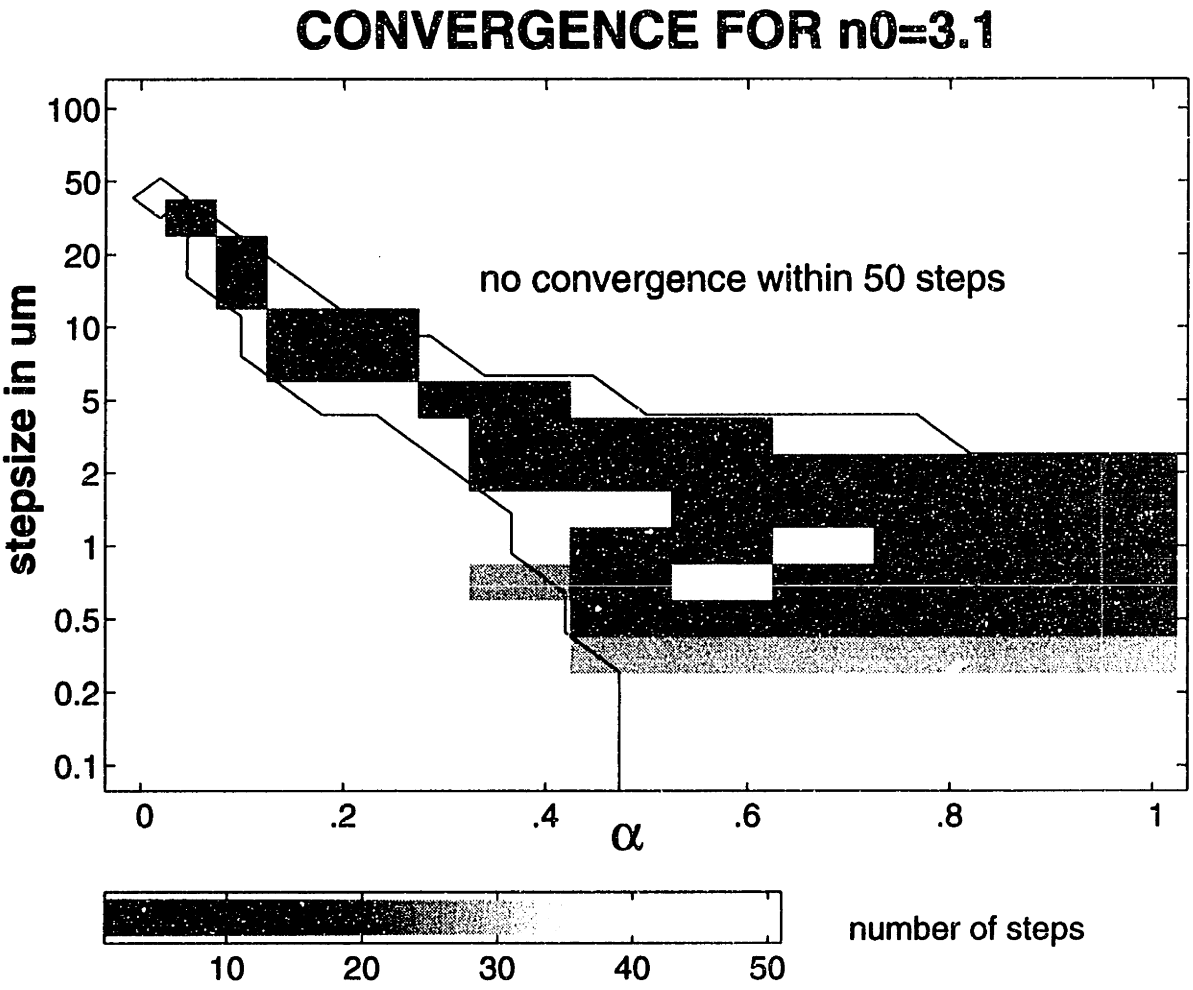

Figure 2-5: For $n_0 = 3.1$, the number steps needed for convergence as a function of α and the step size Δz. The shaded blocks show the results of numerical simulations while the line represents analytic predictions of the boundary dividing converging and nonconverging regions.

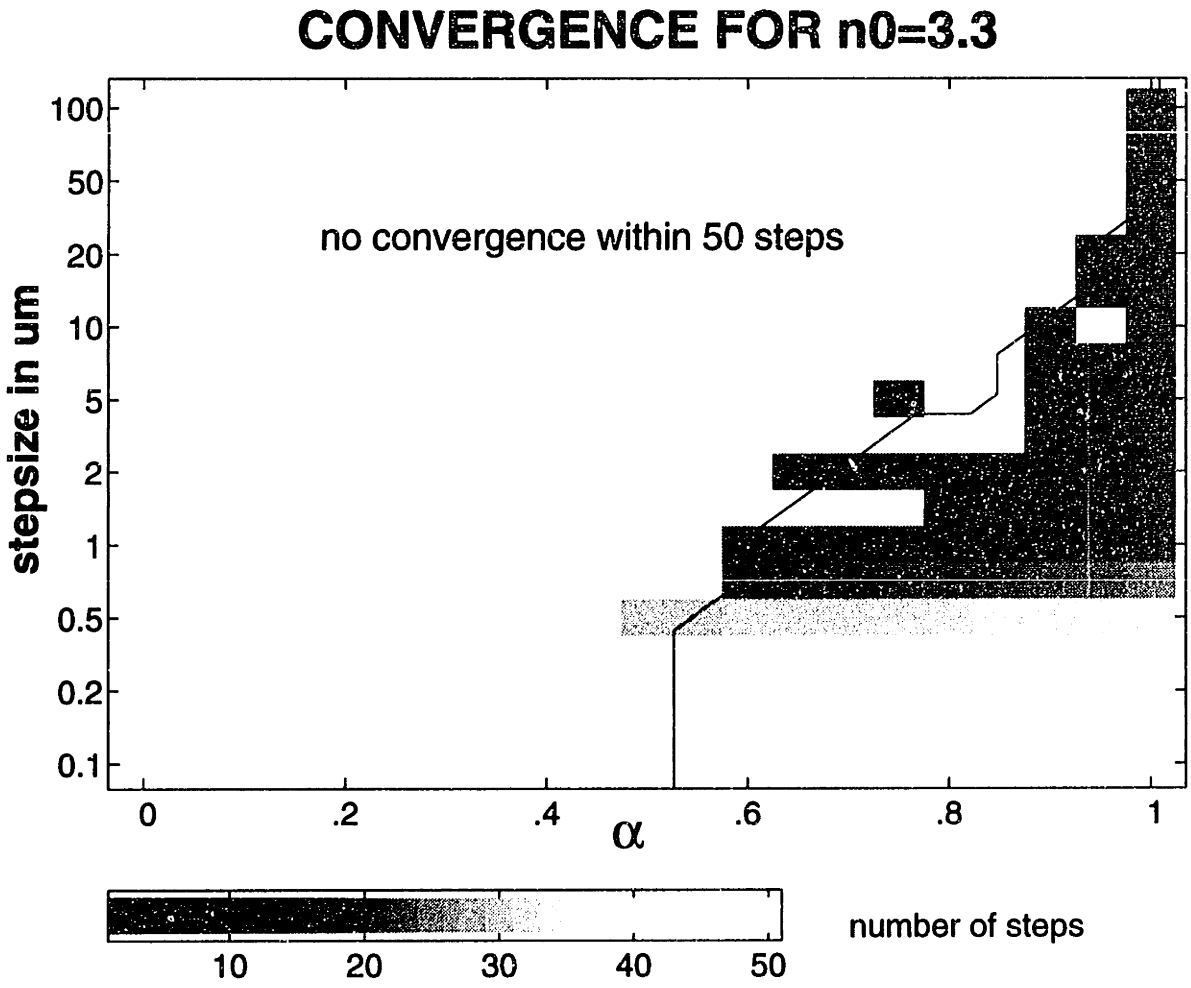

Figure 2-6: For $n_0 = 3.3$, the number steps needed for convergence as a function of α and the step size Δz. The shaded blocks show the results of numerical simulations while analytic predictions produce the line that divides converging and nonconverging regions.

of figure 2-2, which plots $|A^{(i)}(\alpha, \hat{G}^{(i)}\Delta z)|$. Similarly, $n_0 = 3.3$ leads to a negative $\hat{G}^{(1)}\Delta z$. So, figure 2-6 corresponds to the lower half of figure 2-2. Figures 2-5 and 2-6 show that the rate of convergence can vary by factors of 20, just by changing α and Δz. Clearly, a judicious choice of inputs is important to save computational time.

The lines in figures 2-5 and 2-6 separate the regions of convergence and no convergence, as predicted by the amplification factor theory. The theory says that convergence from arbitrary input fields $E(x, y, 0)$ requires that the gain of the fundamental mode $|A^{(1)}|$ exceed the gain of the other modes. This necessitates that $\hat{G}^{(1)} < \hat{G}^{(i)}_{pole}$ so $|A^{(1)}| > |A^{(2)}|$ and that $|A^{(1)}| > \frac{1-\alpha}{\alpha}$ so $|A^{(1)}| > |A^{(\infty)}|$. The first requirement is reflected in the top line in figure 2-5. Specifically, that line is a graph of equation (2.11), marking the location of the poles where $A^{(1)} = \infty$. The second requirement creates the bottom line in figure 2-5 and the only line in figure 2-6. There (2.9) becomes an equality. Occasionally, convergence occurs when the gain of the fundamental is less than the gain of the highest modes or when $|A^{(1)}| < |A^{(\infty)}|$. Figures 2-5 and 2-6 show a few of these instances. There the input field $E(x, y, 0)$ is close to the fundamental mode $E^{(1)}(x, y)$ so the higher mode components are small initially and do not grow to the size of the fundamental. If we had propagated more than 50 steps, these higher order modes would have dominated. In a few other instances, the fields failed to converge to the fundamental, contrary to theoretical predictions. We attribute such cases to the instabilities associated with the transparent boundary condition. Other boundary conditions, if they introduce less instabilities, may be more accurately predicted by our analytic theory. For example, we have tried setting the field to zero ($E = 0$) and the normal derivative to zero ($\partial E/\partial n = 0$). These two boundary conditions seem to be more stable. Although boundary conditions were not taken into account in the amplification factor theory, this compact, analytic theory stipulates necessary requirements for convergence. These requirements give very reasonable, quantitative predictions of the regions of convergence.

The contour plots of $|A^{(i)}(\alpha, \hat{G}^{(i)}\Delta z)|$ in figure 2-2 show odd symmetry with respect to $\hat{G}^{(i)}\Delta z$ and $\alpha - 0.5$. So, one naturally wonders why figures 2-5 and 2-6 do not evince this symmetry. For example, why aren't the areas of convergence the same? In fact,

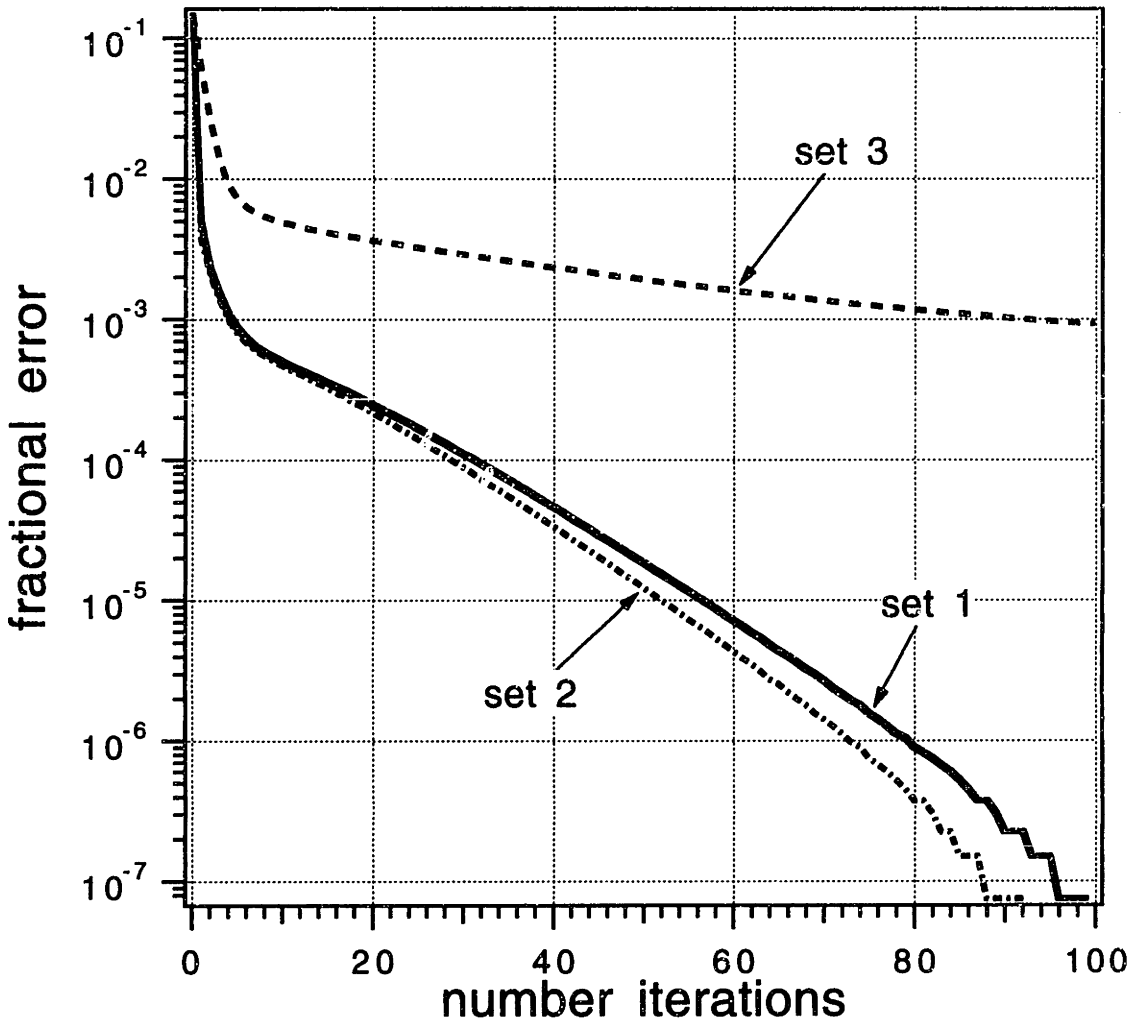

Figure 2-7: At each iteration, the effective index $n_{eig}^{(1)}$ as calculated in three simulations: set 1) $\alpha = 1$, $n_0 = 3.3$, $\Delta z = 10^{10}\mu m$, $M = 5$; set 2) $\alpha = 0.25$, $n_0 = 1.0$, $\Delta z = 0.2\mu m$, $M = 4$; set 3) $\alpha = 0.5$, $n_0 = 3.275$, $\Delta z = 0.1\mu m$, $M = 88$.

it seems that the choice of a $n_0 > n_{eig}^{(i)}$, permits a larger area of "fast" convergence. There are several explanations. First of all, though figure 2-2 exhibits symmetry about $\alpha - 0.5$, explicit and implicit solutions are very different, numerically speaking. Fully explicit solutions ($\alpha = 0$) are limited to very small step sizes while implicit schemes ($\alpha = 1$) are not. Furthermore, the distribution of the eigenvalues $\hat{G}^{(i)}$'s is not symmetric about 0. The presence of higher order modes means more negative $\hat{G}^{(i)}$'s than positive ones.

In figures 2-5 and 2-6 we note two regions of extremely fast convergence. These two regions or "optimal sets" were predicted in the previous section. They correspond

to the very high slopes that were described in (2.10). The first set — $\alpha = 1$ and $\Delta z \to \infty$ — is indicated in figure 2-6. The second region, which in figure 2-5 is shaped like a hyperbola ($\alpha\Delta z$ = constant), is described by (2.11). In this region $\hat{G}^{(1)}\Delta z$ is close to the pole depicted in figure 2-1 ($\hat{G}^{(1)} \simeq \left(\hat{G}^{(i)}_{pole}\right)^{-}$). If either α or Δz is changed slightly, the mode might find itself to the right of the pole, where the slope is negative. There convergence is not guaranteed. This explains why the "fast" and "no" convergence regions are so close to each other. In figure 2-7 we show that these two optimal sets can give estimates for the effective index $n^{(1)}_{eig}$ and the eigenmode within 0.01% accuracy within 5 propagation steps. This is over 15 times faster than the standard Crank-Nicholson method. Here the starting field is the same gaussian used for figures 2-5 and 2-6. For the first set, we used $\alpha = 1$, $n_0 = 3.30$, and $\Delta z = 1000\mu m$. Figure 2-4 shows the fundamental mode, which was obtained after only 10 propagation steps. In the second case, we use $n_0 = 1.0$, $\Delta z = 0.2\mu m$ and $\alpha = 0.25$. This corresponds to $\hat{G}^{(1)}\Delta z = 3.76$ and $\hat{G}^{(i)}_{pole}\Delta z = 4.0$. The standard Crank-Nicholson case was $\alpha = 0.5$, $n_0 = \frac{3.36+3.17}{2}$ and $\Delta z = 0.1\mu m$. Using an optimal set of inputs makes a very big difference.

Optimal set #1 gives very fast convergence. Set #1 has the added bonus that it is very easy to implement since it does not require a precise knowledge of $n^{(1)}_{eig}$. As an aid to those who will optimize their calculations using set #1, we graph in figure 2-8 the effective index $n^{(1)}_{eig}$ at each propagation step for various step sizes Δz. This graph shows that convergence increases dramatically with increasing step size. But after a while, the increases start to level off. Very large step sizes may lead to underflow errors. For example, to resolve between two transverse field values, the decrease in the square of the field after one step — $e^{2G^{(1)}\Delta z}$ where $G^{(1)} < 0$ — must exceed the computer's minimum floating point number. This field must be normalized before it gets too small. In other words, the large amplitude changes, associated with large propagation steps, necessitate that we normalize the field every few steps. But large step sizes tend to give very fast convergence.

Hopefully, figures 2-5 and 2-6 will serve as a guide as to how the convergence depends on the inputs and to which sets of inputs give the fundamental quickly. In

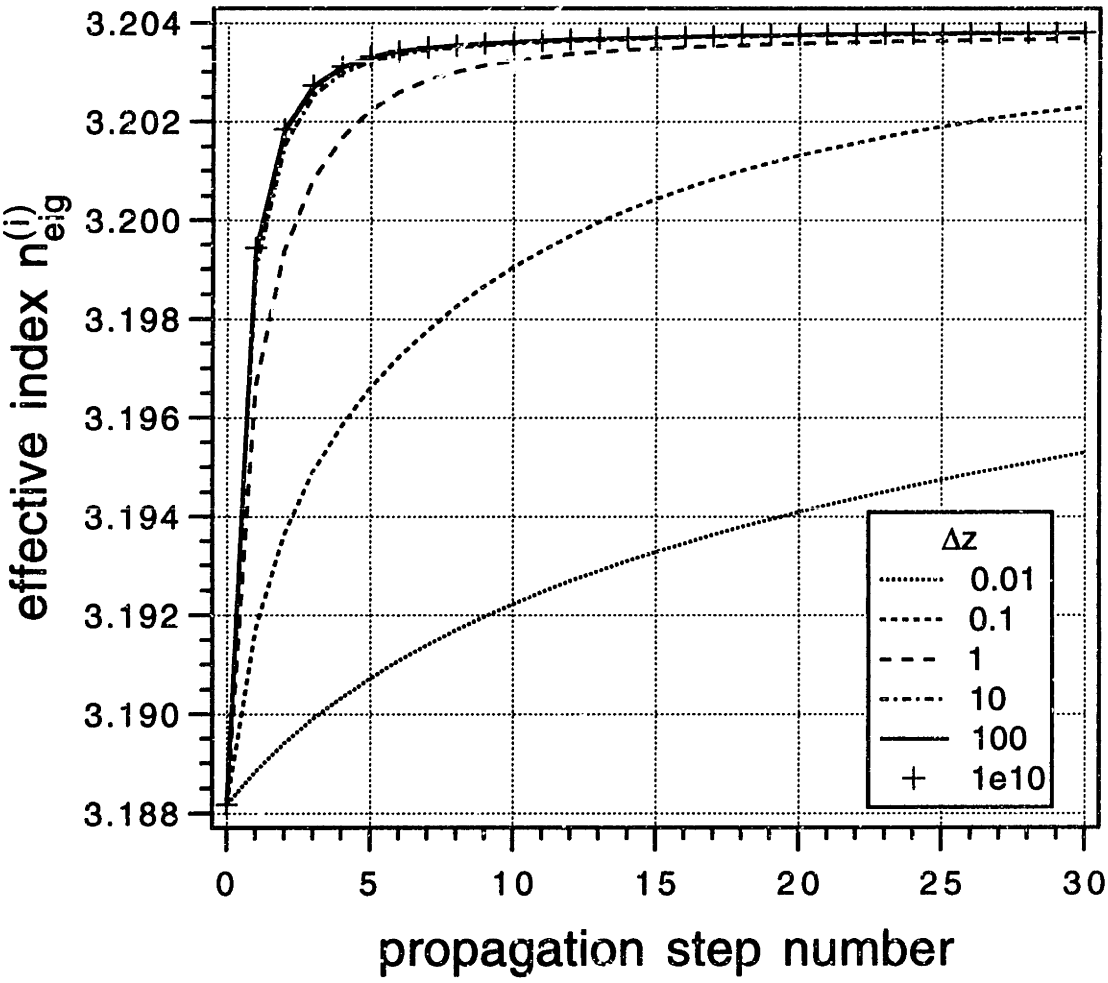

Figure 2-8: The calculated value of effective index $n_{eig}^{(1)}$ at each iteration for $\alpha = 1$, $n_0 = 3.3$ and $\Delta z = 0.01, 0.1, 1, 10, 100, 10^{10} \mu m$.

other words, they give a glimpse of how the inputs determine the rate of convergence. Figures 2-7 and 2-8 show how optimal sets #1 and #2 give very fast convergence. We have also shown that the effect of these inputs matches the theoretical predictions, which stem from knowing the amplification magnitude.

2.5 Conclusion

For finite difference beam propagation method (FD-BPM), we have presented some of the theoretical framework describing how imaginary-distance propagation gives the fundamental mode of an optical waveguide. Namely, we have derived the amplification or gain that each waveguide mode accrues during a propagation step. We have also described how each of the input parameters — initial field, effective index guess, implicitness (scheme) parameter, and propagation step size — affect the mode amplification factor and how the rate of convergence to the fundamental mode can be optimized. The predictions of this compact, analytic theory are consistent with the results from numerical simulations. Finally, we have described two sets of input parameters that can give the waveguide eigenmode and its propagation constant within a few propagation steps.

Chapter 3

Higher order eigenmodes

Summary:

Yevick and Hermansson[23] presented an efficient numerical method to calculate fundamental modes of optical waveguides. We extend their technique to higher order eigenmodes. Using finite difference beam propagation method, we obtain propagation constants and field profiles for the three lowest order TE modes in an asymmetric rib waveguide.[1]

3.1 Introduction

Recently, Yevick and Hermansson[23] showed that propagation along the imaginary axis can give the fundamental mode and its effective index quite efficiently. Yevick and Hermansson suggest the possibility of obtaining higher order modes by applying the Prony method[24,21] but to our knowledge, they have not presented a numerical implementation of the Prony technique. We will calculate higher order modes using a different technique, the power method. To illustrate the generality of our method, we choose an asymmetric coupler. The second lowest order mode of asymmetric structures are not odd so cannot be easily calculated using mirror planes. We calculate the three lowest order modes using 3D semi-vectorial, finite difference BPM.[4,138] Although we demonstrate this power method using finite difference, this method

[1]Most of this chapter has been published in *Optics and Quantum Electronics*.[31]

is general; it can be applied to FFT and FEM BPM, too. We will start with a brief overview of imaginary distance beam propagation method then describe how we calculate higher order modes.

3.2 Method

The electric field in an optical waveguide can be expressed as a sum of transverse modes.

$$E(x,y,z) = \sum_{i=1}^{\infty} c^{(i)} E^{(i)}(x,y) e^{-jkn_0^{(i)}z} \tag{3.1}$$

where $E^{(i)}(x,y)$ is the field distribution of the ith lowest order eigenmode, z is the propagation direction, x and y are the transverse dimensions, k is the free space wave vector, and $n_0^{(i)}$ is that mode's effective index. $kn_0^{(i)}$ equals k_z — the z component of the propagation constant. Let $n_0^{(1)}$ be the largest index and $n_0^{(2)}$ the second largest. The field E obeys the paraxial wave equation:

$$2jkn_0 \frac{\partial E}{\partial z} = \frac{\partial^2 E}{\partial x^2} + \frac{\partial^2 E}{\partial y^2} + k^2[n(x,y,z)^2 - n_0^2]E.$$

Yevick and Hermansson[23] propagate the field along the imaginary axis jz. Then, equation (3.1) becomes

$$E(x,y,jz) = \sum_{i=1}^{\infty} c^{(i)} E^{(i)}(x,y) e^{kn_0^{(i)}z}. \tag{3.2}$$

Since the mode $E^{(1)}$ is associated with the largest n_0, that mode will see the most gain. For large z, $E(x,y,jz) \simeq c^{(1)}E^{(1)}(x,y)e^{kn_0^{(1)}z}$. After a long propagation we are left with the mode profile with the the largest k_z. That means k_x and k_y are the smallest; the variation of the field in the transverse direction is at a minimum. This corresponds to the fundamental mode. From the mode profile we can obtain the propagation constant either from the growth in the field amplitude[28] or from

evaluating the variational equation,[135]

$$(k\,n_0)^2 = \frac{\int [k^2 n^2(x,y,z)|E|^2 - |\frac{\partial E}{\partial x}|^2 - |\frac{\partial E}{\partial y}|^2]dxdy}{\int |E|^2 dxdy}. \tag{3.3}$$

One may generalize the method so as to obtain higher order modes. Consider first the next higher order mode. In coupling structures consisting of two waveguides, the fundamental and first higher order mode determine the coupling length, an important design parameter. If the structure is symmetric, the problem is very simple. One simply requires that the field vanish at the symmetry plane and solves for the fundamental of this new waveguide structure by the same method. If the structure is not symmetric, one needs a more general approach — an approach which is a generalization of the Yevick *et al.* method. Looking at equation (3.2), one notes that, if the initial field $E(x,y,0)$ contains no component of the fundamental field $E^{(1)}(x,y)$, then the field grows at the rate $kn_0^{(2)}$ corresponding to the (imaginary) propagation constant of the first higher order mode $E^{(2)}(x,y)$, and at lower rates corresponding to the next higher modes. Since the eigenmodes are orthogonal to each other, one can subtract the field of all previously calculated eigenmodes to get the next higher order mode.

This method is analogous to the power method of linear algebra.[139] Each propagation step is similar to matrix multiplication. After many matrix multiplications, one gets the largest eigenvalue (or propagation constant) and its eigenvector (eigenmode profile) contained in the initial vector (field distribution). Therefore, if the initial vector (field) contains no components of the eigenvectors (eigenmodes) corresponding to the N largest eigenvalues (propagation constants), repeated matrix multiplication (imaginary propagation) will yield the $N+1$th largest eigenvalue (propagation constant) and its eigenvector (eigenmode). We can subtract the N lowest order eigenmodes $E^{(i)}, i = 1..N$ from the field E if all the eigenmodes are orthogonal to each other.

$$c^{(i)}e^{kn_0^{(i)}z} = \frac{\int E^{(i)*}(x,y)E(x,y,jz)dxdy}{\int E^{(i)*}(x,y)E^{(i)}(x,y)dxdy}$$

$$E_{final}(x,y,jz) \equiv E(x,y,jz) - \sum_{i=1}^{N} c^{(i)} e^{kn_0^{(i)}z} E^{(i)}(x,y)$$
$$= c^{(N+1)} e^{kn_0^{(N+1)}z} E^{(N+1)}(x,y) + \sum_{i=N+2}^{\infty} c^{(i)} e^{kn_0^{(i)}z} E^{(i)}(x,y)$$

This subtraction must be done once at the onset to insure the initial field does not contain lower order modes. Numerically, this subtraction may be done imperfectly, leaving residual traces of the N lowest order modes. Since these traces grow faster than the other modes, it is necessary to subtract out these N modes at the end of the simulation. In practice, it is preferable to subtract several times during the simulation.

A mode that is "cutoff" decays exponentially when propagating along the real axis. However, propagation along the imaginary axis converts an exponential decay to a phase change. So, this method can obtain "cutoff" modes. It applies to any dielectric medium with real indices, including weakly nonlinear media with self phase modulation. In addition, this algorithm can be applied to any of the three BPM types. We happen to use the finite difference method, specifically a 3D, semi-vectorial, time independent, Crank-Nicholson scheme.[138] The resulting sparse matrix is solved by a generalized form of the preconditioned conjugate gradient method called ORTHOMIN.[17] As developed by Stern,[4] the semi-vectorial approach solves the scalar wave equation but accounts for the discontinuity in fields that result from index variations. Huang *et al.*[138] have showed that Stern's approach is equivalent to solving the full vector wave equation if one ignores the cross coupling between transverse field components.

3.3 Application

Recently, several investigators have analyzed asymmetric waveguides, demonstrating two primary applications. First of all, the coupling lengths of asymmetric structures depend less on wavelength since the fraction of power transferred is less.[140–142] In addition, if the dispersion curves of the two waveguides intersect at a small angle, then

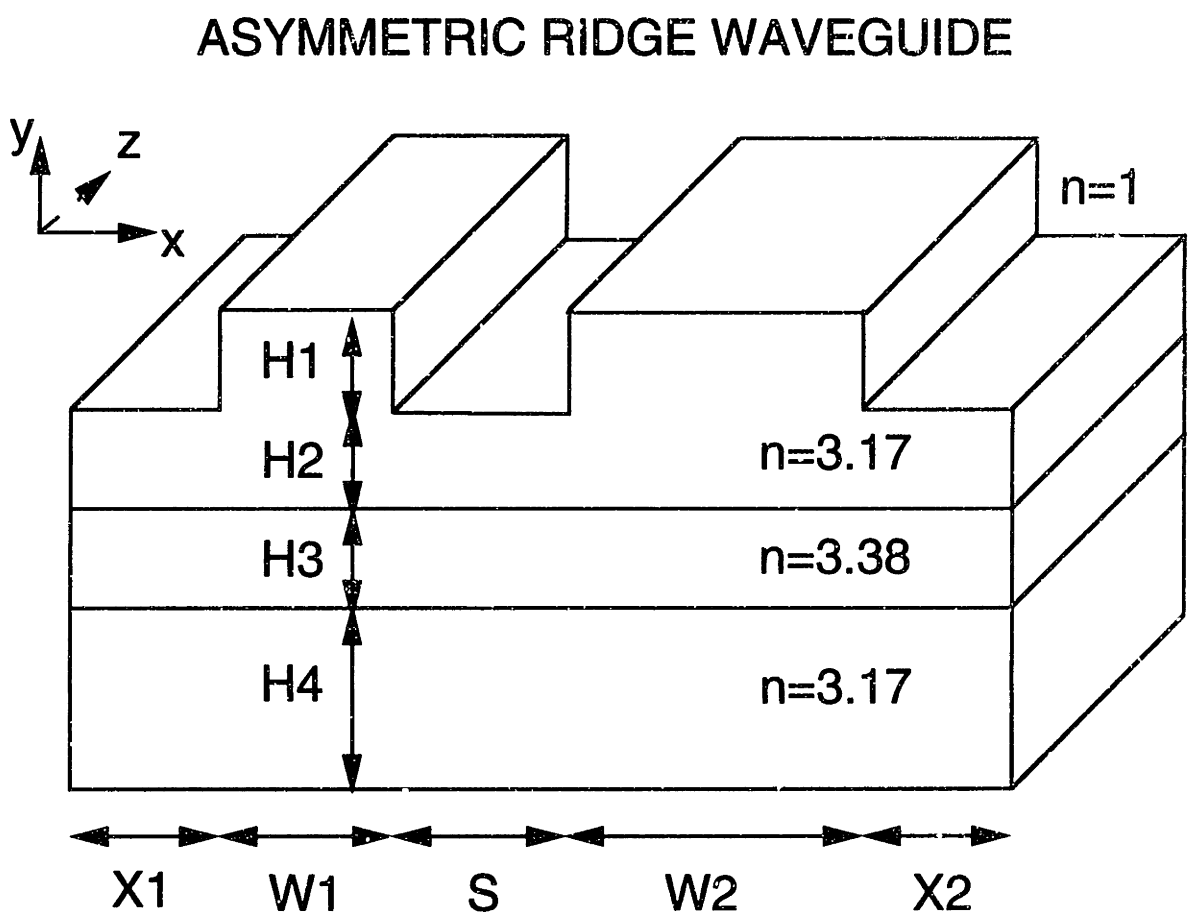

Figure 3-1: Structure geometry for the asymmetric ridge waveguide.
W1 = 2.08 μm, W2 = 4.00 μm, X1 = 8 μm, X2 = 8 μm, S = 1.92 μm, H1 = 1.02 μm, H2 = 0.42 μm, H3 = 0.18μm, H4 = 3.51 μm.

full power transfer occurs only within a narrow band, creating a narrow filter.[143-145] The asymmetry in propagation constant can be formed in two ways. Guides with symmetric geometry can differ in their indices through the electro-optic effect, while other guides achieve asymmetry in their physical geometries or dimensions. Our ridge waveguides differ in their widths (see figure 3-1). This geometry was inspired by Yanagawa *et al.*'s[142] broad-band 8x8 star coupler.

In the transverse direction we divide the 20 by 6 μm region into a grid of 151 by 101 points. The field is set to zero at the boundaries. To get the second lowest order mode, we must first calculate the fundamental mode. The choice of initial field strongly affects the computation time. If the resemblance between the initial field and

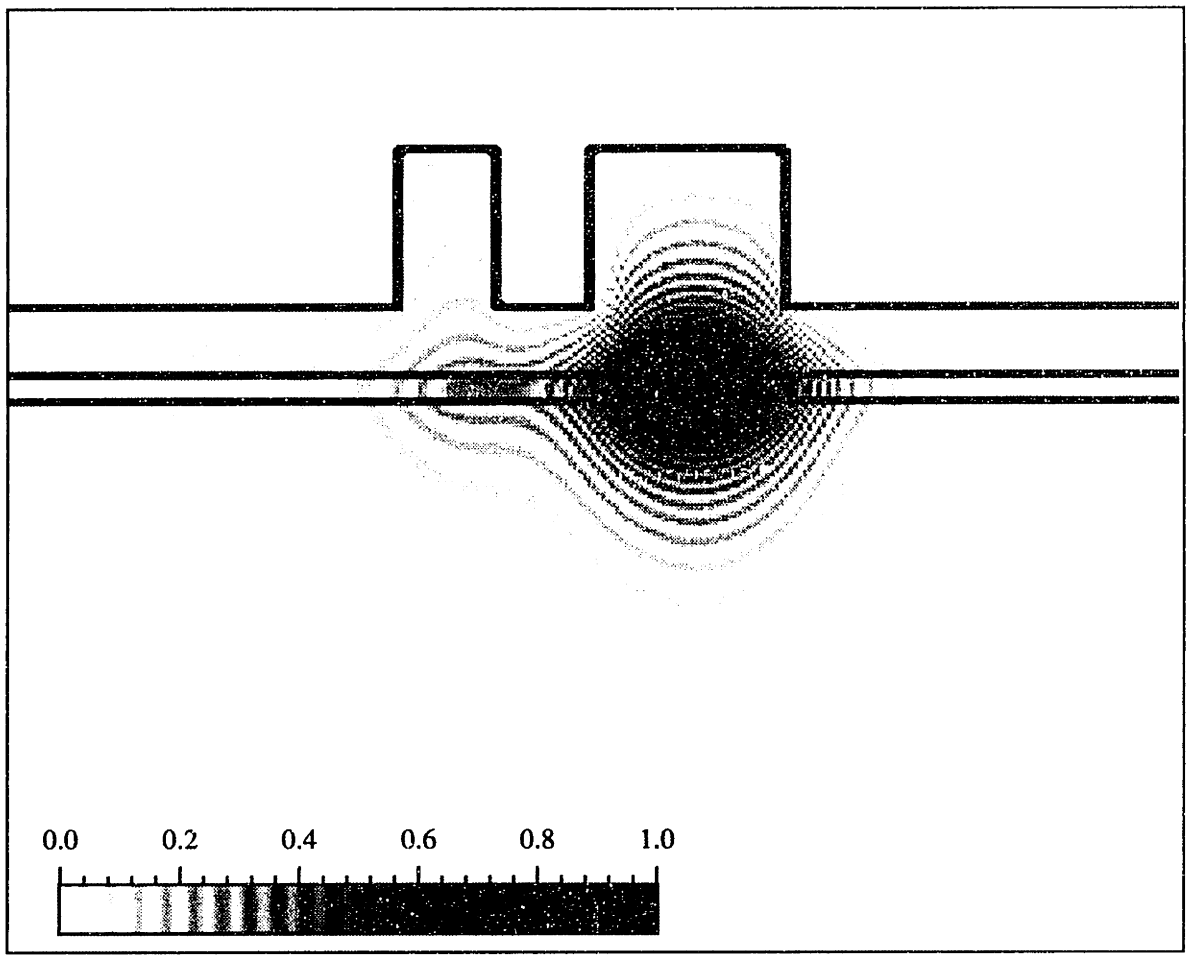

Figure 3-2: Normalized fundamental TE mode (horizontal, in plane)

the fundamental mode is poor, or if the amount of the fundamental mode contained in the initial field is small, many iterations are needed before the fundamental mode can grow to the point being dominant. On the other hand, if the initial field closely resembles the fundamental mode, only a few propagation steps are needed before the field converges.

Since the mode of the coupled waveguides resembles to first order those of the individual guides, the input field of the fundamental mode has been chosen as a superposition of two gaussian inputs centered in the high index guiding layer under each rib. The gaussians have equal amplitudes and FWHMs (Full Width Half Maximums) of 20 horizontal and 10 vertical gridpoints. The input fields of the second lowest mode are identical except that sign of the right gaussian is reversed. For the third lowest

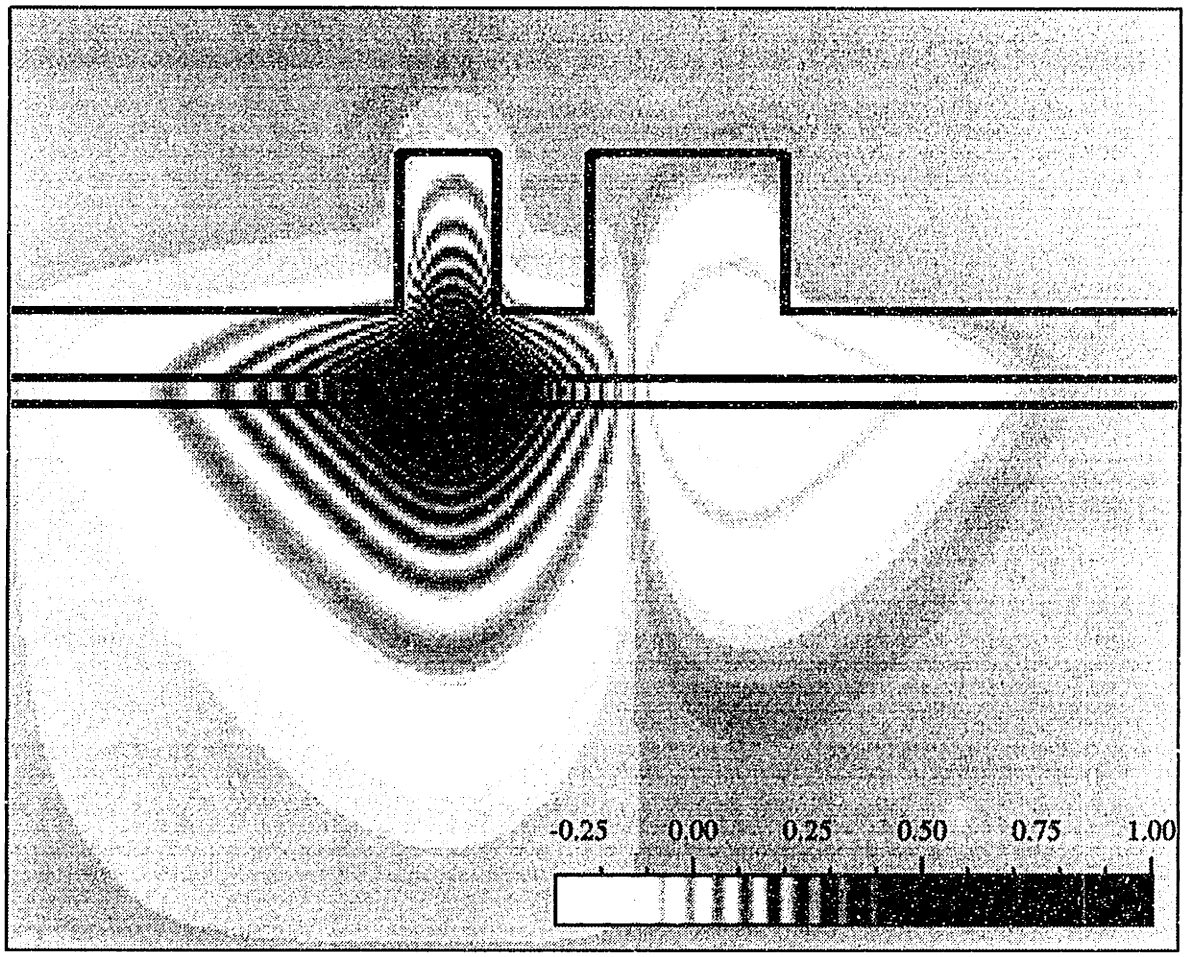

Figure 3-3: Normalized second lowest TE mode (horizontal, in plane)

order mode, the initial field is a superposition of three Gaussian fields: the largest beam below the larger rib, one beam below the smaller, and another with opposite amplitude in the middle. From left to right, the FWHMs are 5 by 5, 30 by 15, and 20 by 15 gridpoints in x and y-direction respectively. And from left to right, the relative amplitudes are 2, -1, and 1.

To obtain the two lowest order TE modes (see figures 3-2 and 3-3), we propagate 300 μms with 0.5μm steps. The convergence is rapid; after only 100 iteration steps, the fields approach within 1% of their final values. The 600 iterations take 62 minutes on an IBM RS6000 workstation, model 320H (6.0 MFlops). For the third mode (figure 3-4), the step size was increased to 2 μm. This increase does not affect the stability

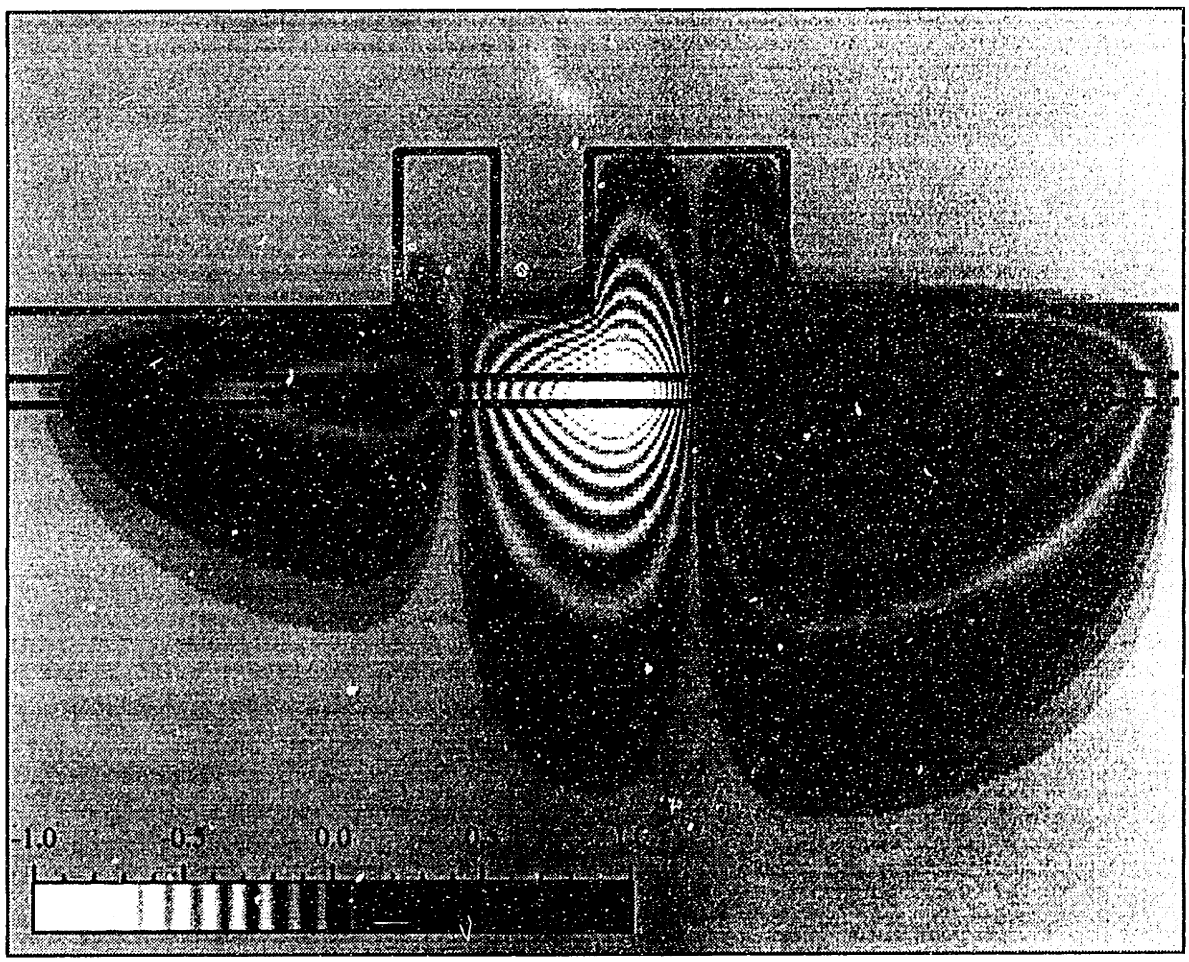

Figure 3-4: Normalized third lowest TE mode (horizontal, in plane)

but does lead to faster convergence.[2] The simulation also involved 600 imaginary propagation steps. One has to be careful about the intervals at which the lower order modes are subtracted. Frequent subtraction can increase the computation time by a few percent but keeps the higher order modes small.

Equation (3.3) gives an estimate for the propagation constants. For the structure in figure 3-1, we determine $n_0^{(1)} = 3.2005$, $n_0^{(2)} = 3.1973$ and $n_0^{(3)} = 3.1942$ for wavelength $\lambda = 1.55\mu$m.

[2]Even faster convergence would have resulted if we had used the optimal parameter sets of the previous chapter. But we had not yet discovered this set when we wrote this paper.[31]

3.4 Conclusion

In conclusion, one can simulate exponential gain by propagation along the imaginary axis. Lower order modes have larger propagation constants so they will see more gain. If the eigenmodes are orthogonal, subtracting the fundamental mode leaves the next higher order mode. Subtracting these two lowest order eigenmodes gives the third lowest mode. In principle, this method can be extended to find even higher order modes.

This method can calculate transverse eigenmodes and propagation constants of any substrate with real indices. Using beam propagation, we obtain the three lowest order TE modes in an asymmetric coupler.

Chapter 4

Ways to reduce bending loss

Summary:
We reduce the modal mismatch losses that occur at a junction of curved and straight rib waveguides, by offsetting the guides and placing isolation trenches. Using a 3D semi-vectorial beam propagation program, we also can investigate more novel effects such as rib heights and sidewall slopes. Our consideration of all these effects results in an optimized design.[1]

4.1 Introduction

Bent or curved waveguides are important in integrated optics. Bent guides can change the propagation direction. In addition, they split power in Y-branches and help switch light in Mach-Zehnders. If such guides have small radii or change direction abruptly, compact optical devices result. Unfortunately, these compact chips radiate light. Some power dissipation or "pure bending loss" occurs when light travels down a bend of constant radius. Additional radiation occurs when the bend radii change. Each guide with a fixed radius of curvature can be associated with a particular eigenmode. At a junction where the bending radius changes abruptly, mismatch between these eigenmodes leads to a transition loss. This transition loss is particularly severe where straight and curved waveguide segments meet. This junction is the dominant source

[1] Most of this chapter will be published in *IEEE J. Lightwave Technology*.[146]

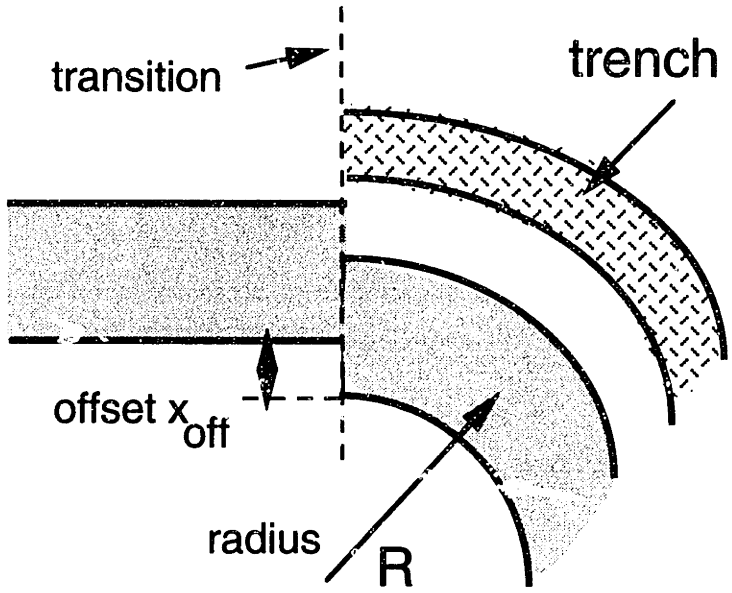

Figure 4-1: Interface between straight and curved waveguide segments, viewed from the top of the chip.

of bending loss for most optical devices.

The most straightforward way to make the straight and curved waveguide modes look more similar, is to increase the radius of curvature.[147,148] But over the past decade, many have suggested more sophisticated ways to reduce the transition loss. Since the field of a curved waveguide tends to be pushed radially outward, E.-G. Neumann *et al.*[149] proposed offsetting the straight waveguide to improve mode coupling (figure 4-1). He also suggested placing a trench outside the curved waveguide. This trench prevents light from spreading outward towards larger radii, thus improving beam confinement.[150] Others have created such trenches by indiffusion.[151] J. Yamauchi *et al.*[152] has optimized the location of such trenches. Recently, M. K. Smit's group[153] has decreased the width of the straight guide, to further reduce the field mismatch.

In this chapter, we investigate additional ways to further minimize this transition loss or field mismatch. We take into account all the previous schemes — trench location, offset amount, and guide width. In addition, we consider the effect of sloping

sidewalls and guide thicknesses.[154] The before mentioned calculations neglected or approximated the dimension extending into the substrate. But our code treats the full 3D geometry without such approximations. And to our knowledge, this paper presents the first semi-vectorial (that is, non-scalar) computation of transition losses. In the next section, we describe the numerical method. Next, we direct our optimization efforts to one common waveguide, the rib waveguide. In particular, we show how sidewall slopes and rib height can be varied to reduce transition losses.

4.2 Numerical method

First we will describe the theoretical framework that underlies our method. For a more detailed overview of applicable numerical methods, please refer to the COST-216 study.[155] Heiblum and Harris suggested that a curved waveguide in two dimensions can be conformally mapped to an equivalent straight waveguide,[156] where the index of refraction increases with the increasing radial distance. Since the radius is much larger than the waveguide dimensions, Heiblum and Harris' equivalent index can be accurately linearized.[152,157,158] Specifically,

$$n_{equiv} = n\,(1 + x/R) \tag{4.1}$$

where n is the unperturbed index of the waveguide, x is the radial distance from the guide center, and R is the radius of curvature. To this, Baets and Lagasse[157] propagated light down bent guides, using the beam propagation method (BPM). Saijonmaa and Yevick[158] extended this calculation to three space dimensions. They calculated not only the radiation loss but also the transition loss. They calculated the eigenmodes associated with the curved and straight waveguides, by beating the transverse field with the propagation constant of the desired eigenmode.[19] Then an overlap integral between the straight and curved eigenmodes gives the transmission coefficient.

$$T = \frac{\int E_{straight}(x,y) \cdot E_{curved}(x,y)\,dx\,dy}{\sqrt{\int |E_{straight}(x,y)|^2\,dx\,dy \int |E_{curved}(x,y)|^2\,dx\,dy)}}$$

The transition loss is one minus the square of the transmission, $L = 10\log_{10}(1-T^2)$. Other popular ways to calculate eigenmodes of rib waveguides are effective index[132] and spectral index method.[136,159] In this paper, we use the imaginary distance beam propagation method — an accurate, numerical method that can applied to arbitrary geometries.

In particular, we use a 3D, semi-vectorial, finite difference beam propagation program[138,28] with transparent boundary conditions.[7] We have improved the calculation speed by over an order of magnitude by an improved differencing scheme.[9] To illustrate how we minimize transition losses, we model the rib waveguide (figure 4-2), oft studied by the COST-216 group.[131] The rib is $h_4 = 1.4\,\mu$m high, spans $w_1 = 2.4\,\mu$m at the bottom and $w_2 = 2.4\,\mu$m at the top. From the bottom to top, the substrate layer thicknesses are $h_1 = 1.725$, $h_2 = 0.2$ and $h_3 = 0.3\,\mu$m, while the indices are $n = 3.17$, 3.38, and 3.17. The total computational window is 17.1 long by $4.0\,\mu$m high and is divided into square grids $\Delta x = \Delta y = 0.05\,\mu$m. In figure 4-2, the rib in curved waveguide has the same dimensions, for the most part. However, the trench is $w_t = 4.0\,\mu$m wide and has an index of $n = 1$ (air). It is positioned $w_t = 2.00\,\mu$m away from the rib. The eigenmodes are calculated by choosing implicit differencing and large reference index. We propagate a large distance $5 \cdot 10^{11}\,\mu$m with only 40 steps. This choice of input parameters has improved the speed of computation significantly.[9]

4.3 Results

Here we detail how we minimize transition losses, by optimizing guide offsets, trench location, rib widths, rib heights, and sidewall slopes. We study one radius of curvature $R = 1.5$ mm and one wavelength $\lambda = 1.5\,\mu$m. The fundamental eigenmode of a rib waveguide is pictured in figure 4-3a. This is the amplitude of the electric field polarized in the page and in the horizontal (or x) direction. As expected, the mode is centered in the highest index layer. If this rib is part of a curved waveguide, the mode shifts to the right, to larger radii (figure 4-3b). It appears more weakly

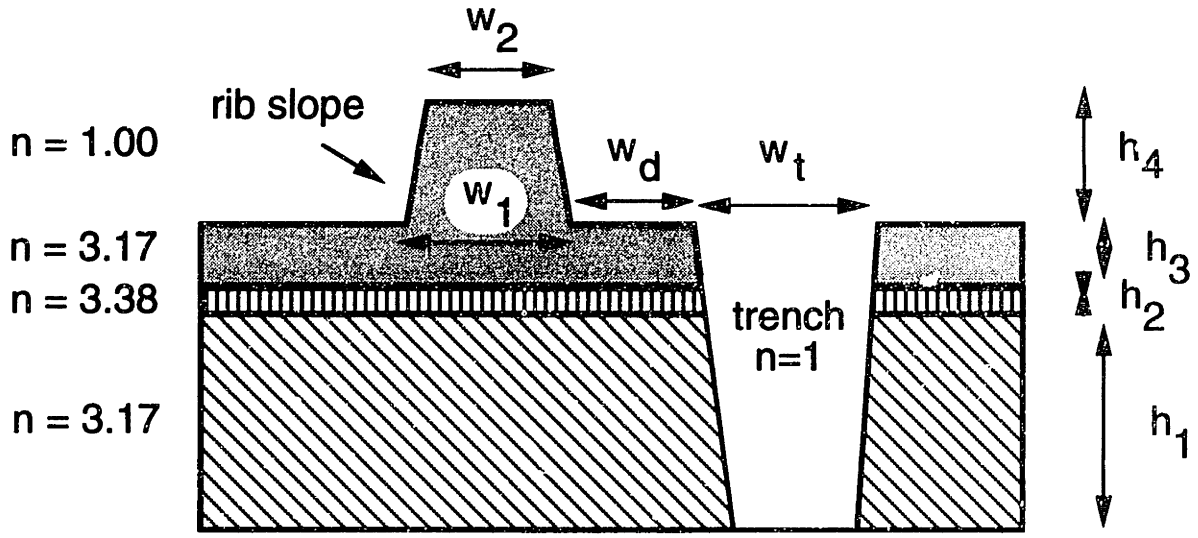

Figure 4-2: Curved rib waveguide with trench, viewed from the side.

guided. Equation (4.1) accounts for this by increasing the effective index. This asymmetric effective index distribution accounts for the lopsided or asymmetric mode of the curved guide. More power is on the right hand or large radius side. Clearly, the eigenmode of the straight rib and that of the curved rib are different. As a result, the transition loss L, given by the overlap integral of the two modes, is very large. $L = -0.9$ dB.

Since the modes of the straight and curved ribs appear displaced from each other, offsetting the two ribs decreases the transition loss. Figure 4-4 graphs the loss versus offset in microns. The loss drops from a high of $L = -0.42$ dB at offset $x_{off} = 0\,\mu$m to a minimum of $L = -0.334$ dB at offset $x_{off} = 0.5\,\mu$m. Introducing a low index material or a trench to the right of the rib pushes the field to the left or radially inward. This helps confine the beam, making the curved mode look more similar to the straight mode. Figure 4-5 graphs the transition loss versus trench–to–rib separation. We find an optimal trench position of $w_d = 2.00\,\mu$m. Another way to confine the beam or prevent the light from spreading radially is to change the rib width. In figure 4-6, while the width of straight guide held constant at $w = 2.4\,\mu$m, the width of the curved guide is varied. Here the transition loss is lowest when the widths of the two guides are equal; then the transition loss is reduced to -0.032 dB.

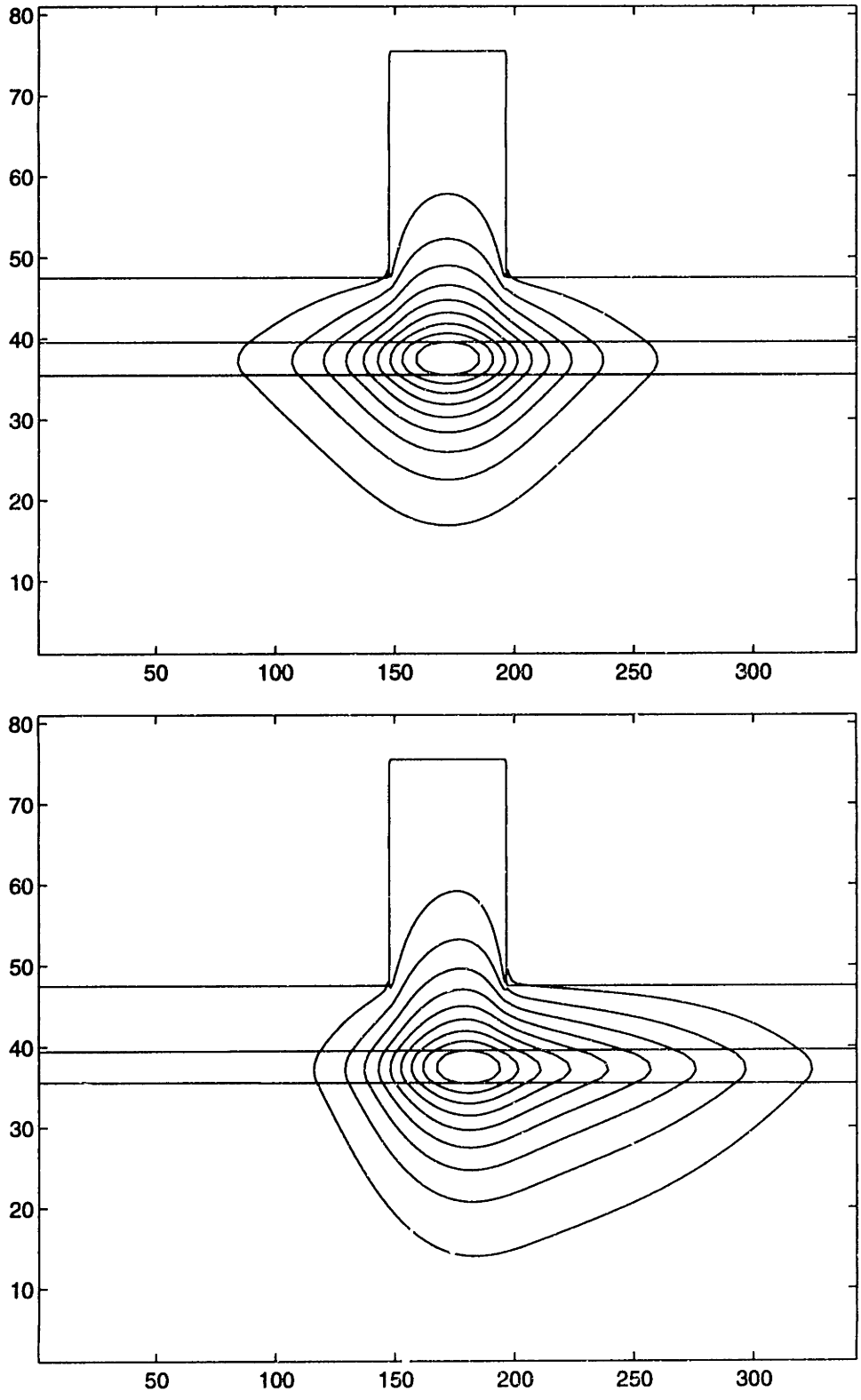

Figure 4-3: Top: Eigenmode of straight rib waveguide. Bottom: Eigenmode of curved rib waveguide.

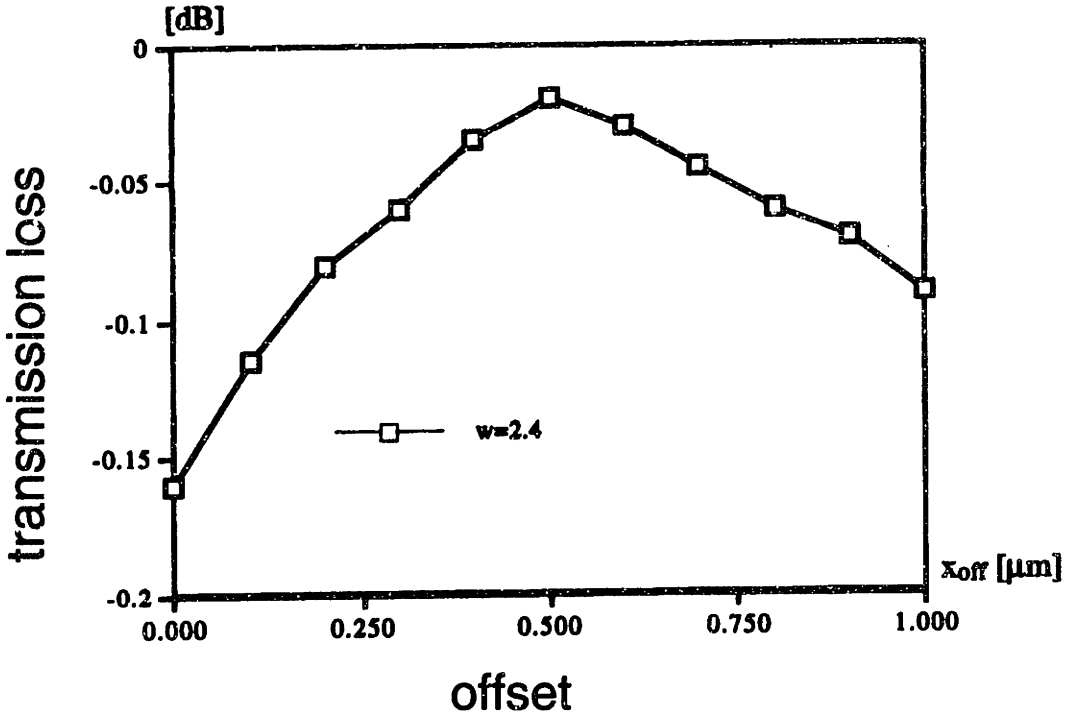

Figure 4-4: Transition loss L plotted for different offsets between straight and curved guides x_{off}.

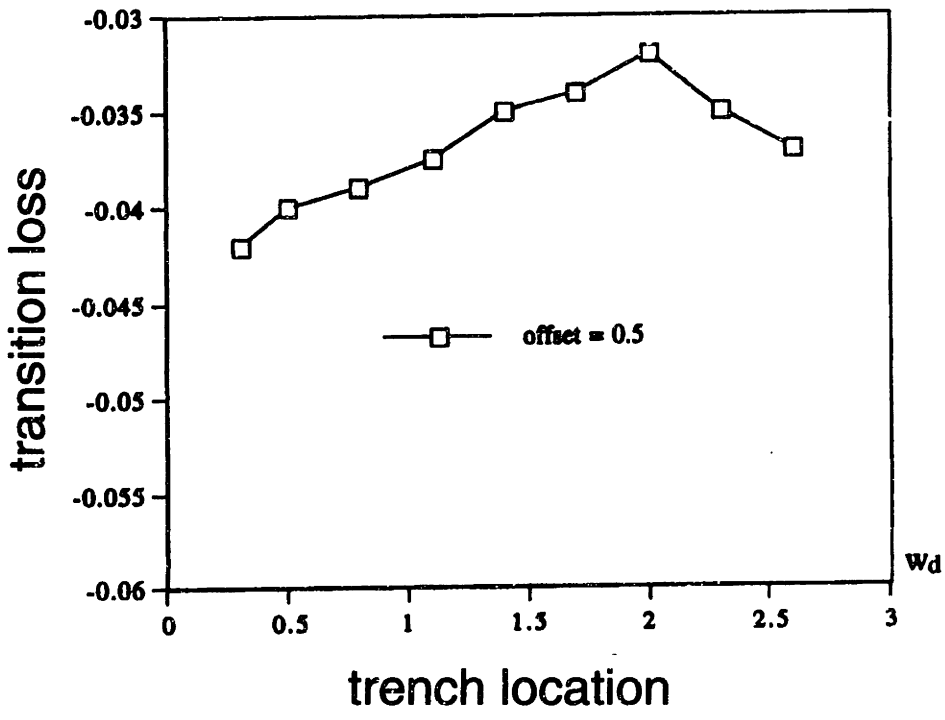

Figure 4-5: Transition loss L plotted for various trench–to–rib separations w_d.

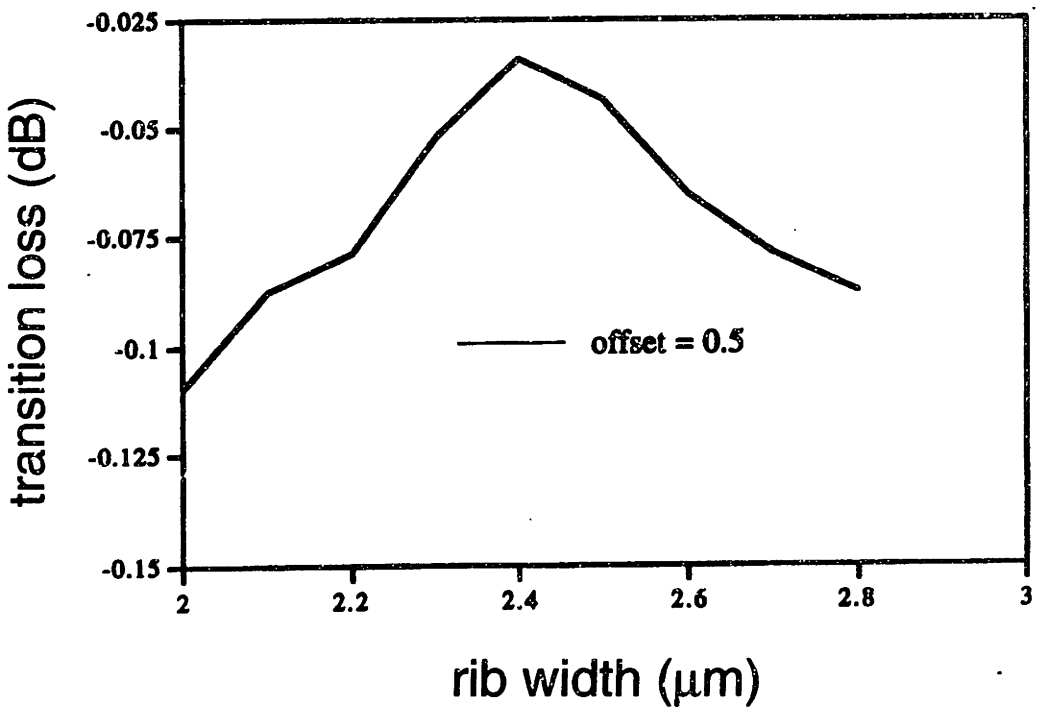

Figure 4-6: Transition loss L plotted for different widths of the curved rib w.

We can reduce the transition loss further, if we increase the height of the curved rib. We are able to calculate this loss accurately since our program is semi-vectorial and 3D. Higher ribs increases the effective index of the rib so more light is confined or guided by the rib. This reduces the spread of the beam towards higher radii. This spread stretches the mode profile. What's more, this distortion is also asymmetric, increasing the mismatch between straight and curved modes. As a result, higher curved ribs reduce the modal mismatch and hence the transition loss (figure 4-7). But the transition loss increases when the height of the straight rib increases as well. The other parameters — offset, width, trench — were optimized for a rib height of $h_4 = 1.4\,\mu$m.

Sometimes problems with the wet or dry etching leads to non-vertical sidewalls. Sloping sidewalls give us another degree of freedom — another way to match the appearance of curved and straight modes. sidewalls are depicted in figure 4-2. Note that the straight and curved guides have the same slope. We find that sloping rib

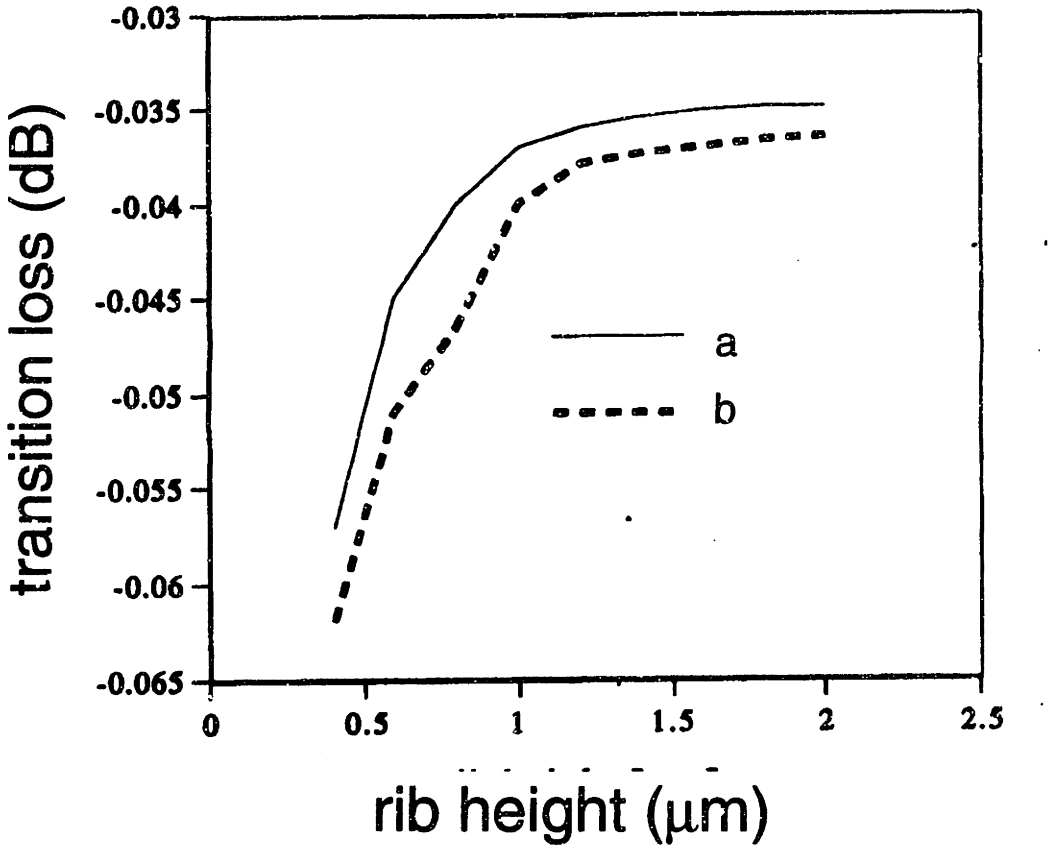

Figure 4-7: Transition loss L plotted for various rib heights h_4. In top curve, only the height of the curved rib varies while the height of the straight rib remains constant at $h_4 = 1.4\,\mu$m. In the bottom curve, both heights are equal.

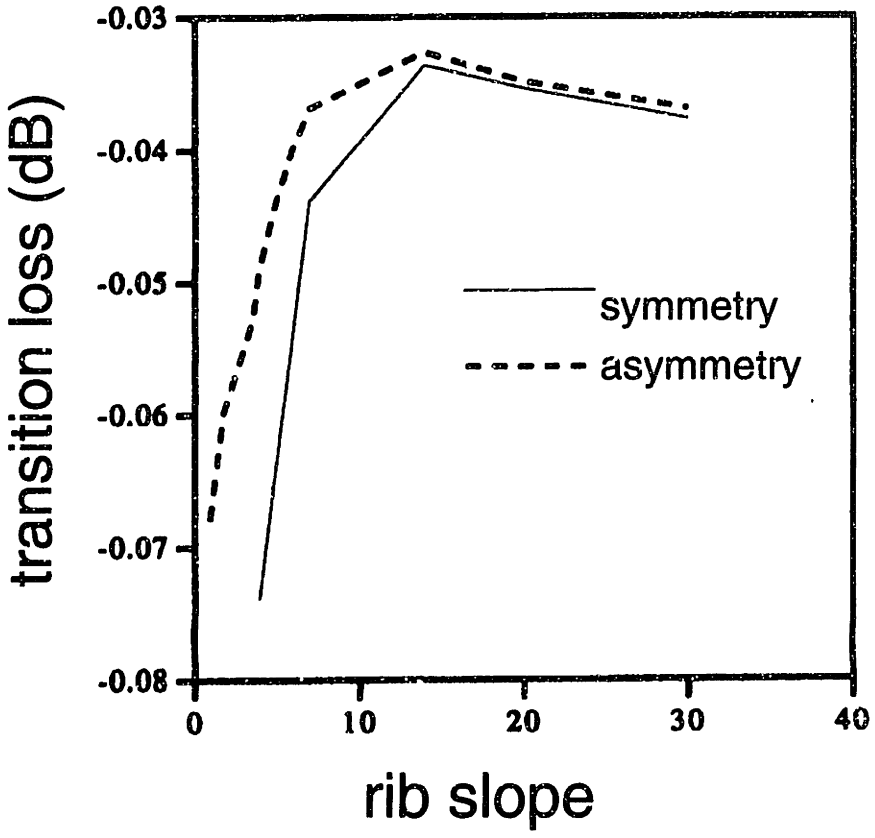

Figure 4-8: Transition loss L plotted for various sidewall slopes. The solid line shows the symmetric case where the two rib sidewalls have equal slopes. For the dotted line, the inner sidewall is vertical while the outer sidewall varies.

walls does lower the transition loss. The solid line in figure 4-8 plots the transition loss for various sidewall slopes. Changing the slope of the sidewall is a very small effect.

In figure 4-3 the mode of the curved waveguide is asymmetric while the straight mode is symmetric. The trench asymmetrizes the index distribution by lowering the index at the large radii. But none of the previous schemes asymmetrizes the index distribution in the rib itself — where most of the power lies. A way to do this is to have different slopes for the left and right sidewall. Hopefully, the asymmetry in the rib will cancel or counter the asymmetry induced by equation (4.1). Clearly, this is very difficult to achieve experimentally. Perhaps, the substrate needs to be tilted during dry etching. Let's see what happens if the left or inner sidewall were vertical, but the slope of the right sidewall varies. The dashed line in figure 4-8 plots the transition loss as a function of tthe right wall's slope. This reduction in loss from

changing the rib index shows the deleterious effect of mode asymmetry.

Now, we combine the optimal values for guide offset $x_{off} = 0.5\,\mu$m, rib width $w = 2.4\,\mu$m, trench–to–rib separation $w_d = 2.00\,\mu$m, rib height $h_4 = 1.4\,\mu$m, and rib slope 14. This gives a transition loss of only -0.033 dB. All the above calculations applied to fields that are polarized such that the electric field is in the x direction (horizontal and in the page). If the fields were scalar, the transition loss is -0.029 dB. There is roughly a 10% difference between scalar and semi-vectorial calculations. Figure 4-9a is a contour plot of the fundamental mode (E_x)of the straight rib. This mode looks very similar to the mode of the curved rib (figure 4-9b). Compared to figure 4-3, the light is confined better and shaped better.

4.4 Conclusion

We have lowered the transition loss between straight and curved rib waveguides. We have optimized the offset between guides, the position of the trench, width of the rib, height of the rib. Also, we find that the effects of rib slopes and the asymmetry of index profiles lead to only second order reductions in the transition losses.

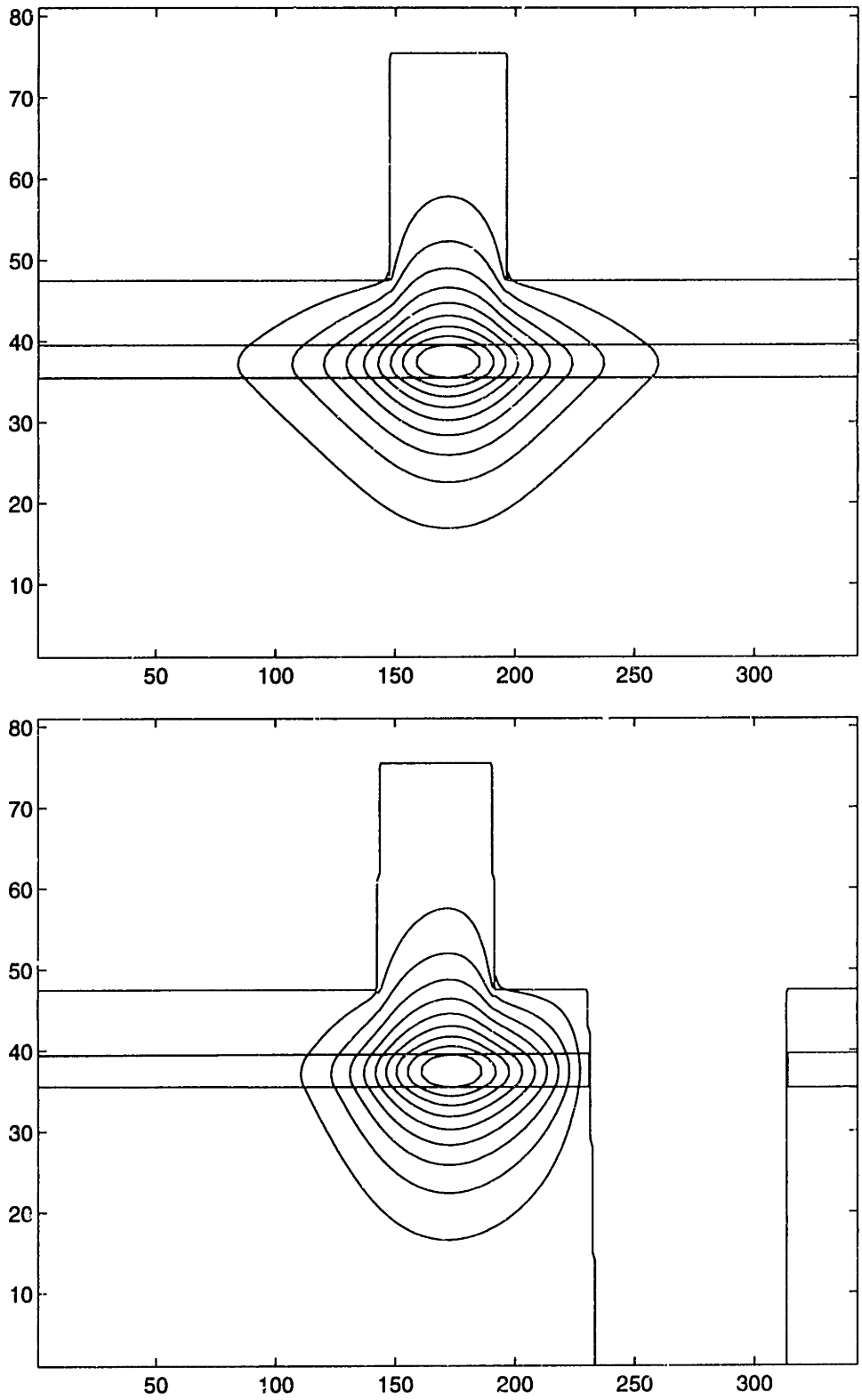

Figure 4-9: Top: Eigenmode of straight rib waveguide. Bottom: Eigenmode of curved rib waveguide, with optimized guide offset, trench position, rib width, and rib height.

Chapter 5

A modified Finite Difference Time Domain code

Summary:

We apply a two dimensional, scalar-like finite difference time domain code to optical waveguides. In particular, we modify the program to measure reflection and transmissions of air bridge filters. The quality factor obtained from these transmission results are consistent with that calculated from resonator's energy decay.[1]

5.1 Introduction

Scalar finite difference codes have been used in acoustics. We show how such codes can be adapted to model the vector waves, such as those found in microwaves and optics. For a 2D geometry, our adaptation permits the calculation of field components perpendicular to the solution domain. In addition, we present a new way to separate forward and backward propagating fields. This allows the efficient calculation of reflection and transmission coefficients. This code has been validated with a resonant air bridge filter. We also formulate expressions for fluxes and energies, to describe this filter's resonator properties. Compared to traditional, vector FDTD codes, this

[1] Portions of this chapter have been published in the proceedings of a referred conference[68] and as a chapter of a book.[69]

scalar-like approach saves memory and simplifies coding.

5.2 Governing equations

Standard finite difference time domain programs integrate Maxwell's equations. To improve accuracy, these programs displace the electric field at a half grid point from the magnetic field. Our program calculates only one field component, avoiding the additional complexities and memory requirements associated with staggered grids. For the TE case, the vector wave equation becomes scalar.

$$\frac{\partial^2 E(x,y,t)}{\partial x^2} + \frac{\partial^2 E(x,y,t)}{\partial y^2} - \frac{n(x,y)^2}{c^2}\frac{\partial^2 E(x,y,t)}{\partial t^2} = 0.$$

where E is the electric field in z direction and n is the index of refraction. The equation we solve for 2D TM case is

$$\frac{\partial}{\partial x}\left(\frac{1}{n(x,y)^2}\frac{\partial H(x,y,t)}{\partial x}\right) + \frac{\partial}{\partial y}\left(\frac{1}{n(x,y)^2}\frac{\partial H(x,y,t)}{\partial y}\right) - \frac{1}{c^2}\frac{\partial^2 H(x,y,t)}{\partial t^2} = 0.$$

where H is the magnetic field in the z direction. From E_z and H_z, the other polarizations can be derived using the Maxwell curl equations.

For second order accuracy, all the derivatives are center differenced. These equations are explicit and so are easy to code. Furthermore, each field quantity at a given time step is independent of fields at the same time step; there are no data dependencies. So, an initial value calculation can run efficiently on parallel[35] as well as vector machines. The boundary conditions we use are second order absorbing.[37] We use the finite difference program in two ways, to get either the transmission spectrum or the resonator properties.

By examining the resonator properties, we can extract the quality factor Q. To extract the quality factors, we need to find the field profile of that resonator eigenmode. An arbitrary initial field can be decomposed into many eigenmodes, each of which decays exponentially with a rate ω/Q. A sufficiently long propagation will yield the mode with the largest Q; the other eigenmodes will be negligibly small.[73] Of course,

this calculation can be speeded up if the initial field resembles the high Q eigenmodes. By monitoring the rate of energy decay, we obtain the Q of the eigenmode. The energies are defined as

$$\begin{aligned} W^{TE} &= \frac{1}{2}(\frac{n}{c}\frac{\partial E}{\partial t})^2 + \frac{1}{2}(\frac{\partial E}{\partial x})^2 + \frac{1}{2}(\frac{\partial E}{\partial y})^2 \\ W^{TM} &= \frac{1}{2}(\frac{1}{c}\frac{\partial E}{\partial t})^2 + \frac{1}{2}(\frac{1}{n}\frac{\partial E}{\partial x})^2 + \frac{1}{2}(\frac{1}{n}\frac{\partial E}{\partial y})^2. \end{aligned}$$

The corresponding fluxes are

$$\begin{aligned} F_x^{TE} &= -\frac{\partial E}{\partial x}\frac{\partial E}{\partial t} \\ F_x^{TM} &= -\frac{1}{n^2}\frac{\partial E}{\partial x}\frac{\partial E}{\partial t}. \end{aligned}$$

The external quality factor Q_e is defined as the fractional energy coupled to the waveguide in a cycle. This is derived from integrating the flux. The total quality factor Q of the resonator can be calculated from the decay of energy W or the escape of flux F. There is good agreement between the two.[2]

For the transmission spectrum, we launch a monochromatic sinusoidal wave from one end of the waveguide. The next chapter discusses the effect of a gaussian time dependence. The transverse profile of this source is the guide's fundamental mode. The field is explicitly stepped forward in time until steady state is reached. From the field values at two different positions and times, we separate out the forward and backward propagating wave components.

$$E_f \cos(kx - \omega t + \Phi_f) = -\hat{A} + \hat{B} \quad (5.1)$$

$$E_b \cos(kx + \omega t + \Phi_b) = \hat{A} + \hat{B} \quad (5.2)$$

[2]I find small discrepancies using the 2D vector code. Shanhui maintains that the 3D vector code is fine.

where

$$\hat{A} = \frac{E(x,t+\Delta t) - \cos(\omega\Delta t)E(x,t)}{2\sin(\omega\Delta t)}$$
$$\hat{B} = \frac{E(x+\Delta x,t) - \cos(k\Delta x)E(x,t)}{2\sin(k\Delta x)}.$$

Choosing Δx and Δt so that the differences — $\hat{A}$ and $\hat{B}$ — are large, enhances accuracy. One can solve for the amplitudes E_f and E_b by evaluating equations 5.1 and 5.2 at an additional time step. And by taking the ratios of various field components before and after the filter, we obtain the reflection and transmission coefficients. The radiation power is defined as the incident power minus the power transmitted and the power reflected. This includes the power transferred to higher order transverse modes and to the substrate. For photonic band gap materials, others have calculated transmission and reflection through transfer matrices[82, 160] and transmission and radiation through beam propagation methods.[84] To the best of our knowledge, this is an original way to measure all three: reflection, radiation and transmission.

5.3 Application to resonant filters

Here, we validate or test this scalar-like FDTD code. This code can be applied to any two dimensional geometry. For example, we can model how a CW wave propagates through a series of dielectric blocks, whose index is 1.88. The blocks measure 0.58 by 0.14 wavelengths, while the air gap between adjacent blocks is 0.2544 wavelengths. The center post or block is 0.2776 wavelengths long. Figure 5-1 shows the electric field whose frequency is at transmission resonance. We can also model circular posts that are composed of a silicon nitrate ($n_{eff} = 1.8821$) layer on top of silicon oxide ($n_{eff} = 1.3586$). Figure 5-2 shows the scattered radiation interfering with the incident light, also at the frequency of transmission resonance. In the rest of this chapter, we will focus on a filter constructed from the more familiar air bridge geometry (figure 5-3). This example allows us to test both the transmission and resonator properties.

Now, how does this filter work? A distributed feedback (DFB) grating waveguide

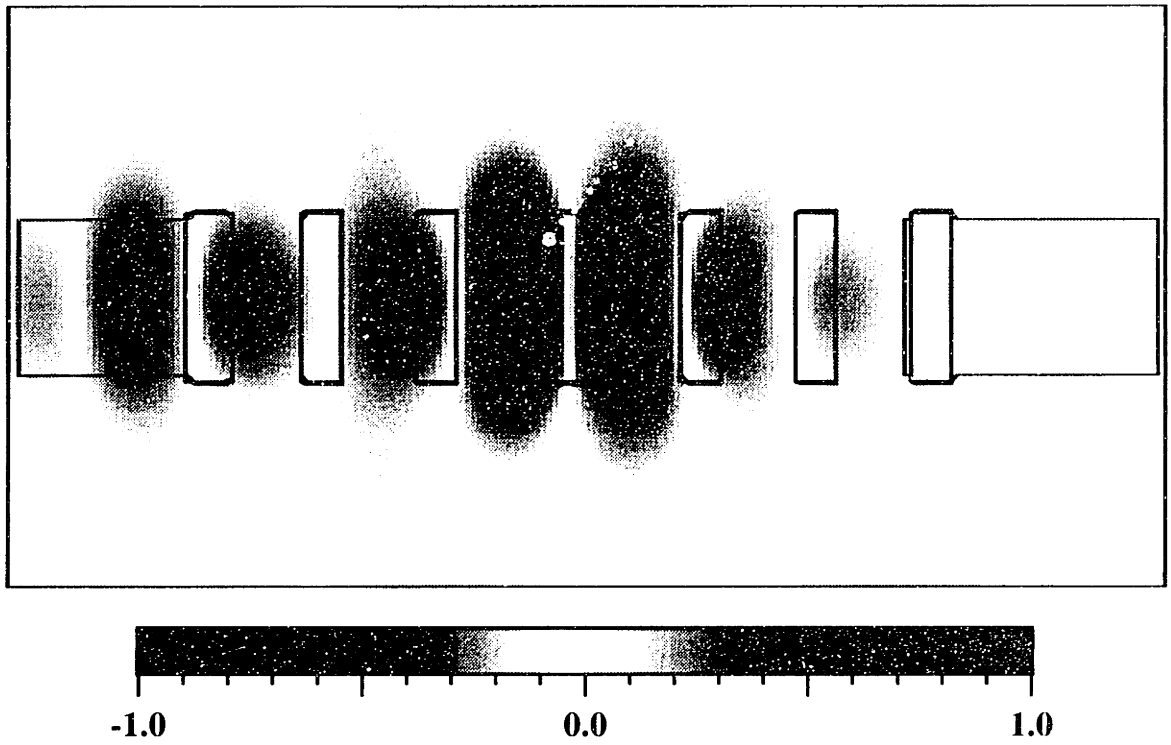

Figure 5-1: Contour plot of light transmitted through dielectric blocks.

acts as a reflection filter in the stopband of the grating. If a quarter-wave shift (QWS) is introduced in the center of the grating, a transmission resonance occurs in the center of the stopband. A QWS-DFB grating waveguide side-coupled to a bus (or "signal") waveguide can acts as a channel dropping filter that drops from the bus the channel with a carrier frequency coincident with the resonance of the grating resonator. The other frequencies remain on the bus waveguide. Such add/drop filters may find application in wavelength division multiplexing systems. In order to cover a set of channels over the bandwidth of erbium amplifiers, gratings are required with a stopband twice that of the erbium gain (approximately 40 nm). Only the large index contrasts found in photonic band gap materials can create such large stopbands. Other potential applications of photonic band gaps include curved waveguides with low losses, laser resonators with low spontaneous emission, and efficient radiation from planar antennae.[74, 117, 119, 130, 161]

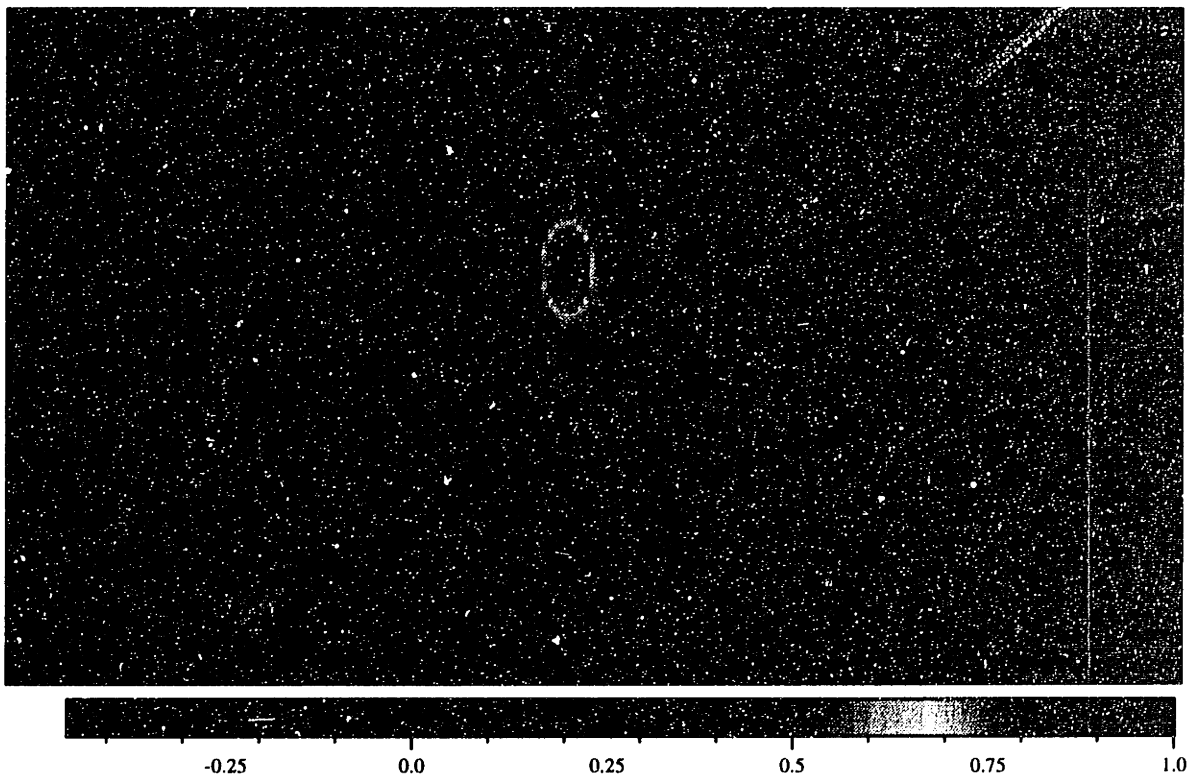

Figure 5-2: Contour plot of light scattered from Si_3N_4/SiO_2 posts.

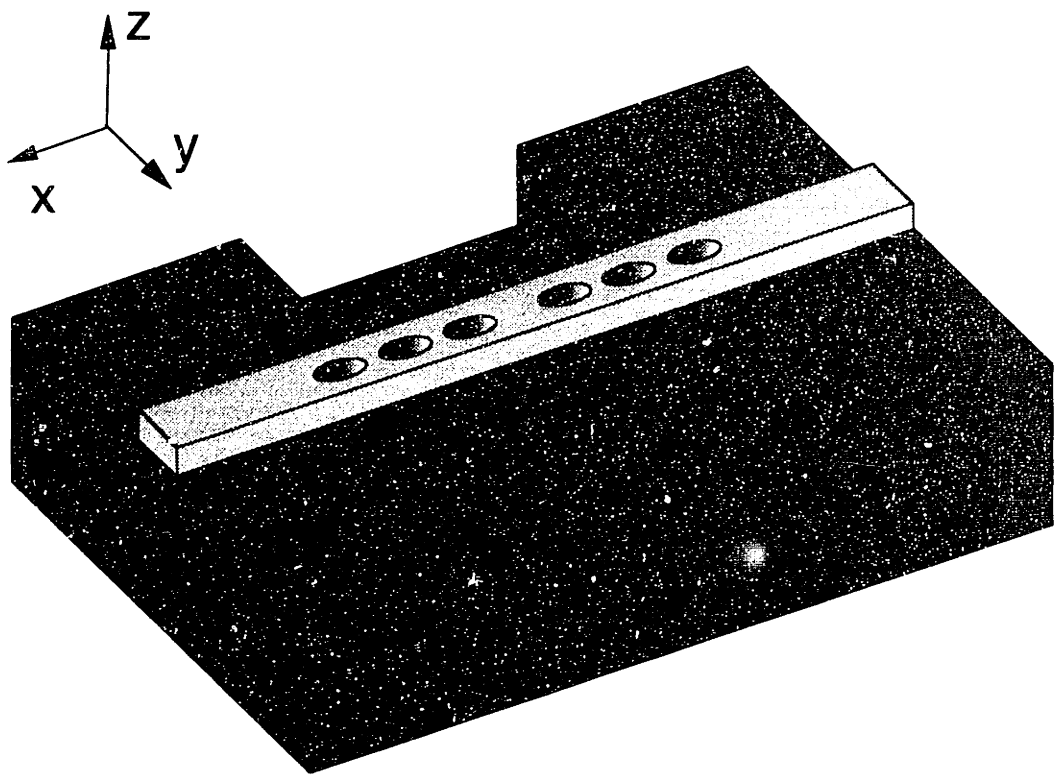

Figure 5-3: Air bridge with six circular holes. drawing by P. R. Villeneuve.

5.3.1 Resonator properties

For the air bridge structure shown in figure 5-3, we examine a cross section. The index of refraction is $n = \sqrt{13}$. This air bridge has only six circular air holes. In particular, the period or hole-to-hole spacing is 0.232 λ or (for $\lambda = 1.5\,\mu$m) 0.348 μm. This spacing increases to 0.325 λ or 0.487 μm for the center two holes. The air holes have a 0.167 λ or 0.250 μm diameter, while the air bridge is 0.151 λ or 0.226 μm wide. A longer version of this structure — one with more air holes — can act as a high Q microcavity.[73, 108] Figure 5-4 shows the magnetic field profile of the highest Q eigenmode. It is TE. The magnetic field has even symmetry, so the electric field would have odd symmetry. Figure 5-5 shows the energy decay for an initial excitation. The slope gives the Q. Figure 5-5 shows a Q of 387. This is a surprisingly large Q for a structure that has only 3 air holes. The total structure is less than 1.5 wavelengths long! This small size allows for a compact integration of many wavelength filters on a small chip.

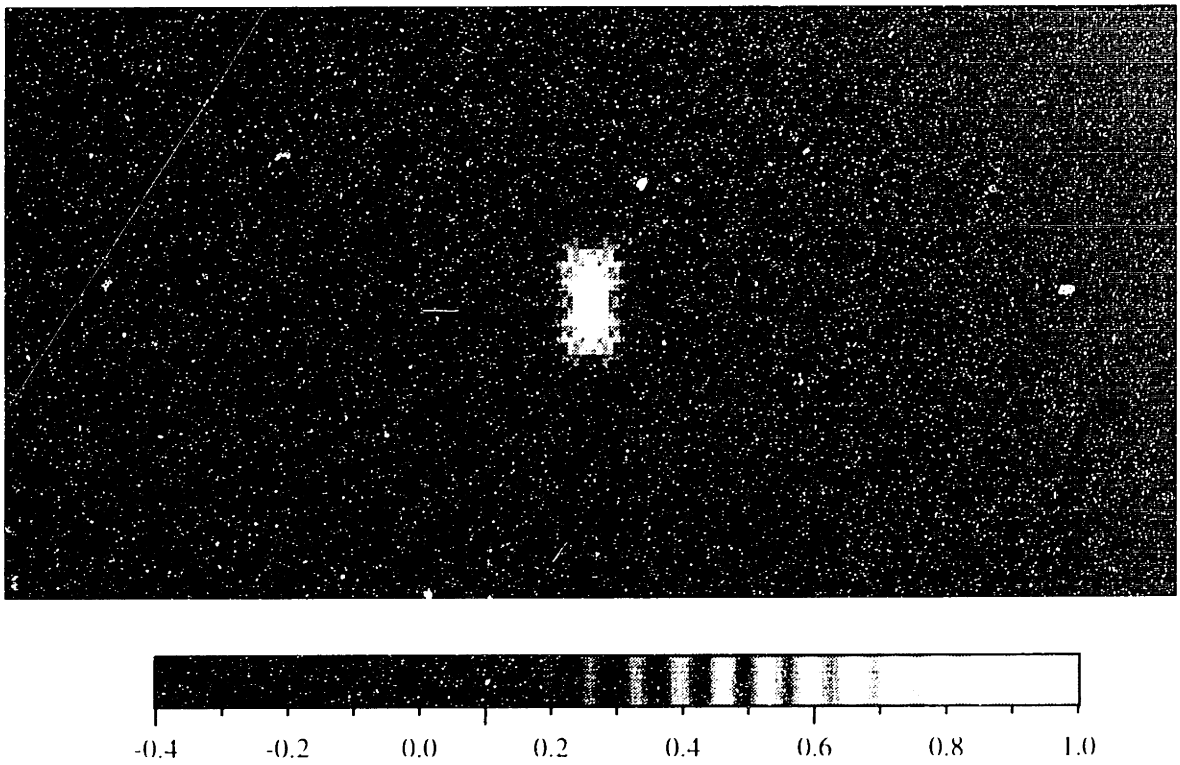

Figure 5-4: Grayscale contour of TE magnetic field (normal to page), showing the eigenmode with the highest Q.

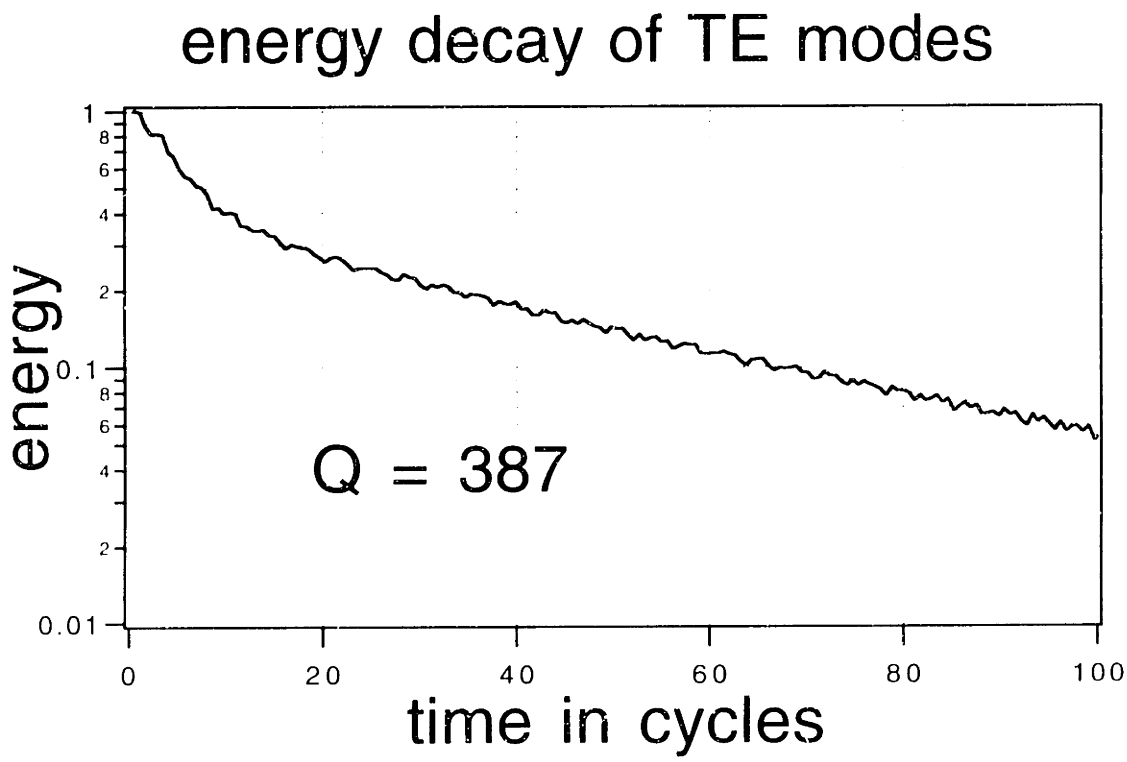

Figure 5-5: Energy in TE fields plotted versus number of cycles

The fields in figure 5-4 are strongly localized about the dielectric defect or phase slip. The exponential decay of the field from its maximum can be approximated by a decay constant $\kappa = -\frac{\Delta n}{<n>}\frac{2}{\Lambda}$ where Λ is the grating period, Δn is the difference in effective indices of the air hole and dielectric guide, and $<n>$ is the average index of the hole and dielectric.,[162] For photonic band gap materials, Δn is large. In some cases, $\Delta n \simeq <n>$ so κ is on the order of the free space wave vector. This strong localization of electric field means a large spread of the mode's spatial Fourier spectrum. Radiation occurs when the spectrum extends into the radiation mode spectrum. An analytic approximation for the radiation Q has been formulated.[163] The Q_{ext}, associated with the coupling of the resonator to the input and output waveguides, is derived in Prof. Haus' book.[162]

$$Q_{ext} = \frac{l}{\lambda}\frac{\pi c}{v_g|\kappa|l}e^{2|\kappa|l} = \frac{l}{\lambda}\frac{<n>}{|\kappa|l}e^{2|\kappa|l}.$$

The total Q of a resonator is

$$1/Q_{total} = 1/Q_{ext} + 1/Q_{rad}.$$

For the TM air bridge, the analytic theory makes the following predictions: $Q_{rad} = 500$. $Q_{ext} = 551$. $Q_{total} = 262$. The total Q is comparable to the numerically derived $Q = 387$.

5.3.2 Transmission spectra

Higher Q resonators lead to a sharp transmission peak within the stop band. Figure 5-6 shows the transmission, reflection, and radiation as a function of frequency. Here the transmission coefficient is the fraction of power that remains in the fundamental transverse mode of the waveguide after propagating through the air holes. The transmission resonance occurs at $\lambda = 1.5\mu$m or 200 THz. In figure 5-7, a monochromatic laser source comes in from the left side of the filter. Since the source oscillates at the resonance frequency of the cavity, light is coupled into the resonance mode (figure

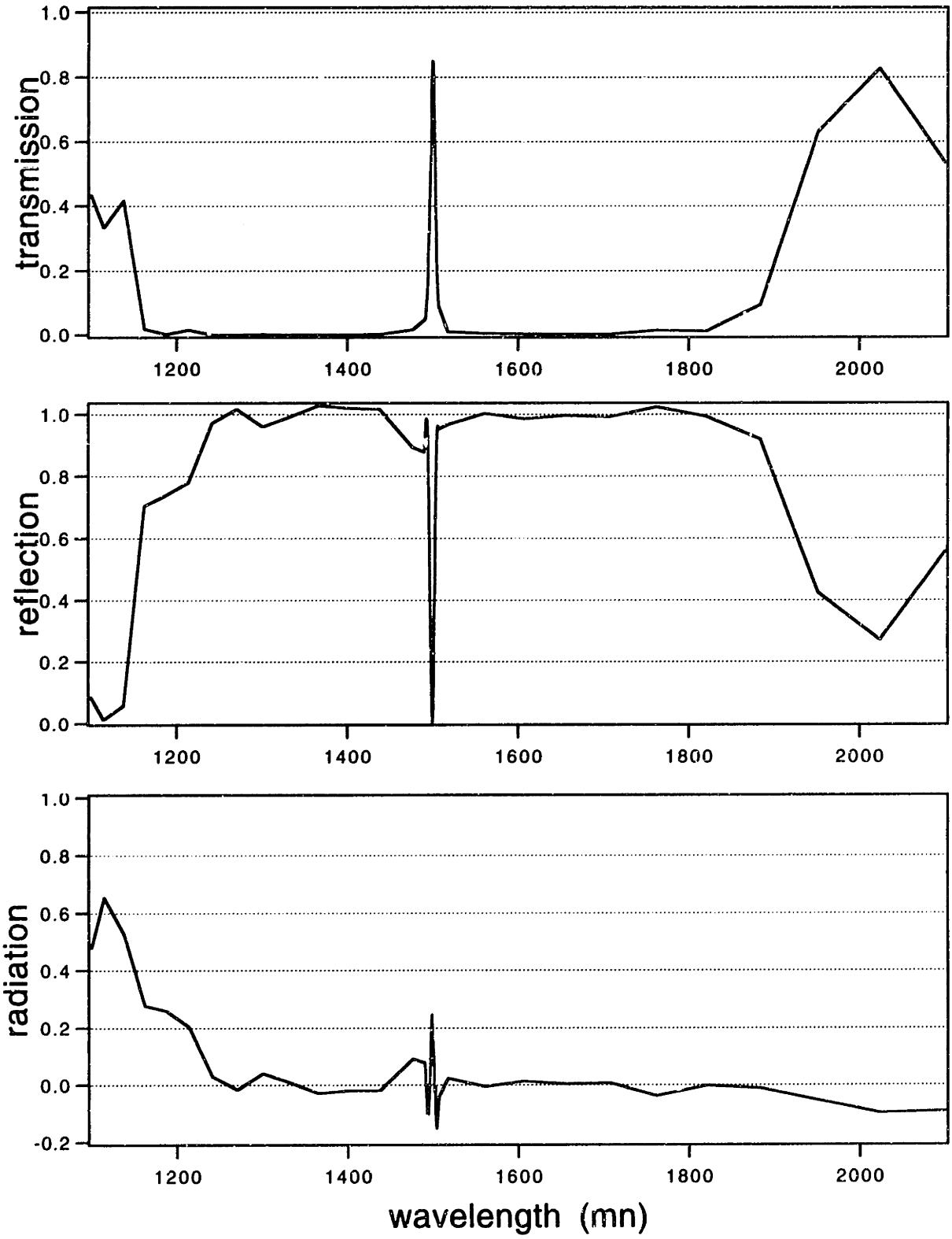

Figure 5-6: Fraction power transmitted, reflected, and radiated through filter as a function of frequency

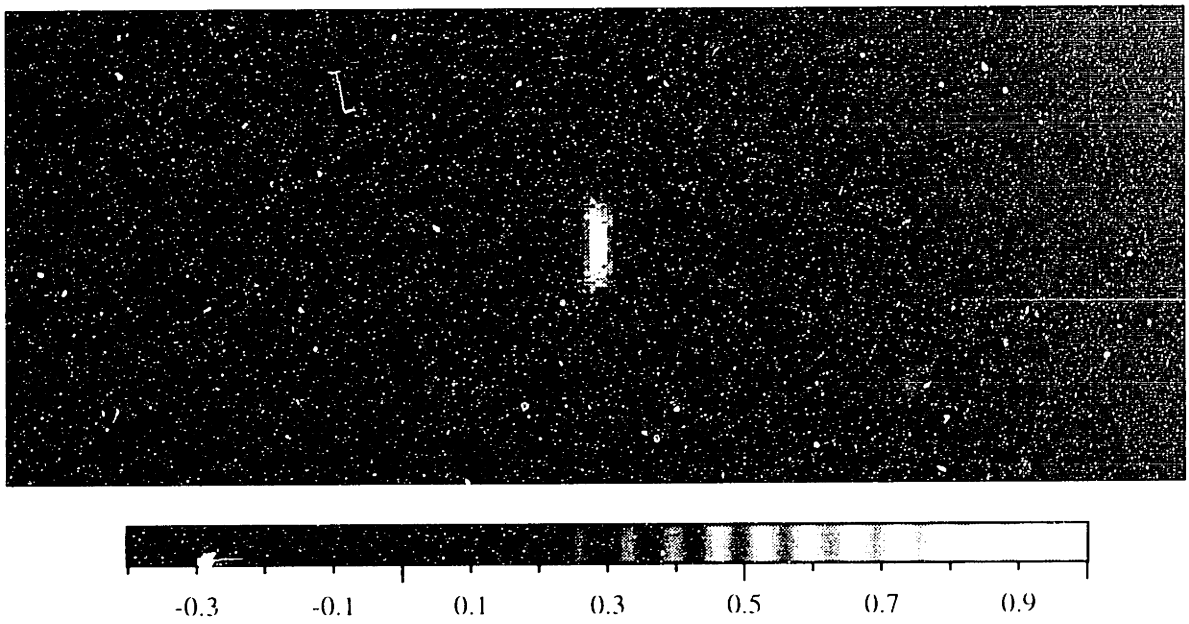

Figure 5-7: TE magnetic field propagates down air bridge filter at transmission resonance. NOTE: vertical scale is expanded.

5-4), creating strong field localization about the phase slip or dielectric defect. At this frequency, the transmission is nearly perfect; 87 % is transmitted. The Q from the FWHM of that resonance is 304. The size of the stop band is 600 nm! This is about 40% the center wavelength. Reflection and radiation are also plotted. Over much of that range, the reflection is near unity and the radiation near zero. For higher frequencies, the radiation increases since light is transferred to higher order transverse modes. At resonance, the loss due to radiation is surprisingly small despite the sharp decay (large κ).

5.3.3 Tuning ability

This scalar-like FDTD code can also calculate this filter's tuning characteristics. Here, we vary the size of the dielectric defect or phase shift, by adding more dielectric between the two center holes. This lengthens the bridge. The phase shift is calculated by multiplying the effective index by the additional length. Zero phase shifts mean the filter is perfectly periodic; the spacings between the circles are constant. This bridge differs from the air bridge of figure 5-3 in that now we have 14 cirular holes.

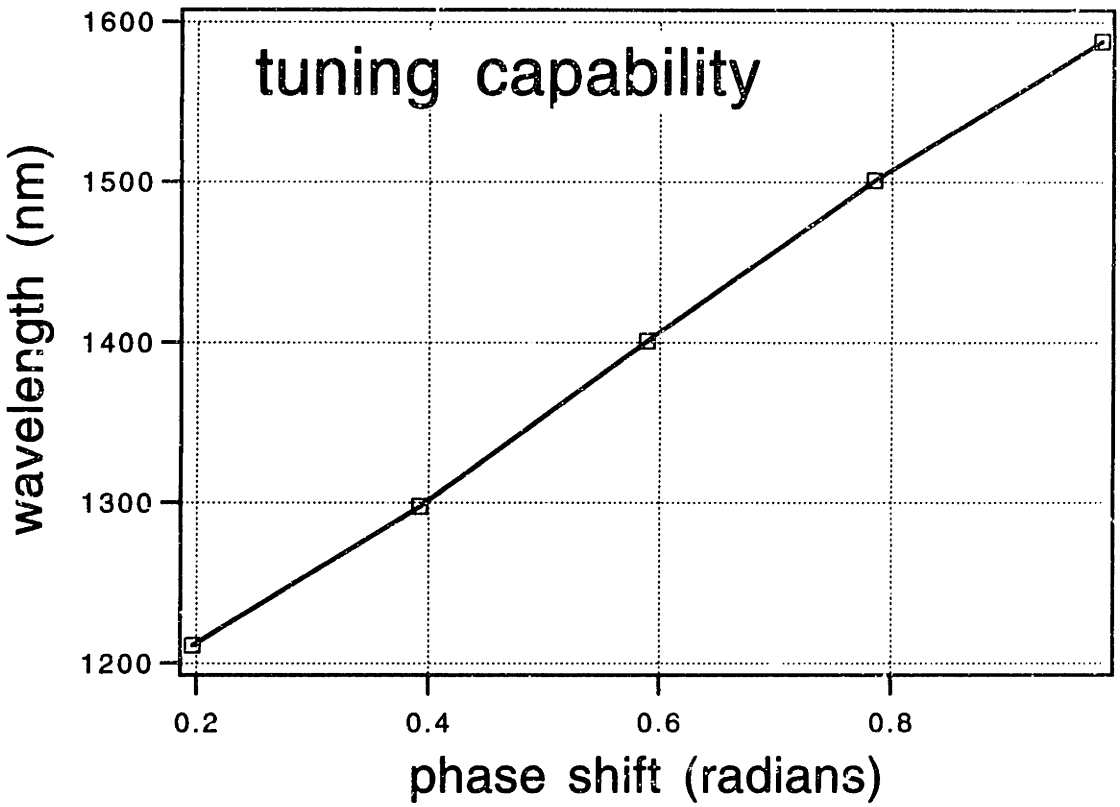

Figure 5-8: Tuning capability of bridge with 14 circular holes.

instead of 6. Figure 5-8 shows that the resonant wavelength of this resonator (and filter) increases with the phase shift. Tuning across 400 nm is possible. These filters and resonators work over an enormous frequency range.

But unfortunately, the quality factor is very sensitive to frequency changes, varying by factors of 10 (figure 5-9). The quality factor peaks at $Q = 4000$ at wavelength $\lambda = 1500$ nm. This is approximately a quarter wave or $\pi/4$ phase shift. Radiative losses shifts the optimum phase from $\pi/4$ — which analytic methods prove is optimum for lossless gratings.

5.4 Conclusion

We have presented a modified finite difference time domain method that is conceptually easier to code and reduces the storage requirements of the dielectric medium. Our enhancements permit the calculation of reflection and transmission coefficients

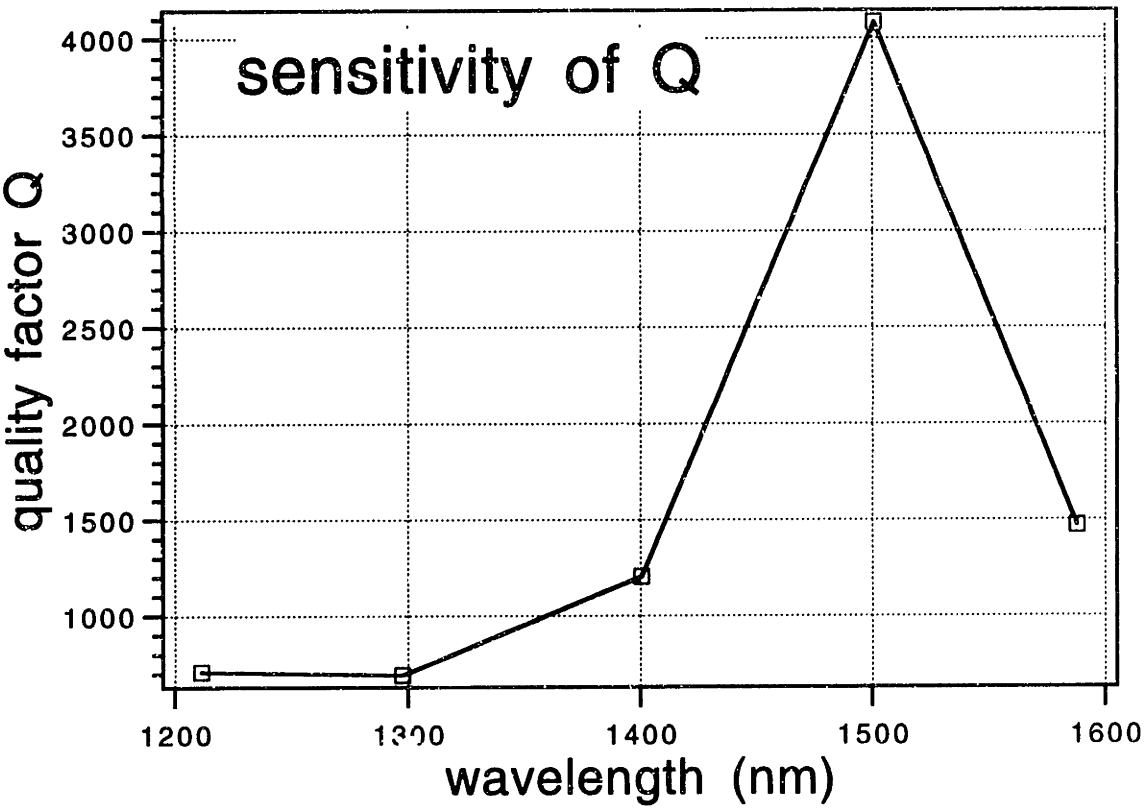

Figure 5-9: Sensitivity of quality factor Q to resonant wavelength.

for cw waves. Energy and flux conservation is also demonstrated. We use the air bridge resonant filter as an example. This filter is highly tunable.

Chapter 6

Parallel supercomputers

Summary:

Efforts to port the scalar-like finite difference time domain code from a single to multi- processor machine are presented. Parallel processing on a Thinking Machine CM-5 is compared to vector processing on a Cray C90. The parallel supercomputer allows for larger domains and runs faster for some boundary conditions.[1]

6.1 Introduction

Compared to single processor computers, parallel computers can solve larger problems with increased computational speed, by sub-dividing the problem among many separate CPU's. How the problem is sub-divided affects the performance greatly. For maximum performance, all the processors should be equally busy; the computational load should be balanced. One processor should not be idle while waiting for data from neighboring processors. In the multi-instruction multi-data (MIMD) model, each processor may work on a different instruction from its neighbor. Such computers can be difficult to program. Single-instruction multi-data (SIMD) or data parallel computers tend to be easier to program. There a single instruction is computed by all the

[1] Portions of this chapter have been published in a conference proceeding.[35] The slides from this talk can be found on the world wide web at http://www.nchpc lcs.mit.edu/Workshop94/Slides/s2_p201.html.

processors at the same time. Thinking Machine's Connection Machine can be used in the SIMD fashion. In the past, some researchers have ported vector finite difference time domain (FDTD) codes to various Connection Machines: CM,[164] CM-2,[165,166] and CM-5.[167,59] v In this chapter we present a parallel implementation of the scalar-like FDTD method, described in the previous chapter. Unlike vector treatments, this scalar-like model does not suffer from the complexity of a staggered grid nor from the need for additional storage.[67] In addition, we compare the newest parallel machine by Thinking Machine (CM-5) with a very fast, single processor supercomputer by Cray (C90). And for the first time to our knowledge, we present a detailed study on the role of boundary conditions.

6.2 Advantages of parallel computers

Finite difference time domain (FDTD) methods are important for modeling the evolution of optical beams in 2D and 3D waveguides of arbitrary refractive index profiles. Unfortunately, this technique is computationally intensive, so only small structures can be studied. Parallel computers permit the study of large structures.

The equation we solve is the scalar wave equation

$$\frac{\partial^2 E(x,y,t)}{\partial x^2} + \frac{\partial^2 E(x,y,t)}{\partial y^2} - \frac{n(x,y)^2}{c^2}\frac{\partial^2 E(x,y,t)}{\partial t^2} = 0,$$

where $E(x,y,t)$ is the electric field, x and y are the 2 spatial dimensions, t is time, c is the speed of light, and $n(x,y)$ is the index of refraction. Centered-Time Centered-Space differencing about $E^n_{i,j} = E(i\Delta x, j\Delta y, n\Delta t)$ yields

$$E^{n+1}_{i,j} = 2E^n_{i,j} - E^{n-1}_{i,j} + \frac{c^2\Delta t^2}{(n_{i,j})^2}\left(\frac{\delta_i^2}{\Delta x^2} + \frac{\delta_j^2}{\Delta y^2}\right)E^n_{i,j}, \tag{6.1}$$

where δ_i and δ_j are center difference operators. This equation is explicit so is easy to code. Furthermore, each field quantity at $t = (n+1)\Delta t$ is ind' ndent of fields at the same time step. Numerical analysts tend to represent th rially with a "stencil" drawing. The resulting field, represented by a white ball, depends on those

fields represented by black-colored balls (figure 6-1a). So, an initial value solution of equation (6.1) is block oriented; there are no data dependencies. Such algorithms can run efficiently on SIMD parallel machines. If each of the N spatial (x, y) grid points were assigned to a processor, then the algorithm runs $O(N_t)$, where N_t is the number of time steps. This can be shown in the "stencil" in figure 6-1b. The fields at all x and y points are updated in one time step. In contrast, a single processor computer would require $O(N_t \cdot N)$ steps. In addition, since there is no need to store a large matrix, the memory requirements are 3 N; only 3 time steps need to be stored.

To port the FORTRAN77 program to the CM-5 fortran, we used the Thinking Machine converter *cmax* with several *NODEPENDENCE* directives. Then a few *LAYOUT* directives were necessary. Such directives tell the converter why a particular loop can be parallelized and how the electric field should be distributed between processors. Our code allows for four different boundary conditions. The Neumann and Dirichlet boundary conditions were parallelized. Periodic and absorbing[37] boundary conditions can be in principle parallelized but *cmax* had difficulty converting them; only after some recoding, did the code for absorbing boundaries convert properly.

6.3 Comparison between Connection Machine and Cray

In this section we compare the fastest publicly-available single processor machine with the fastest publicly-available parallel computer. These simulations were performed in the summer of 1994. The single processor machine is the Cray C90 at NSF's San Diego Supercomputer Center. Its vector processor is rated at 0.95 GFlops. The maximum RAM we could access then is 64 MWord or 512 Mb. The parallel machine is Thinking Machine's CM-5. Its free use comes courtesy of Project Scout and M.I.T's Laboratory of Computer Science. We were able to use all 128 processors with an aggregate speed rating of 7.7 GFlops and with a combined physical memory of 4 Gb.

First, I tried to port a small subset of the program. In particular, I worked on

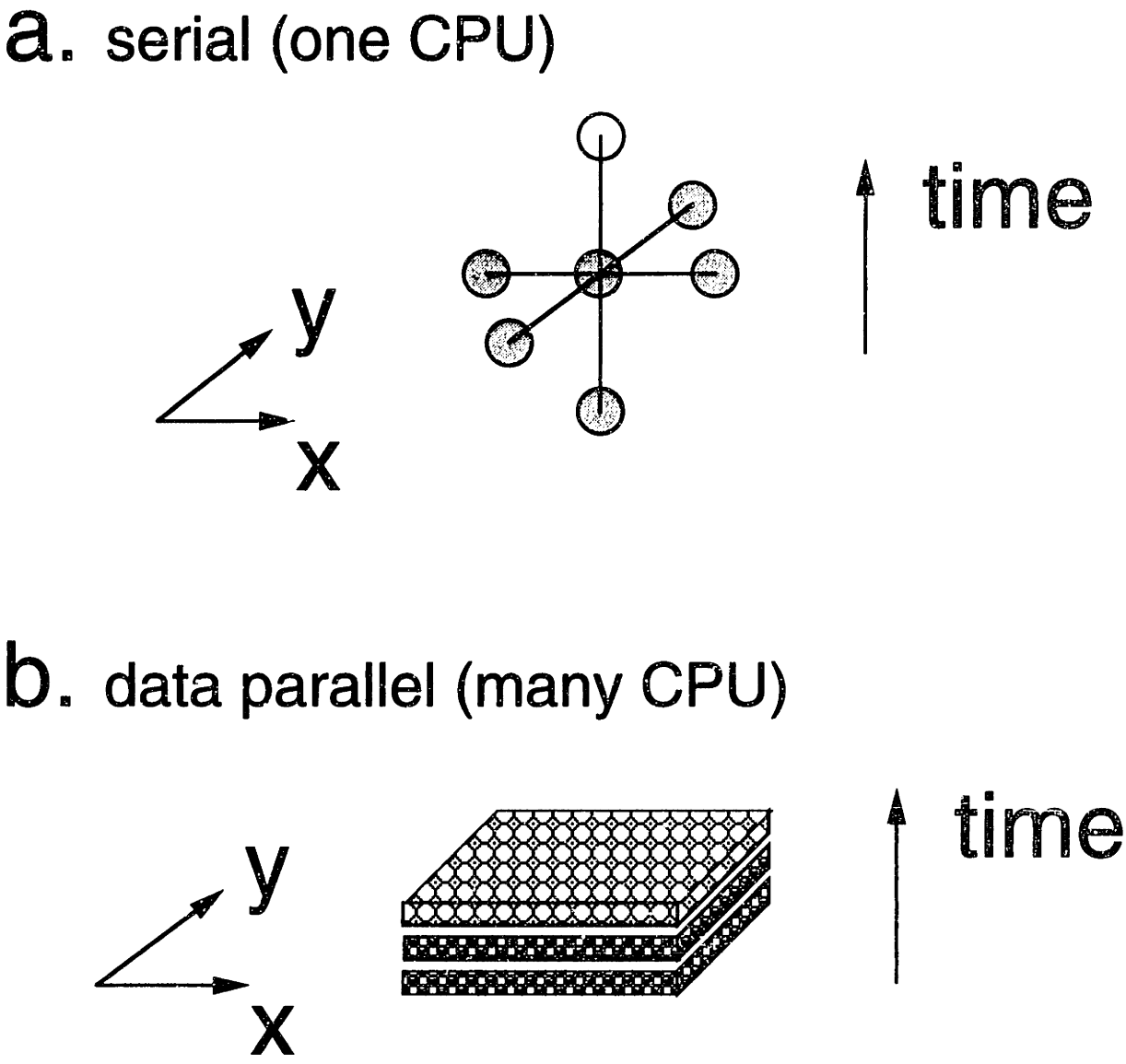

Figure 6-1: "Stencils" representing how the fields (balls in white) depend on other fields (balls in black), for computers with **a.** one processor and **b.** many processors.

the propagation subroutine, which updates the fields at the interior grid points, and the boundary subroutine, which calculates the field at the exterior points. For the propagation routine, the execution time was reduced by about 30 % by rearranging terms such that all the shifts occurred before the calculations. This reduces the time spent waiting for data from neighboring processors. An additional 10% speed-up comes from expliciting specifying the calculated array sections.[2] Figure 6-2 plots the number of seconds spent updating one field point. This is plotted for both the C90 and the 128 node (processor) CM-5, for varying amounts of spatial points. In this test, I ran 100 iterations over a square grid with Dirichlet ($E = 0$) boundaries. Both computers are relatively inefficient for small number of grid points; if there are only a few grid points at each processor, the interprocessor communication is high. For small domains, the Cray is faster; its vector length is less than the CM's block size. For squares exceeding 2000 grid points, the CM-5 is faster. For the largest problems, the CM-5 is about 40 times faster! This is better than expected from the Linpack MFlop rating. Such time stepping is well-suited to parallel machines with SIMD architectures.

In addition, parallel computers tend to have larger aggregate memories than single CPU machines, because addressing enormous amounts of RAM from one CPU requires many bits to specify a particular memory location uniquely. Because the CM-5 has about 8 times as much total memory, it can solve FDTD problems with larger grids. To find each machine's limit, I kept incrementing the grid size until the computer crashed. The maximum grid handled by the 0.512 Gb C90 was a square of 2880x2880 points. The 4.0 Gb CM's largest grid measured 4800x4800. It can handle grids that are about 2.8 times bigger! [3]

Next, I used CMAX to translate the entire FDTD program, and then added the optimized propagation routines. Figure 6-3 shows the results of running the whole

[2]For 1000 iterations through a grid of 135 x 49, the execution time on a 32 node (or processor) CM is 0.276 seconds. Rearranging the shifts lowers the time to 0.196. Using array sectioning notation reduces the time to 0.166 seconds.

[3]Although the memory is 8 times larger, CM can not run grids that are 8 times larger, because it needs to replicate the program code at all the CPU's.

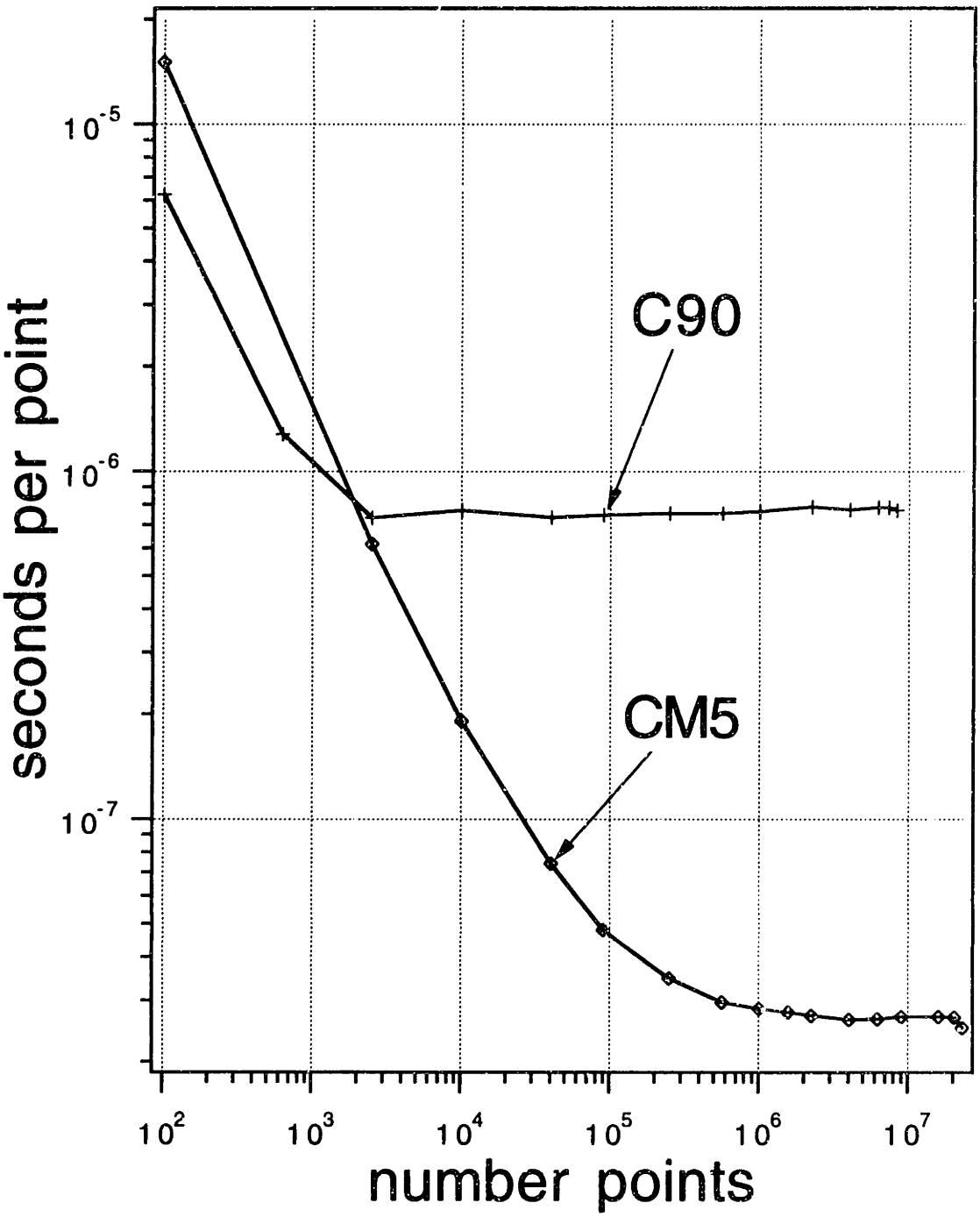

Figure 6-2: Seconds needed to update one field point, as a function of number spatial points in a square grid.

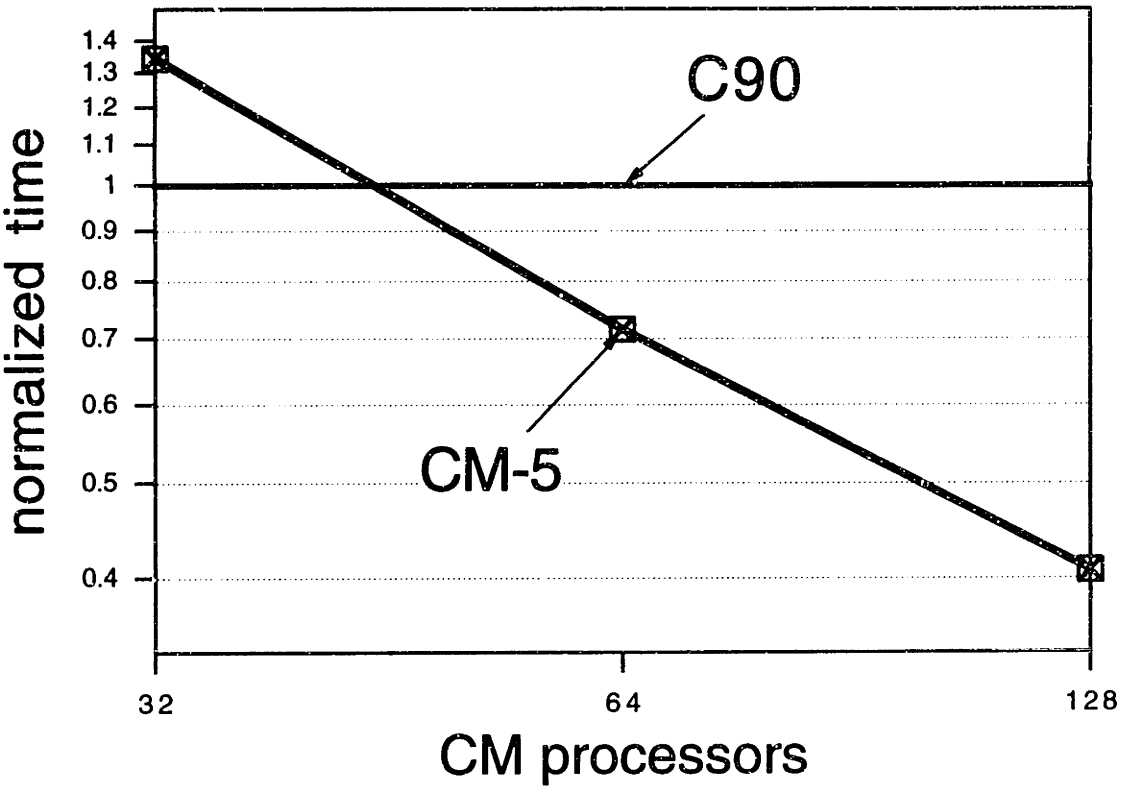

Figure 6-3: Execution time of Connection Machine as a function of number of processors, normalized to Cray's computation time. Boundary is $E = 0$.

program for 50 cycles, as a function of number of CM processors or nodes. The grid is not square but is rectangular (1000x300 grid points). The line is linear meaning the program is well-parallelized. Serial operations are at a minimum. The execution time of the 32 processors is about 90 % of four times the total time used by 128 processors. This roughly 90% speedup is very good for parallel codes. It is not 100% due to inter-nodal communication. The 128 node CM-5 is still faster than the Cray, but only 3 times faster. In contrast, the propagation and Dirichlet boundaries ran 40 times faster on the CM-5. Perhaps the overhead associated with the variable setup, I/O interface and energy/flux calculations reduced the speed.

Figure 6-4 presents the execution times for the entire FDTD code, using exactly the same parameters but now using absorbing boundary conditions. On two sides the boundary is second order,[37] while the other two use first order. On the Cray the codes slows down about a few percent, but on the Connection Machine the program

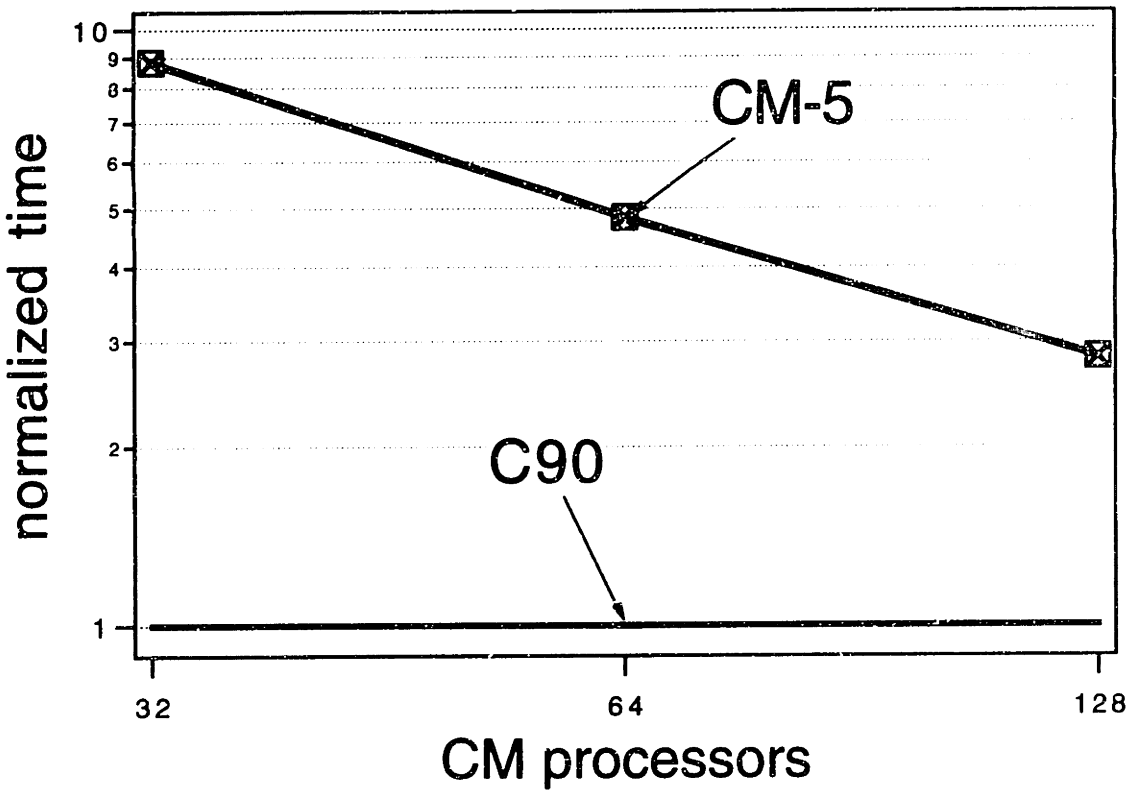

Figure 6-4: Execution time of Connection Machine as a function of number of processors, normalized to Cray's computation time. Boundary is absorbing boundary condition.

take much longer to run. With ABC boundaries, the CM-5 is three times slower than the Cray. The code for the ABC involves many, many terms. This leads to significant internodal communication. The Cray compiler tends to optimize large numerical expressions automatically, whereas the more primitive Thinking Machine compiler does not do this. If the expression were simplified by hand, the CM codes should run much faster.

6.4 Conclusion

Optimizing code on the massively parallel Connection Machine takes much more tweaking and requires familiarity with the machine architecture. We have reduced the speed of the time stepping or propagation such that the CM-5 runs about 40 times faster than the single processor Cray. But the entire program can be 3 to 0.33 times

faster on the CM than on the Cray, depending on the boundary condition. Parallel machines can handle large problems requiring much memory.

Chapter 7

Boundary conditions

Summary:

In some cases, Perfectly Matched Layers (PML) with quartic conductor profiles are superior to the traditional quadratic gradations and are far superior to the widely used Absorbing Boundary Condition (ABC). This PML boundary condition can be applied to gratings; it does not suffer from Fabry-Perot fringes and is not swamped by noise, unlike the Absorbing Boundary Condition.[1]

7.1 Introduction

The vector finite difference time domain (FDTD) is a general, all-purpose method for modeling microwave and optical waves. It can be applied to any electromagnetic device — antennae, receivers, couplers, splitters, gratings, microstrip lines, etc. The standard absorbing boundary condition (ABC) to simulate an open or unbounded region is the Mur second-order ABC.[38]

This absorbing boundary condition is optimized for propagating waves and a limited range of propagation directions. Evanescent waves and waves from other directions may be reflected from the computational border back into the computational domain. These spurious reflections become particularly noticeable when the index

[1]Most of this chapter has been published in *Microwave and Optical Technology Letters*.[55]

of refraction changes along the border or when a waveguide crosses the border. Unfortunately, this affects such important structures as microstrip lines at microwave frequencies and dielectric waveguides at optical frequencies. Many researchers[168-170] have devised schemes to combat these reflections.

Recently, Berenger formulated the perfectly matched layer (PML)[49] to model open boundary conditions. This has since been extended to three spatial dimensions[56] and to dielectric waveguides.[57,171] The PML method uses an artificial conductor that absorbs incident fields. These fields are split into two components, of which only one "sees" the conductor. To minimize back reflections, Berenger[49] and Pekel and Mittra[172] suggest that increasing the conductivity quadratically (with a power of $n = 2$) is preferable to uniform and linear profiles. As a result, quadratic gradations are the norm.[59,58,173]

In this letter, two new results are presented. First, for a waveguide problem, quartic ($n = 4$) conductivity profiles are shown to be better than quadratic ones. In this GaAs waveguide, the reflections from a quartic PML ($n = 4$) are two orders of magnitude lower than those from a quadratic ($n = 2$) PML, which are, in turn, two orders lower than those from the Mur second-order ABC. Incidentally, this work was done independently of Taflove's group;[54] quartic PMLs have been applied to air bridge filters.[71] Secondly, this letter is the first to compare a quartic PML and a Mur second-order ABC in periodic structures. For this, high "Q", quarter wave shifted gratings were studied — devices that are particularly hard to model. Long runs with a Mur second-order ABC proved to be unstable. Spurious reflections from a Mur second-order ABC also produced Fabry-Perot oscillations. In contrast, the PML did not suffer from these problems.

7.2 Perfectly Matched Layers

In this section, the superiority of quartic PML for waveguides is demonstrated. Using Berenger's notation,[49] the conductivity σ can be expressed as

$$\sigma(\rho) = \sigma_{\max}\left(\frac{\rho}{\delta}\right)^n,$$

where δ is the PML thickness, $\sigma_{\max}$ is the maximum conductivity or the conductivity at the edge, and n is order of the polynomial which describes the conductivity profile. ρ varies from 0 at the edge of the solution domain to δ next to the perfectly conducting outer boundary. The field is completely reflected at the perfectly conducting outer boundary, where the tangential electric field is zero. As a result, the theoretical reflected field amplitude is

$$R(\theta) = \exp\left(-\frac{2}{n+1}\frac{\sigma_m\delta}{\epsilon_0 c}\cos(\theta)\right),$$

where θ is the angle of incidence, ϵ is the electric permittivity, and c is the speed of light.

To measure the reflectivity of the boundary, a straight, GaAs waveguide is examined. Specifically, the waveguide is 0.29304 μm (or 0.195 wavelengths) wide and has index of $n_{\text{GaAs}} = 3.4$. It is surrounded by air. The source is polarized in z (normal to the waveguide), and temporally has a Gaussian pulse profile, which is modulated at a frequency of $f = 200$ THz or a wavelength of 1.5 μm.

$$\sin(2\pi ft)\exp(-(ft-4)^2),\ t \geq 0. \tag{7.1}$$

Figure 7-1 shows the initial and reflected amplitudes as a function of frequency for a Mur second-order ABC, a PML with $n = 2$, and a PML with $n = 4$. The Mur second-order ABC[37] was implemented in a 2D, scalar FDTD.[69] Both quadratic and quartic PML's were chosen to have a theoretical reflectivity of $R(0) = 10^{-6}$ and a layer thickness of $\delta = 12$ grid points. All of these simulations were performed

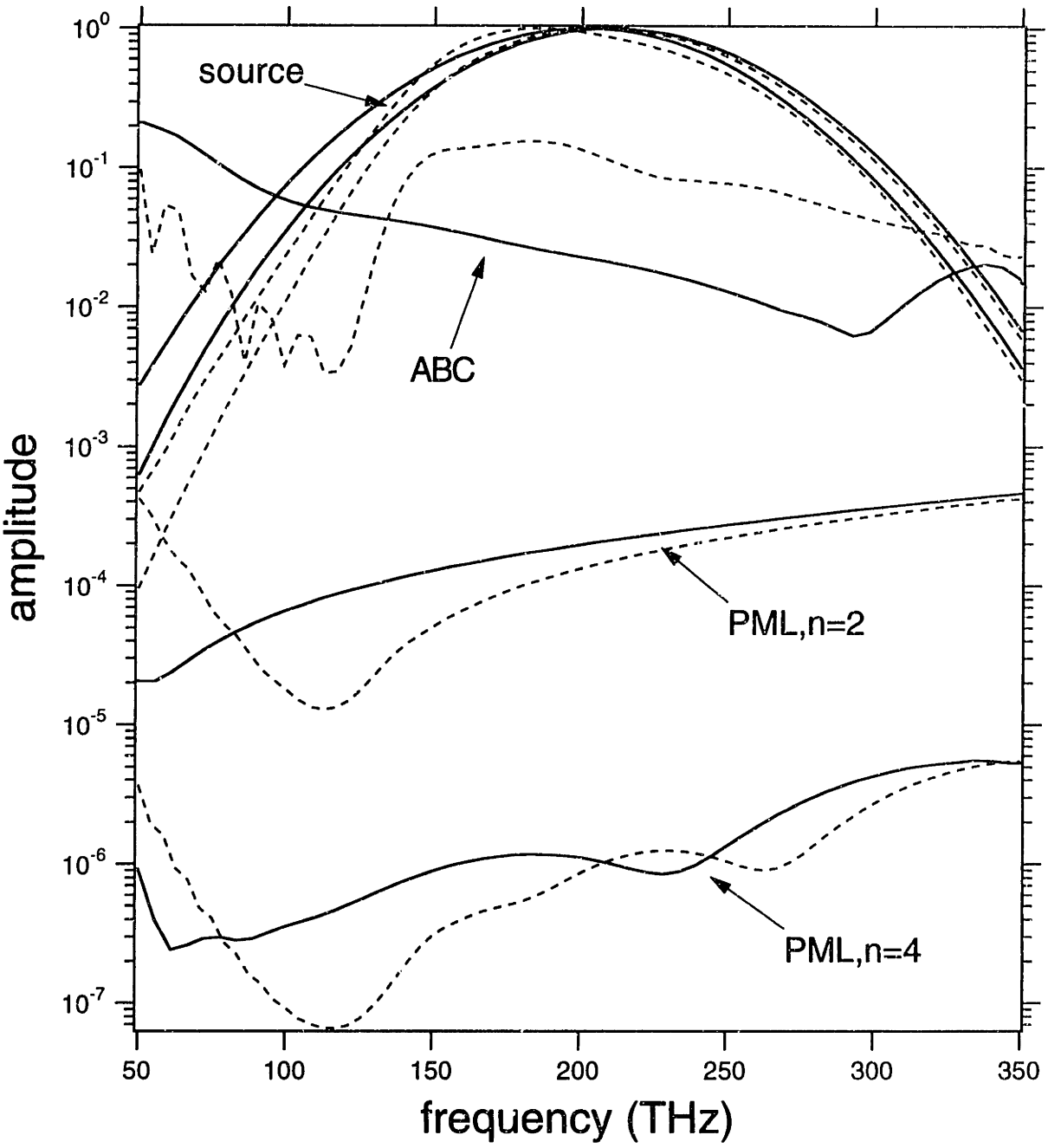

Figure 7-1: In a straight, GaAs waveguide, amplitudes reflected for various frequencies due to a Mur second-order ABC, a quadratic ($n = 2$) PML, and a quartic ($n = 4$) PML. Solid lines denote TE E_Z and dashed lines are for TM H_Z.

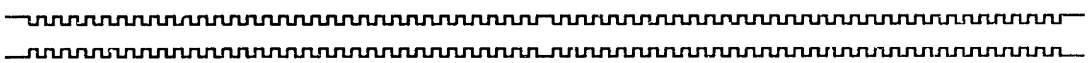

Figure 7-2: Waveguide with quarter wave shifted grating.

for 2D FDTD. The reflected and initial TE electric fields, E_z (where z is normal to waveguide), are plotted with solid lines while the TM magnetic fields, H_z, are denoted with dashed lines. For $R(0) = 10^{-6}$ and $\delta = 12$, the quartic PML produces the least reflections — two orders of magnitude less than the quadratic PML and over four orders of magnitude less than a Mur second-order ABC. Unfortunately, there is a slight polarization dispersion; TE and TM fields differ in their reflections. However, in PML, these reflections are very low over enormous frequency ranges. For example, using layers with only 12 points ($\delta = 12$), reflections from the quartic PML are less than 2×10^{-6} for both TE and TM waves, from 0 to 250 THz.

7.3 Grating example

PML's low reflections over a large bandwidth are particularly advantageous for modeling high "Q", quarter wave shifted gratings. Such gratings can store energy for long times and have sharp transmission resonances. To model these effects, very long simulations, involving tens of or even hundreds of thousands of time steps, are required.

The grating example comes from periodically notching the sides of the beforementioned, straight waveguide. The notches are 0.0356 free-space wavelengths deep and 0.0888 wavelengths long. Notches are separated from each other by 0.178 wavelengths. There are 33 notch pairs on each side of the unnotched center section, which measures 0.178 wavelengths long. Overall, this quarter-wave shifted distributed feedback grating (figure 7-2) is 0.195 wavelengths wide and 11.812 wavelengths long.

Figure 7-3 plots the reflected and transmitted powers for this grating. This simulation uses a Mur second-order ABC and 2^{18} time steps. Note that 112.60 time

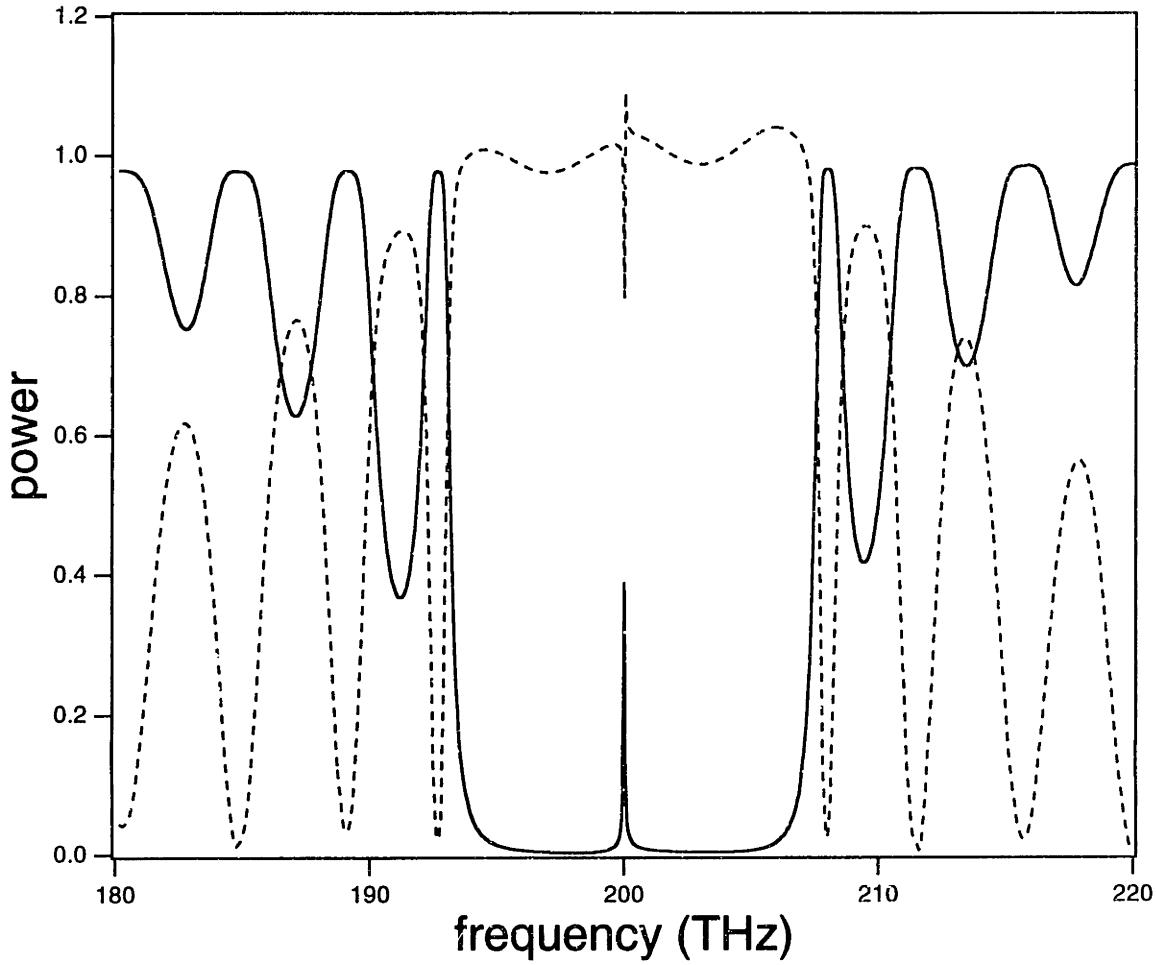

Figure 7-3: Reflected (dashed line) and transmitted (solid line) powers for grating as a function of frequency, from a Mur second-order ABC simulation with 2^{18} time steps.

steps constitute an optical cycle at 200 THz. Between 193 and 207 THz, the reflection coefficient should be constant, but instead it is observed to oscillate about unity. These Fabry-Perot oscillations are an artifact of the computation; they result from a "cavity" that is generated by reflections from the computational border near the source and from the notches closest to the source. At 200 THz, the transmission peak is just starting to emerge. In order to fully resolve the sharp transmission resonance near 200 THz, the simulation must be executed longer.

Yet, if this same simulation were executed twice as long (2^{19} time steps), "garbage" is obtained. Figure 7-4 presents the resulting reflection and transmission spectra. These spectra suffer greatly from instabilities, noise and oscillations. During the

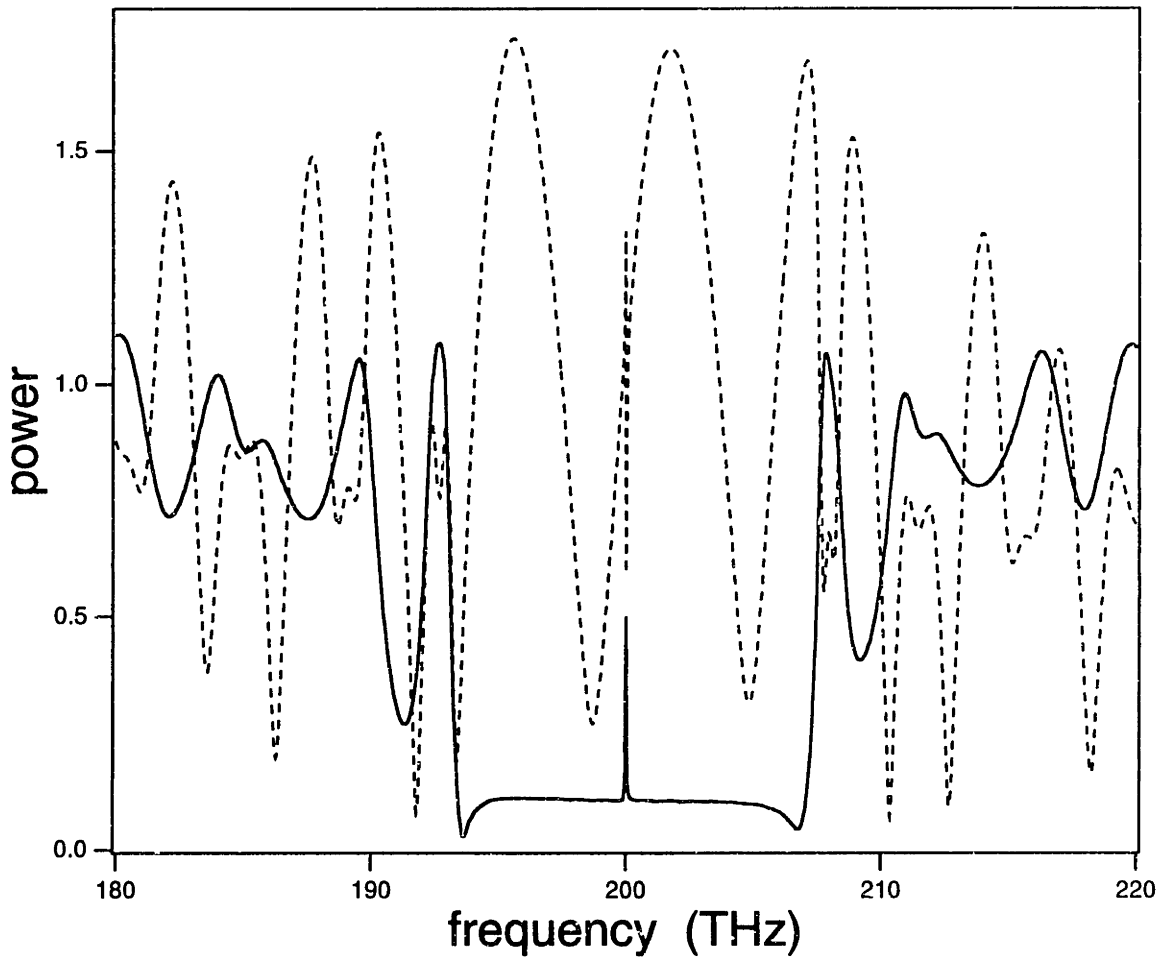

Figure 7-4: Reflected (dashed line) and transmitted (solid line) powers for grating as a function of frequency, from a Mur second-order ABC simulation with 2^{19} time steps.

long simulation, the spurious reflections from the border build up, couple into the resonator, and produce these artifacts.

In contrast, PML simulations do not suffer from these instabilities or oscillations. Figure 7-5 shows the spectra from an even longer run, with 2^{21} or over two million time steps! Notice the reflection coefficient is very flat between 193 and 207 THz; the borders do not reflect nor set up Fabry-Perot cavities. Also there is little noise; the spectra are clearly discernible. The transmission resonance is adequately resolved, with 8.0 GHz resolution.

7.4 Conclusion

Here, quartic gradations in the PML conductor are shown, for the cases examined, to be better than quadratic ones. For gratings, the Mur second-order ABC can lead to Fabry-Perot oscillations and to spurious noise. But PML can give accurate transmission and reflection spectra with high frequency resolution.

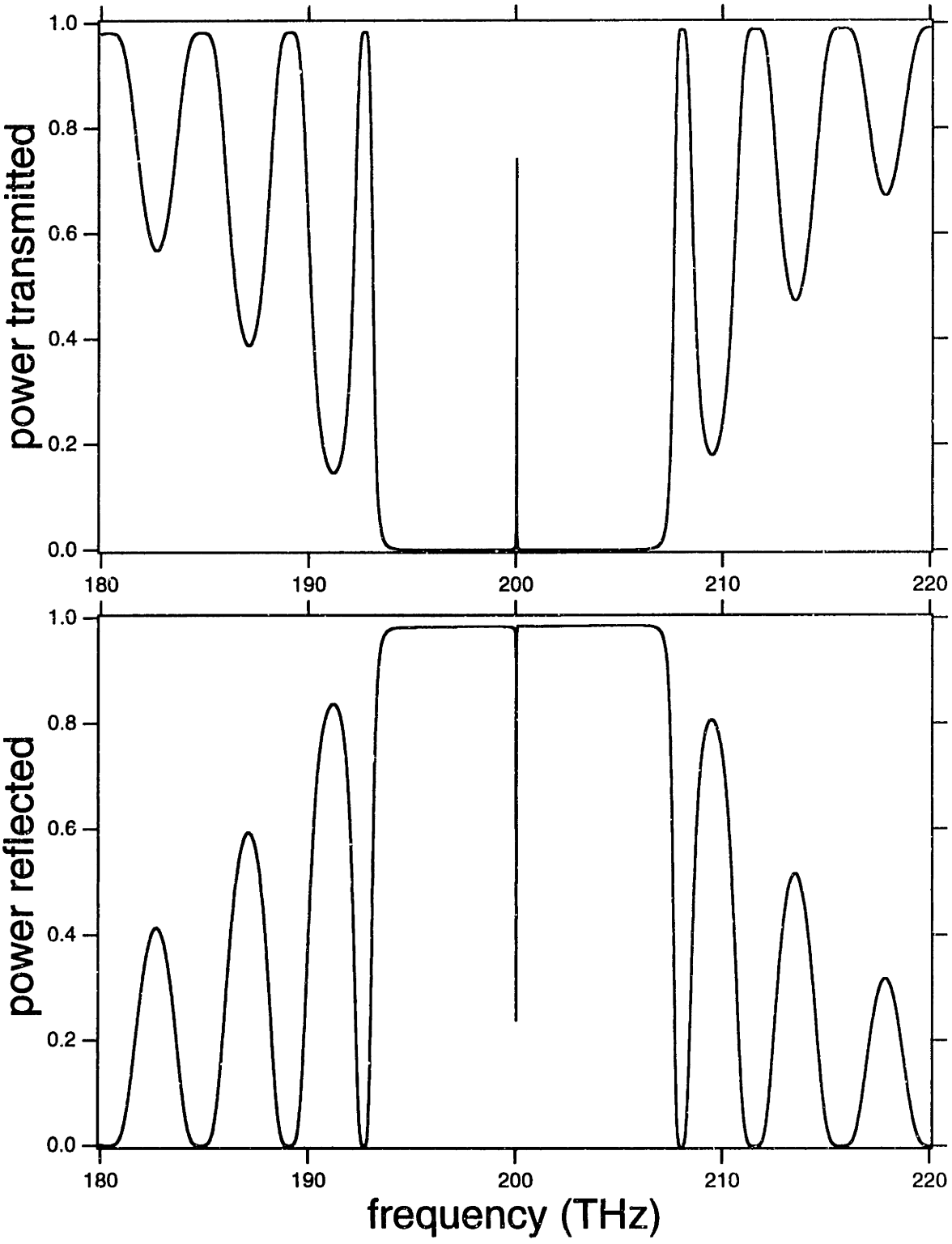

Figure 7-5: Reflected and transmitted powers for grating as a function of frequency, from a quartic ($n = 4$) PML simulation with 2^{21} time steps.

Chapter 8

Air bridge filter

Summary:

Surrounding waveguides by air reduces radiation losses so the air bridge geometry can produce optical filters with sharp transmission resonances and very wide stop bands. Simulations from a vector finite difference time domain code are presented.[1]

8.1 Introduction

In recent years, photonic band gap materials have attracted much attention. What makes such materials special are wide band gaps or stop bands — ranges of frequencies where no light can propagate. Frequencies in the band gap will be reflected by photonic band gap materials and be attenuated within these materials. Possible applications of these two unique properties are laser cavities with low thresholds, efficient radiation from planar antennae, and microbends with low loss.[74, 117, 119, 130, 161]

Here we give a quantitative description of the filter properties of these structures. For simplicity we study a one dimensional band gap. Conventional gratings may have index modulations of only a few percent. In contrast, photonic band gap materials have large index contrasts typically, as large as of 3 to 1. This large index ratio or contrast leads to a wide stop band. But as the index contrasts or grating strengths

[1] Portions of this chapter can be found in an award write-up,[71] a book chapter,[174] and a journal article.[72]

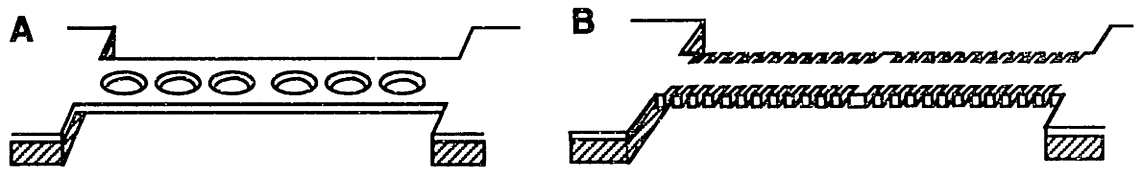

Figure 8-1:
A. Schematic of air-bridge with six circular holes
B. Another bridge with 33 notches.

become larger, the fields tend to radiate out of the waveguide. To confine the light, we can surround the waveguide by a lower index material or by a photonic band gap material. In the present case, we use air, forming an air bridge (figure 8-1). Since interfaces between air and high dielectric material confine light well, we are able to design an optical filter (figure 8-1) whose transmission resonance peaks at 91%. And since the index contrasts are so large, the stop band width is about 40% of the carrier frequency! We also present a second filter with a very sharp transmission resonance, whose quality factor "Q" exceeds 24,000. In this chapter, we will first describe how we model these filters, then present more details on the characteristics of these novel filters.

8.2 Vector approach

We calculate the transmission, reflection and radiation spectrum, using a vector finite difference-time domain program. Such programs are reviewed in chapter 1 and described in more detail in chapter 7. Since the index contrasts are so large, analytic methods like coupled mode theory are not as accurate. We need to turn to numerical techniques. Specifically, we integrate Maxwell's equations forward in time over the two spatial dimensions.

$$\nabla \times \vec{E} = \mu \frac{\partial \vec{H}}{\partial t}$$

$$\nabla \times \vec{H} = \epsilon \frac{\partial \vec{E}}{\partial t}$$

For accuracy, the electric E and magnetic H fields are separated by half steps in space and time, in a Yee lattice.[34] This initial value problem is explicit; the fields at one time step depend only on the fields at the previous time step. As a result, such schemes can be run efficiently on parallel computers.[35]

In such programs, the boundary conditions tend to be the most challenging part. The treatment of the outer boundary (unbounded space) is of particular importance. The popular Absorbing Boundary Condition[37] suffers from reflections from the computational border. These spurious reflections become particularly severe in microstrip line simulations, where the indices of refraction changes along the border. Over the years, many schemes have been devised to minimize these reflections.[168-170] The recently reported Berenger's Perfectly Matched Layer (PML)[49] gives low reflections, even for microstrip lines.[57] To achieve such low reflections, researchers[49,57] increase the conductivity or absorption strength or the matching layers quadratically, with a power of $n = 2$. However, Chen and Li[55] find that significant further improvement can be achieved by using quartic gradations ($n = 4$). Following this example, we choose our layer to be $\delta = 12$ grid points thick, which has a theoretical reflectivity of $R(\theta = 0) = 10^{-6}$ in free space. Inside the dielectric, the conductivity is multiplied by the dielectric constant.[57] These low reflections eliminate the Fabry-Perot fringes that would otherwise arise from the reflections at the grating region and the computational boundary.[55]

One can use a sine wave source to calculate the transmission and reflection at one frequency.[69] However, pulsed sources are more efficient for calculations over a range of frequencies. In particular, one can send in a gaussian source to the filter and monitor the reflected and transmitted pulses. The Fast Fourier Transform (FFT) of these pulses, normalized to the spectrum of the input pulse, gives the reflection and transmission spectrum. In our simulations, we send in a gaussian pulse whose pulse

width equals the period $1/f$.

$$\sin(2\pi ft)\exp\left[-(ft-4)^2\right],\ t \geq 0$$

This gives sufficient frequency range to model the filters.

We can also obtain physical insight about the transmission peak, by examining the resonator properties. The energy of a resonator decays exponentially.

$$W = W_0 e^{-\omega_0 t/Q} = W_0 e^{-2t/\tau}$$

where $Q = \omega_0\tau/2$ is the quality factor, ω_0 is the resonance frequency, and τ is the amplitude's decay constant. Using coupled mode theory, Haus[162] computes the transmitted power through a resonator

$$T_{pwr} = \frac{(4\tau^2/\tau_{e1}\tau_{e2}}{(\omega-\omega_0)^2\tau^2+1}$$

where τ_{e1} measures the decay of fields into the external world or waveguide from port 1. Since our filters have symmetric input and output ports, τ_{e1} and τ_{e2} are equal and can be combined into an overall external decay constant $\tau_e = \tau_{e1}/2$. This simplifies the transmission to

$$T_{pwr} = \frac{(\tau^2/\tau_e)^2}{(\omega-\omega_0)^2\tau^2+1}.$$

This transmission expression considers the input coupling between the waveguide and the resonator, the intrinsic radiation losses of the resonator and the output coupling of power to the waveguide. The maximum transmission is $T_{pwr}(\omega=\omega_0) = (\tau^2/\tau_e)^2 = (Q^2/Q_e)^2$, where Q_e is the external quality factor. The ratio of the resonance frequency and the full width half maximum (FWHM) of this transmission resonance is

$$Q_{FWHM} = \frac{\omega_0}{2/\tau} = \frac{\omega_0\tau}{2} = Q_{resonator}.$$

This suggests that from the transmission peak, one can predict such resonator parameters as ω_0, Q and Q_e.

We calculate such parameters using the finite difference time domain method. To extract the quality factors, we need to find the field profile of that resonator eigenmode. An arbitrary initial field can be decomposed into many eigenmodes, each of which decays exponentially with a rate ω/Q. A sufficiently long propagation will yield the mode with the largest Q; the other eigenmodes will be negligibly small.[73] Of course, this calculation can be speeded up if the initial field resembles the high Q eigenmodes. By monitoring the rate of energy decay, we obtain the Q of the eigenmode. The resonance frequency ω_0 comes from the oscillation rate of the electric or magnetic field.

So, by knowing the resonator properties, we can predict some features of the transmission. There is good agreement between the two.

8.3 Two designs

The optical filters we wish to investigate are air bridges (figure 8-1). The air surrounding the waveguide on all four sides — top, bottom, left and right — helps to confine the light inside the bridge waveguide. This suppresses the radiation losses, giving a high Q resonator and a narrow transmission resonance peak. To illustrate this point, let us examine what happens if the air were replaced by another material on just one side. We will perform a 2D model of an air bridge, by focusing only on its cross section. The air bridge shown in figure 8-1a has six air holes, which are spaced 0.232 free-space wavelengths λ or (for $\lambda = 1.55\mu$m) 0.360 μm apart. This hole-to-hole separation increases to 0.325 λ or 0.503 μm for the center two holes, giving rise to the quarter wave-like phase shift that gives the transmission resonance. The diameter of each hole is 0.167 λ or 0.258 μm. The entire structure is only 1.420 λ or 2.20 μm. This small size allows for a compact integration of many wavelength filters on a small chip. A slightly longer version of this structure — one with more air holes — can act as a high Q microcavity.[69,73,108] This waveguide has a width of 0.151 λ or 0.234 μm and an index of $n = 3.4$. The precise value of the index is not important. We choose 3.4 because it is close to the indices for GaAs and Si. Now, if we place AlAs ($n = 2.85$)

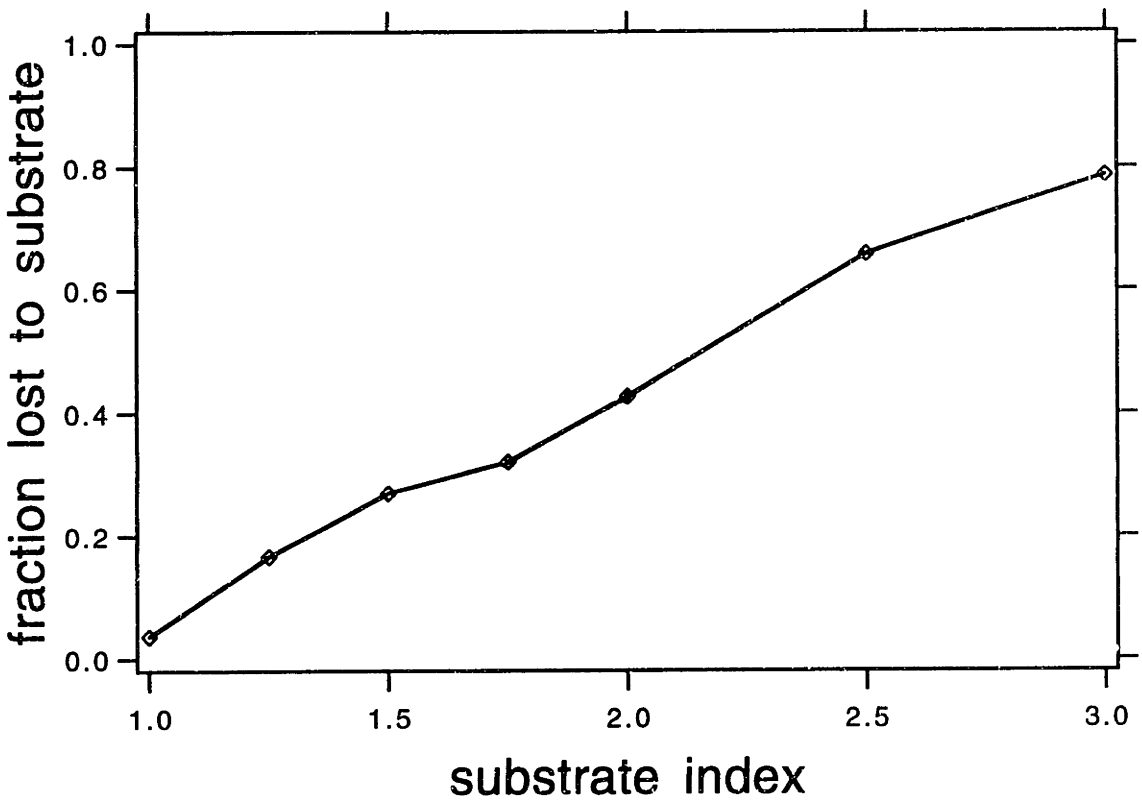

Figure 8-2: Fractional power lost to substrate as a function of substrate index.

next to the waveguide, about 80% is radiated into the AlAs slab. So, even an index contrast of 3.4 to 2.8 is not enough to confine the light (figure 8-2). The radiation loss drops dramatically as the index becomes lower. For air ($n = 1$) the loss to that one side becomes almost negligible. These radiative losses are also evident for posts of silicon nitrate ($n_{eff} = 1.8821$) over silicon oxide ($n_{eff} = 1.3586$). Figure 5-2 in chapter 5 shows the scattered radiation interfering with the incident light. Chapter5 and our publication[69] contains more details on how these calculations are performed.

Figure 8-3 plots the transmitted and reflected power as a function of wavelength. Notice the reflection is almost unity over a 600 nm range. This is about 40% of the carrier wavelength! The Q or ratio of the carrier wavelength to the transmission FWHM is 264.7. The radiation loss is near 0, over most of the range. At lower wavelengths, however, radiation increases as light is coupled to higher order transverse modes. Figure 8-4 shows the electric field (pointing down) and the magnetic field (pointing out of page) at transmission resonance. Coming in from the left side of the

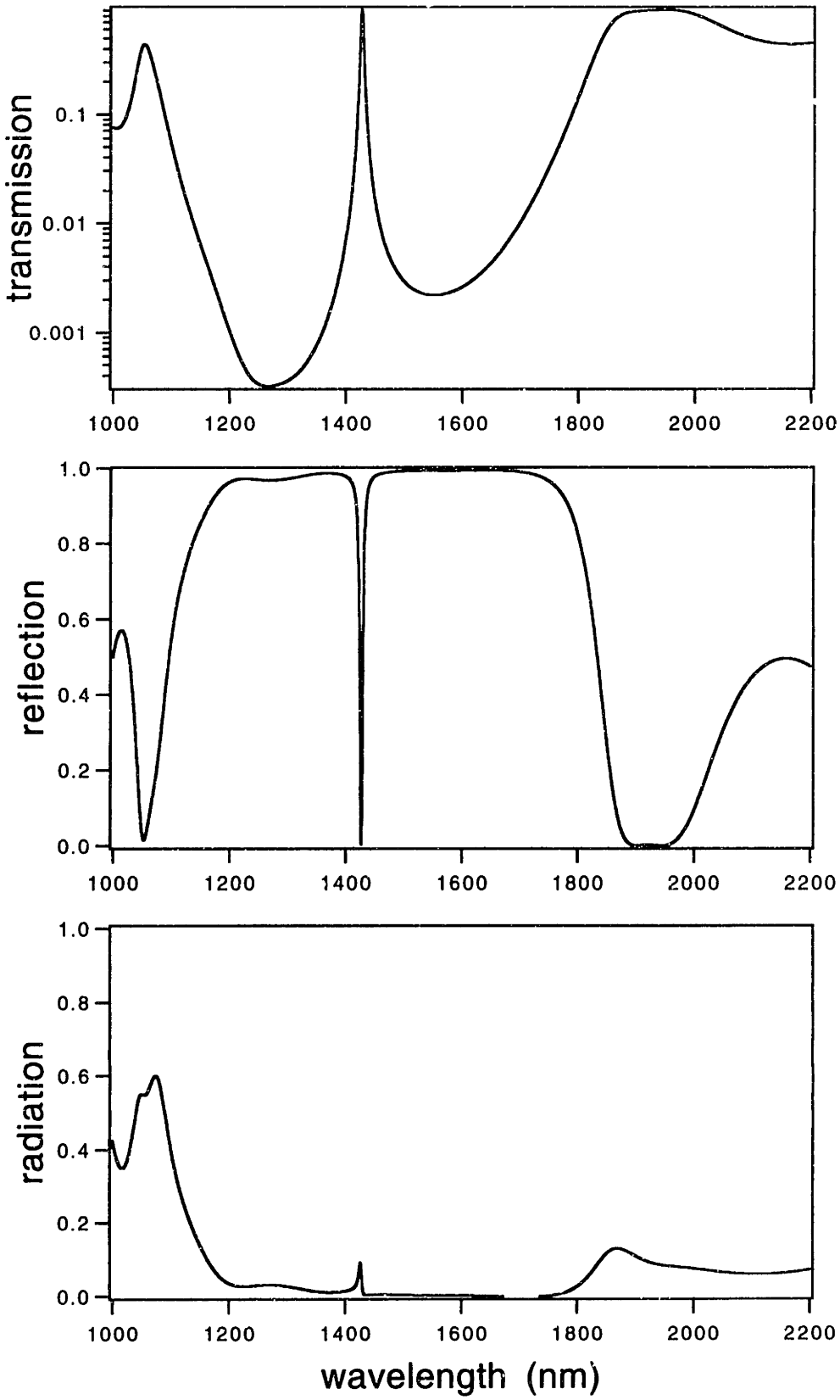

Figure 8-3: Power transmitted, reflected and radiated as a function of wavelength in bridge with three pairs of air holes.

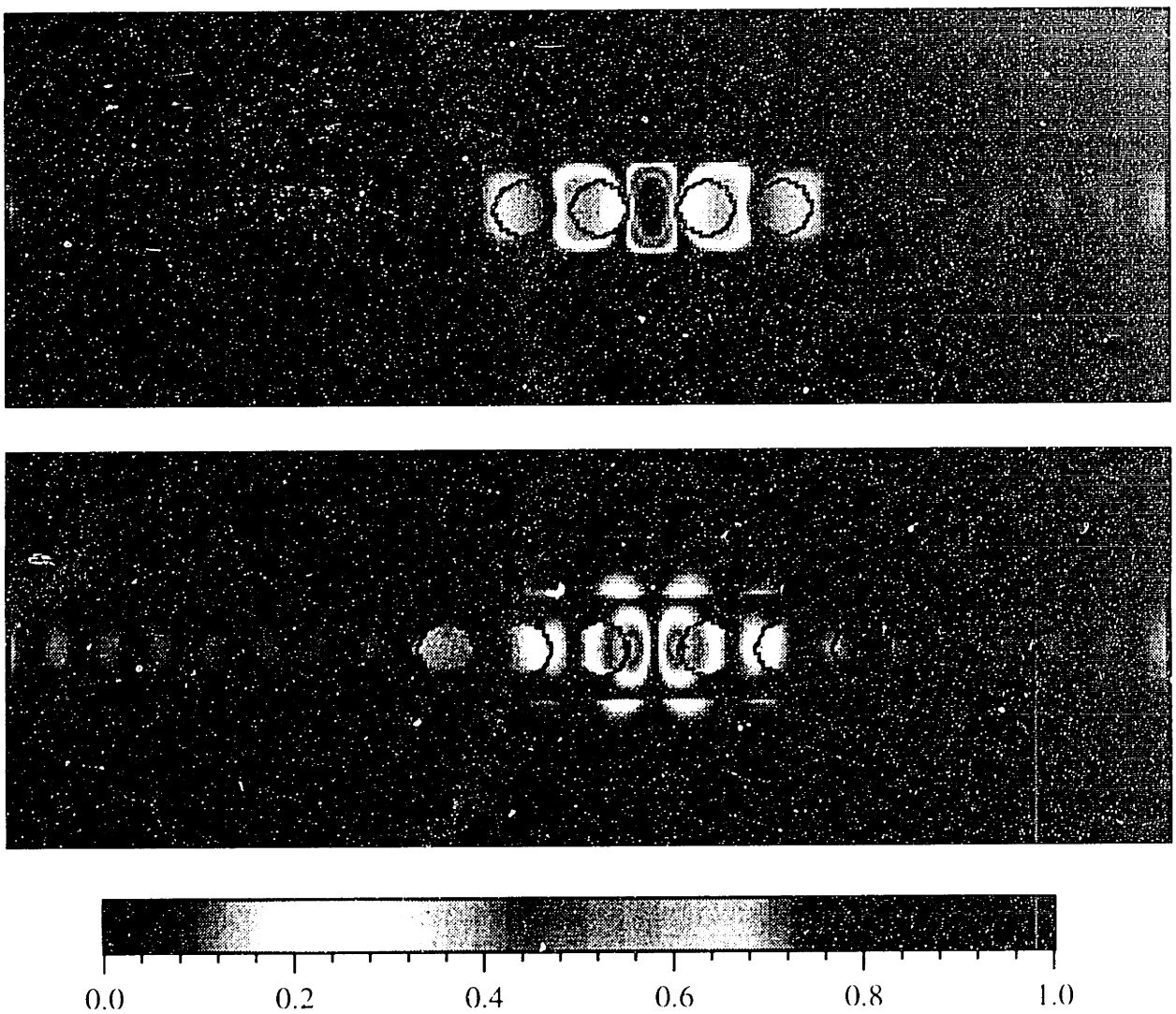

Figure 8-4: air bridge with 6 circular holes
Top panel: Electric field component lying in the page and transverse to the propagation direction, at transmission resonance.
Bottom panel: Magnetic field normal to the page, at transmission resonance.

figure, light is coupled to the resonator mode in which most of the light is localized about the so-called quarter wave phase shift or dielectric defect. Then over 91% is transmitted to the other side! This air bridge geometry allows a wide stopband and a large transmission. And most of the light is confined to the waveguide.

By measuring the energy decay of the resonator, we find the quality factor of 269.6. This compares favorably to the $Q = 264.7$ obtained from the transmission width. Since at resonance, the maximum transmitted power is $T_{pwr} = .91174$ and $T_{pwr} = (Q/Q_t)^2$, then $Q_t = 1.0473\,Q = 282.3$. The estimated radiation quality factor

is $Q_r = 1/(1/269.6 - 1/282.3) = 5993$, using

$$1/Q = 1/Q_r + 1/Q_e.$$

If one more air hole were added to each end of the air bridge, the quality factor increases because the external quality factor increases. The radiation quality factor Q_r should stay roughly the same. But because Q_e increases, the maximum transmitted power decreases to 0.43 (figure 8-5). From the FWHM of the transmission resonance, we obtain a total quality factor $Q = 918$. By knowing the maximum T_{pwr}, we can separate the quality factor into $Q_e = 1400.$ and $Q_r = 2667$. This Q_r is more accurate than the one derived from three hole pair case, which comes from the difference of similarly sized numbers. K.-Y. Lim, G. S. Petrich, and L. A. Kolodziejski have made impressive progress[129, 108] towards fabricating Si/SiO_2 and GaAs/AlGaAs versions of this air bridge. Figure 8-6 shows their recent GaAs air bridge. With a minimum feature size of 0.4μm, it has a transmission resonance around $\lambda = 4.2\mu$m.

We present another filter with an even larger "Q". By omitting the holes and by notching the sides of the air-bridge instead (figure 8-1b), we reduce the index contrasts or grating strengths. This reduces the stop band width. More importantly, this also lowers the radiation losses. Specifically, the stop band width falls to 70 nm. Note that for optical communication purposes, this width is more than adequate, being about double the gain bandwidth of erbium amplifiers. The quality factor increases significantly; it exceeds Q=20,000. The notches are 0.0356 free-space wavelengths deep and 0.0888 wavelengths long. Notches are separated from each other by 0.178 wavelengths. As before, we choose an index of 3.4 for the bridge. It is 0.195 wavelengths wide and 11.812 wavelengths long. There are 33 notch pairs on each side of the phase slip, which measures 0.178 wavelengths long. Figure 8-7 shows the absolute values of the electric field (normal to page) and the magnetic field (in the page but normal to propagation direction). The transmitted, reflected, and radiated powers are shown in figure 8-8. Note the sharpness of the transmission peak at resonance. There are only a few data points in the center of this resonance. Calculating more

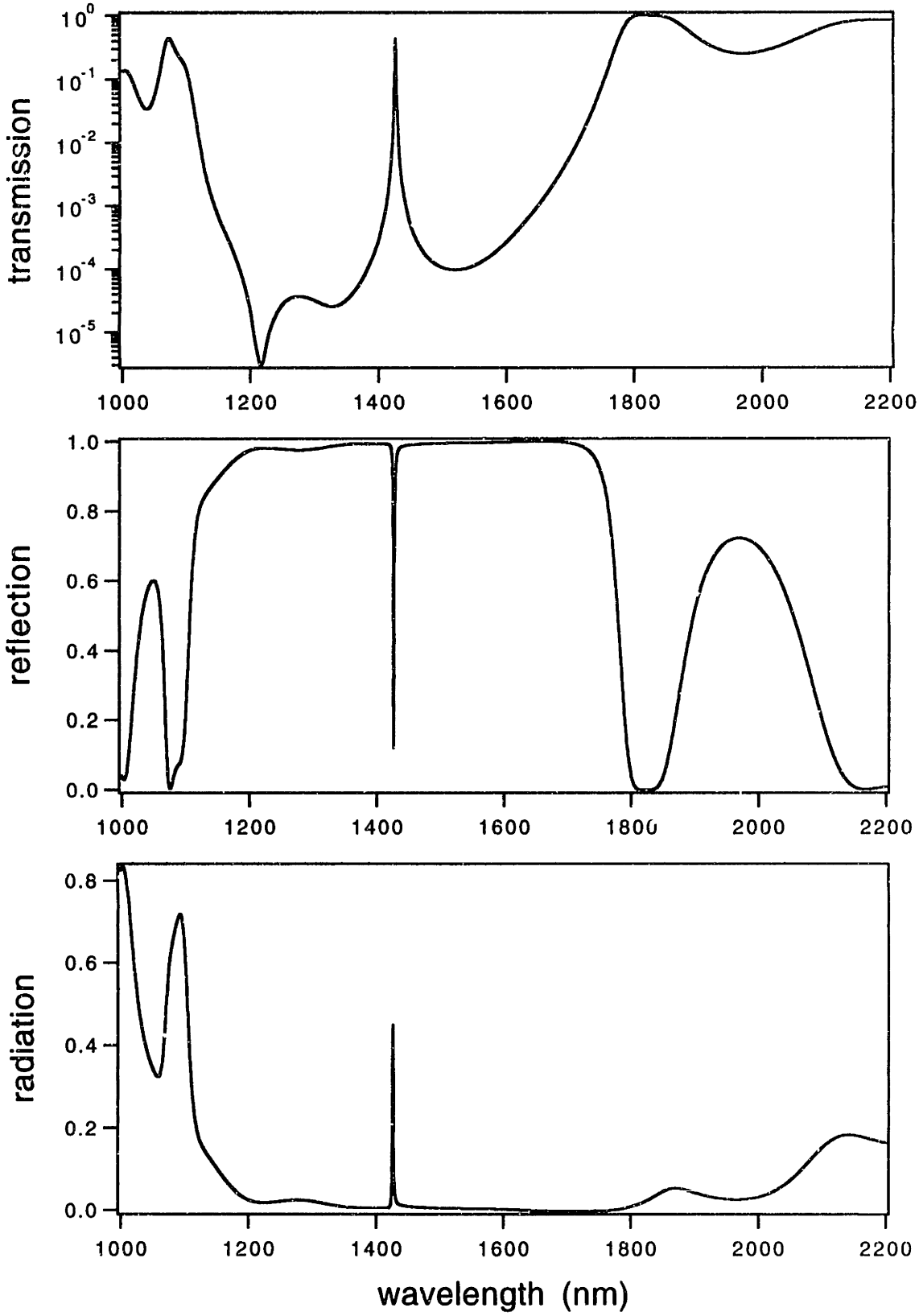

Figure 8-5: Power transmitted, reflected and radiated as a function of wavelength in bridge with four air circle pairs.

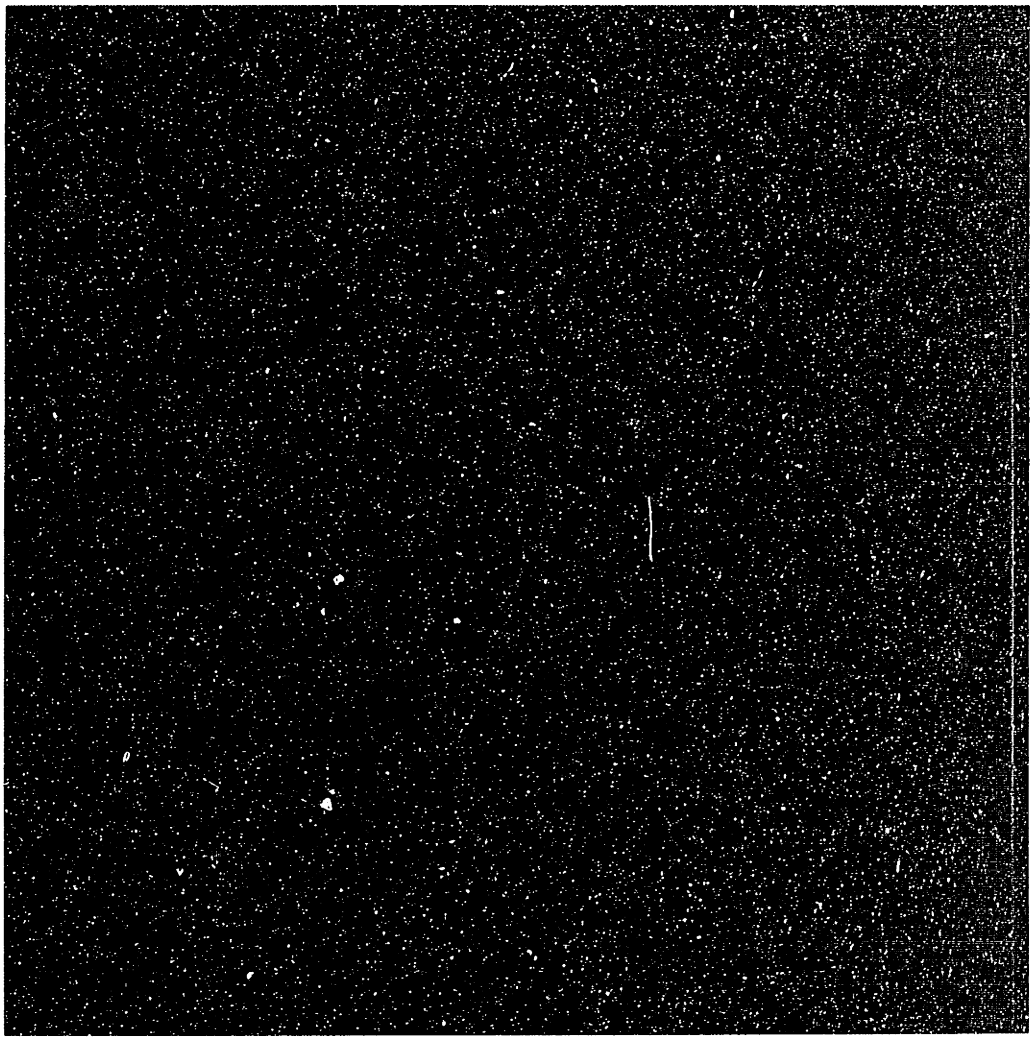

Figure 8-6: Scanning electron microscope (SEM) of GaAs air bridge with four air hole pairs, by K.-Y. Lim and G. S. Petrich.

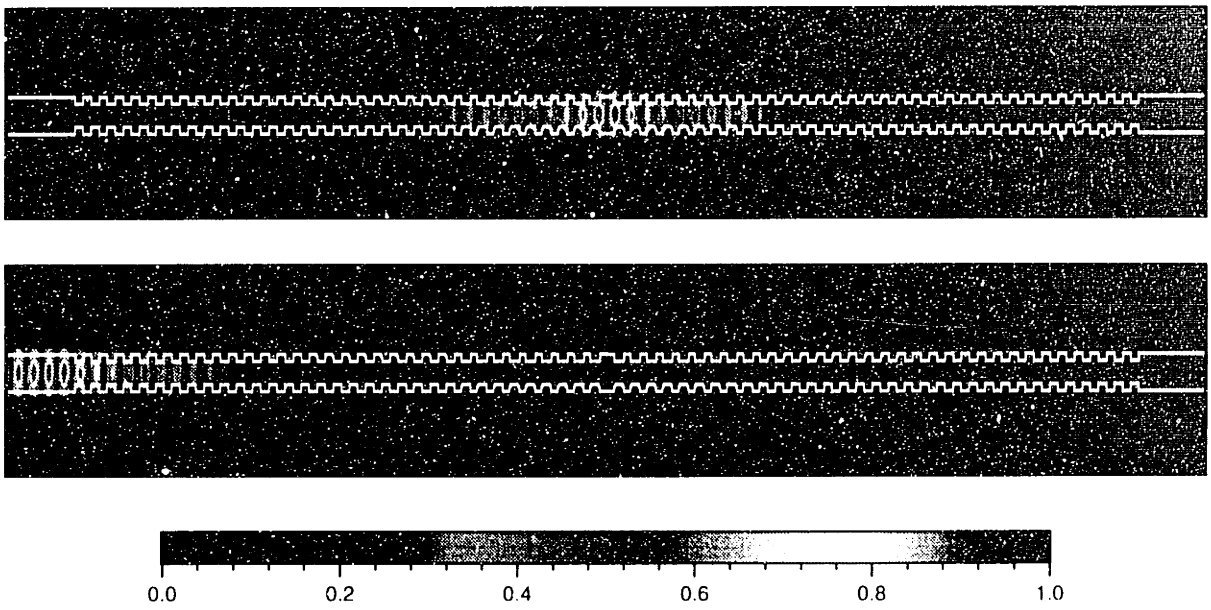

Figure 8-7: air bridge with 66 notch pairs
Top panel: Absolute value of electric field normal to page, at transmission resonance.
Bottom panel: Absolute value of magnetic field lying in the page and transverse to the propagation direction, at transmission resonance.

points would require much computer time. From these points, the quality factor must exceed 11,000. From the energy decay, we find a "Q" of 24,100. The highest transmitted power observed is 0.741. This corresponds to a radiation "Q" of over 173,000! Moving off resonance, the transmission falls by 40 dB. As a result, another filter with a slightly different transmission resonance would see very little crosstalk.

8.4 Three-dimensional analysis

The previous calculations dealt with two dimensional geometries (x and y), they neglected the index changes in the z direction. Prof. Joannopoulos' group has developed two simulation programs that can handle three dimensional objects. Both solve Maxwell's equations — one in frequency domain and the other in the time domain. The air bridge studied in this section (figure 8-1) has been described in the last NATO ASI conference.[174] Specifically, the index is $n = 3.37$. All spatial dimensions

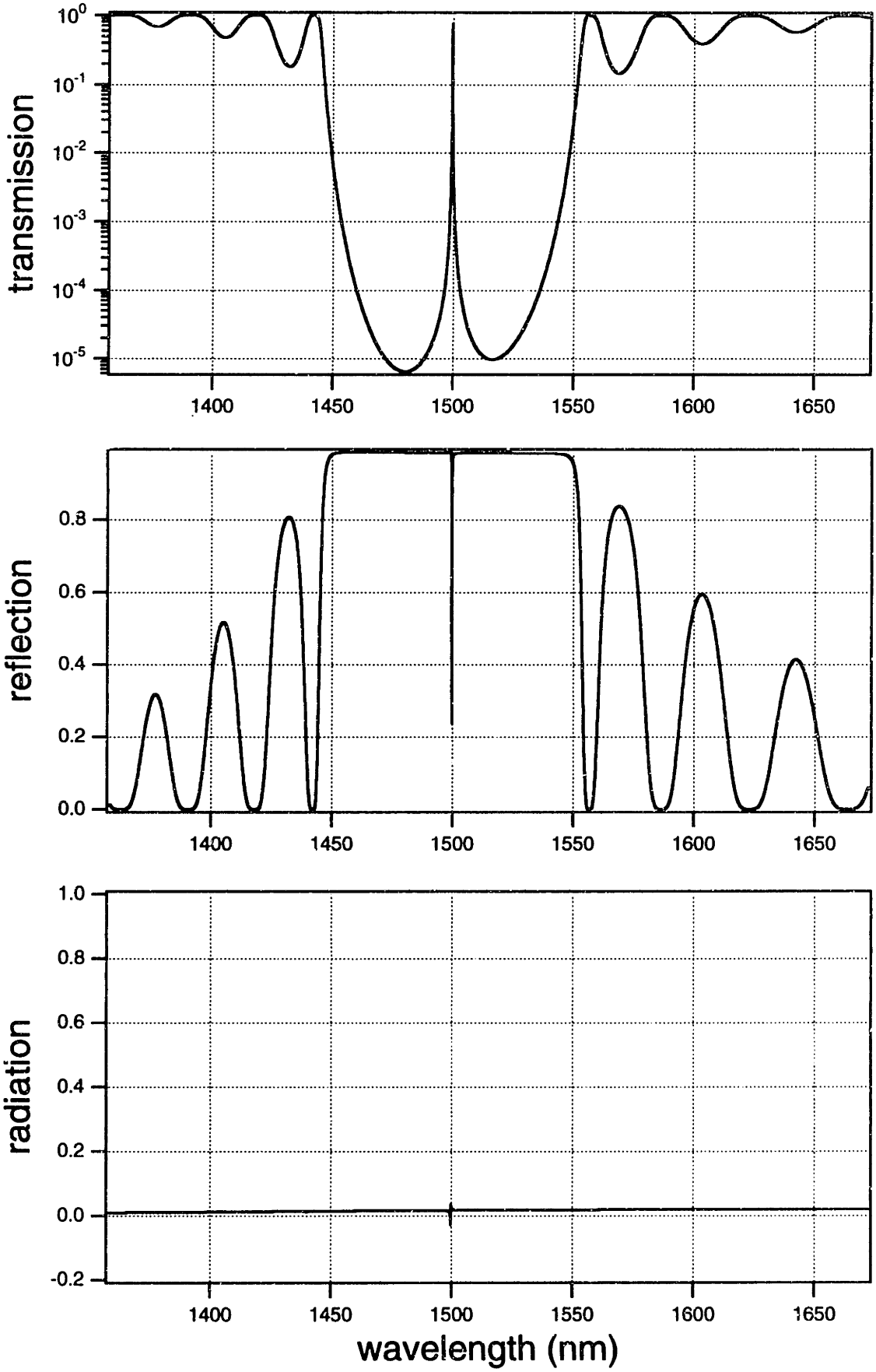

Figure 8-8: Fraction of power transmitted, reflected, and radiated by notched filter as a function of frequency.

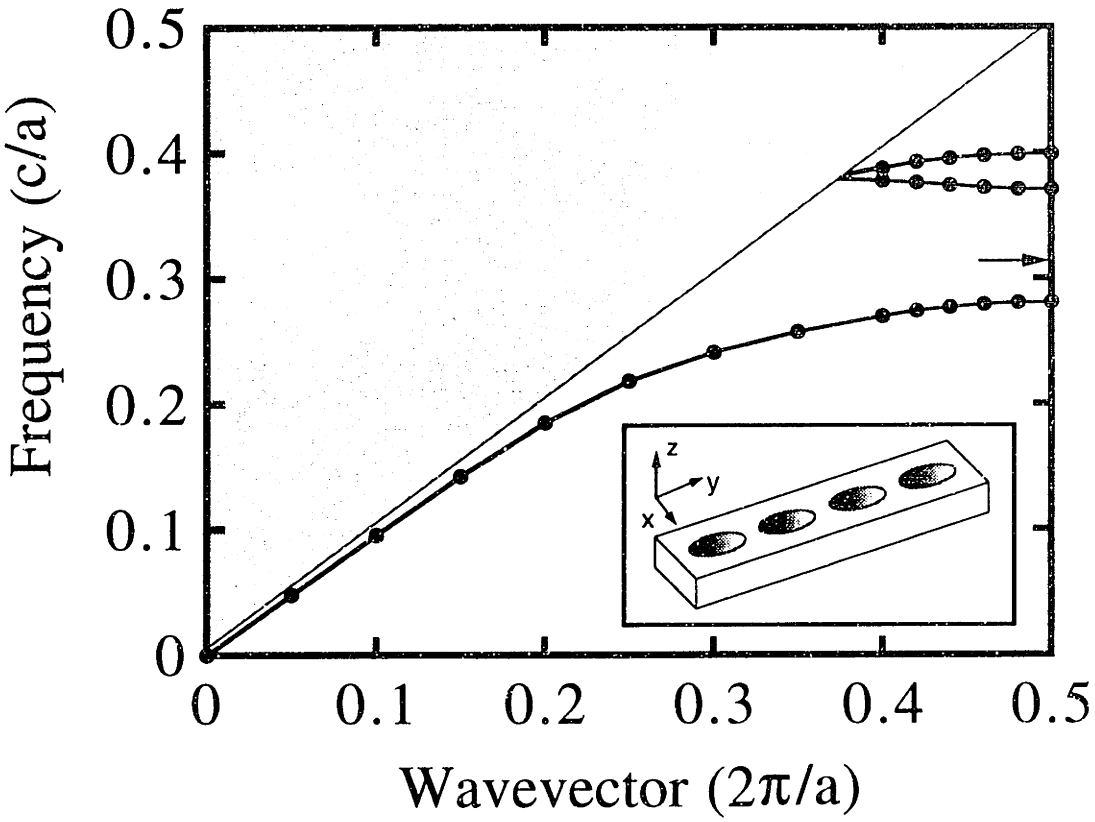

Figure 8-9: Photonic band gap of 3D air bridge. Calculation and figure by Pierre Villeneuve.

are normalized to a — the period (or distance between centers of adjacent holes). The width is $1.2a$; height (or thickness) is $0.4a$; radius of air hole is $0.3a$; distance between two center holes is $1.5a$. I am grateful to Prof. Joannopoulos' group (particularly, to Shanhui and Pierre for their calculations, figures, and friendship).

The frequency domain code solves the vector wave equation, (1.7). Bob Meade and Shanhui Fan have written this code, following the methods of Leung and Liu[78] and Meade *et al.*[79] The band structure is plotted as ω versus k in figure 8-9. I am thankful to Pierre Villeneuve for letting me use his work. Notice that a large bandgap appears between 0.28 and 0.37.

The other program is a three dimensional finite difference time domain (FDTD) code. Shanhui Fan has done an admirable job writing and running this program (see figures 8-10 and 8-11). This code uses the Absorbing Boundary Condition;[38] see chapter 1 for an intuitive description of this algorithm's inner workings and chapter 7 for a comparison with the new PML[49] condition. Since 3D FDTD codes require many

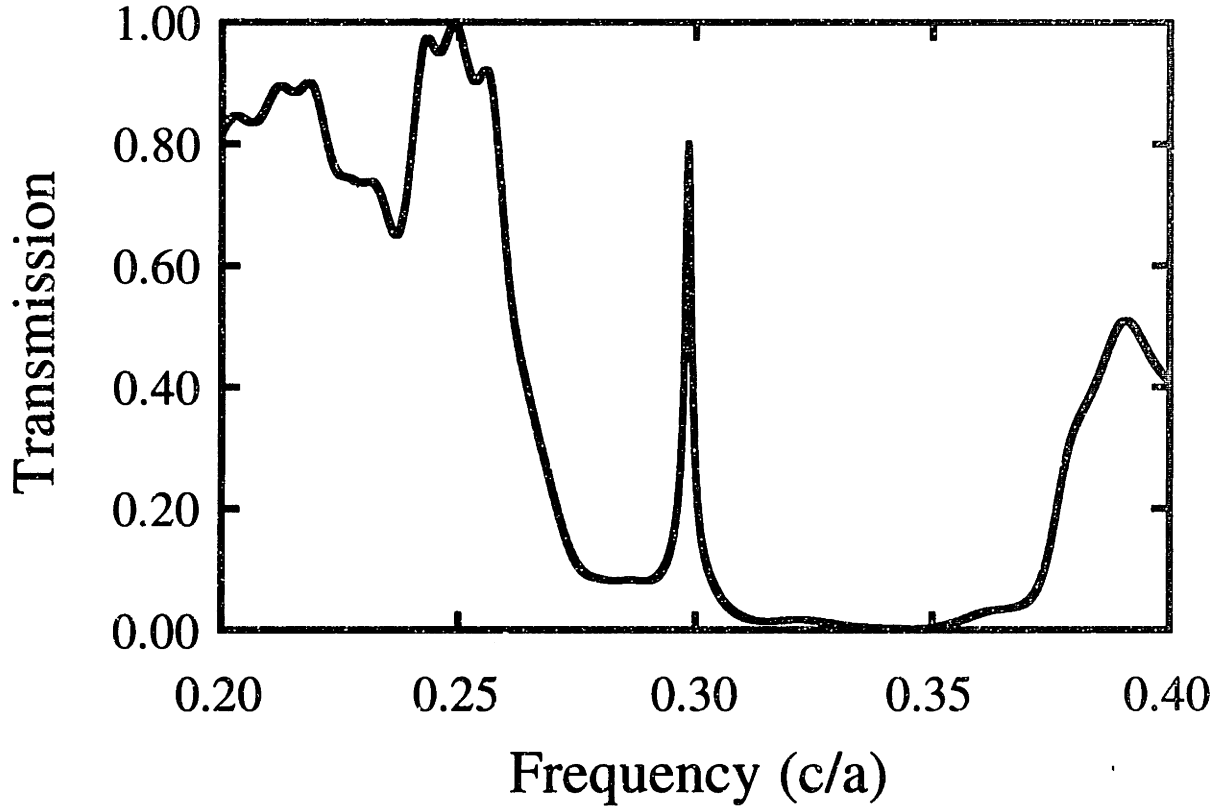

Figure 8-10: Amplitude transmitted through 3D air bridge. Calculation by Shanhui Fan and figure by Pierre Villeneuve.

megawords of memory, it is not always possible to measure the reflection, radiation and transmission, using a large grid with a two point probe (as in chapter 5, in chapter 7, and in the previous section). Instead, one can calculate the transmission only using a very small grid and one probe.[175] One can do a simulation through an air bridge without holes to get the source's transmission, then do a second simulation through the air bridge with the holes. The ratio of the two transmissions gives the the transmission due to the holes. Figure 8-10 shows the amplitude transmitted, using this method. The wiggles, when the frequency is between 0.20 and 0.25, are computer artifacts; they result from the Fabry Perot oscillations, described in chapter 7. The quality factor is 271 — exhibiting a good agreement with the two dimensional calculations. But the resonant transmission peaks at 80%. In contrast, the FDTD 2D code gives a maximum transmission of 95.5%.

Since the maximum transmission is $(Q^2/Q_e)^2$, this implies a discrepancy in Q_e, which in turn implies a difference in Q_r, because $Q_r = 1/(1/Q - 1/Q_e)$. As more holes

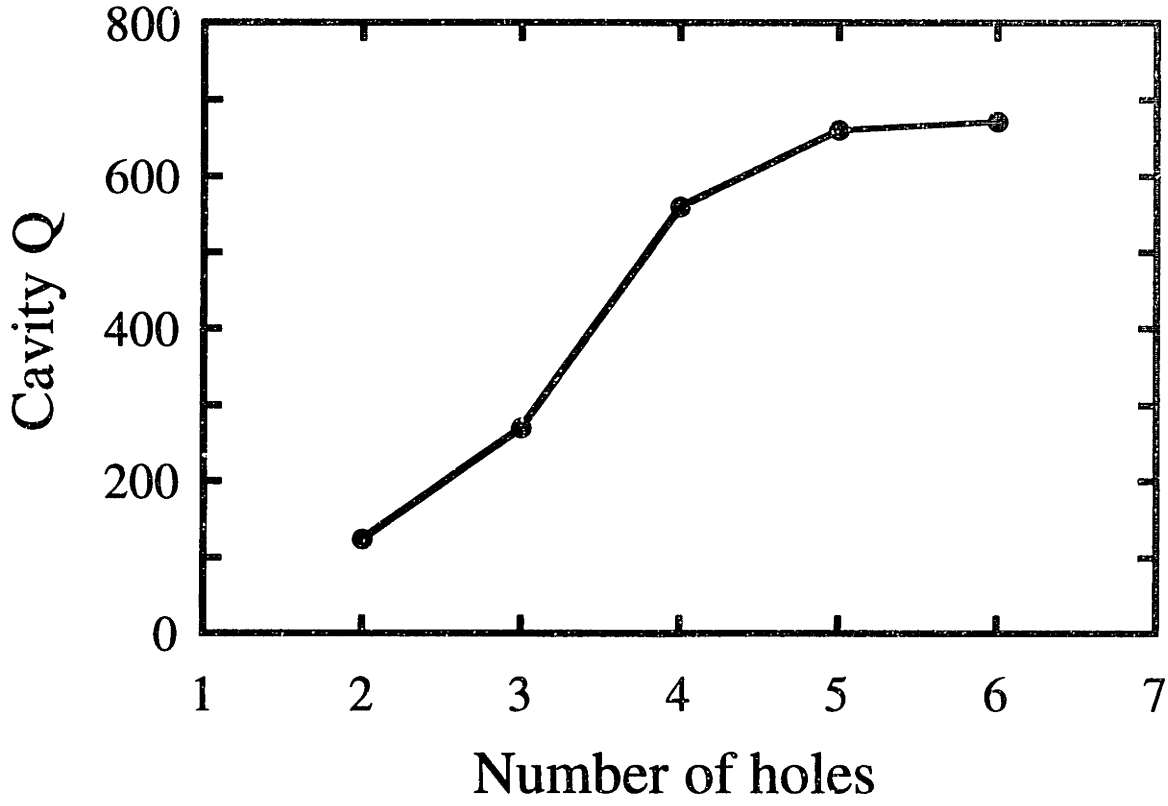

Figure 8-11: Quality factor increases with number of hole pairs. Calculation by Shanhui Fan and figure by Pierre Villeneuve.

are added, the external quality factor Q_e increases exponentially. So, with a large number of holes, the quality factor is dominated by Q_r. Figure 8-11 plots the effect of more holes on Q. It seems that Q saturates at 700; in another words, $Q_r = 700$. But the 2D bridge with 7 hole pairs in chapter 5 implies a radiation Q exceeding 4000. Light must be diffracting or escaping into the z direction.

As developed by Prof. Joannopoulos' group, these three dimensional codes can calculate the band structure, the transmission, and the quality factor. The quality factor of the resonator and the sharpness of the transmission seems to agree with two dimensional calculations.

8.5 Conclusion

We have presented optical filters based on air bridge geometries. The suppression of radiation leads a large transmissions. The large index modulations give enormous

stop bands whose widths are about 40% of the carrier wavelength. We can also achieve "Q"s of over 24,000, resulting in very sharp transmission resonances. A three dimensional analysis of the air bridge is also presented.

Chapter 9

Conclusion

This thesis numerically models integrated optic devices. The extension of the beam propagation techniques allows for the more efficient calculation of waveguide eigenmodes. Specifically, our study of this method led to the optimization of mode computation and to the calculation of higher order modes. We have also modelled curved waveguides and their bending losses in a more efficient manner. Photonic band gaps form an exciting and rapidly emerging field. Using air bridges, we designed a resonant filter with a very wide band gap and a second filter with a narrow transmission peak. In principle, such devices can be integrated into WDM systems. This thesis also improves the boundary conditions of finite difference time domain codes (FDTD), modifies a scalar-like FDTD technique, and compares a massively parallel supercomputer with an one processor Cray. The improved ability to simulate wave propagation and eigenmode calculation will advance the design and modeling of optical filters, couplers, and other waveguide components.

Appendix A

List of publications

Here I list my publications, both conference proceedings and journal articles. Not all the publication I have worked on during my Ph.D. years are included in this thesis; my time and energy are limited. The included works are asterisked.

Bachelor's thesis

1. Y. Okada, J. Chen, I. H. Campbell, P. M. Fauchet, and S. Wagner, "a-Si and μc-Si grown from SiF_4 with high H_2 dilution in a DC glow discharge," *Materials Research Society Symposium Proceedings*, vol. 149, pp. 93–8, 1989.

2. Y. Okada, J. Chen, I. H. Campbell, P. M. Fauchet, and S. Wagner, "μc-Si growth from SiF_4 with high H_2 dilution in plasma enhanced chemical vapor deposition," *Extended Abstracts of the 1989 Electrochemical Society Fall Meeting*, p. 533, 1989.

3. Y. Okada, J. Chen, I. H. Campbell, P. M. Fauchet, and S. Wagner, "Mechanism of microcrystalline silicon growth from silicon tetrafluoride and hydrogen," *J. Non-Crystalline Solids*, vol. 114, pt. 2, pp. 816–8, 1989.

4. Y. Okada, J. Chen, I. H. Campbell, P. M. Fauchet, and S. Wagner, "Mechanism of the growth of amorphous and microcrystalline silicon growth from silicon tetra-

fluoride and hydrogen," *J. Applied Physics*, vol. 67, pp. 1757–60, February 15, 1990.

Master's thesis

5. J. C. Chen, H. A. Haus, and E. P. Ippen, "Stability of lasers mode locked by two saturable absorbers," *IEEE J. Quantum Electronics*, vol. 29, pp. 1228–32, April 1993.

Ph.D. thesis

6*. S. Jüngling, J. C. Chen, and F. X. Kärtner, "Novel calculation of higher-order modes of waveguides using beam propagation method," *Optical Society of America Annual Meeting Technical Digest* (Toronto, Canada), October 3–8, 1993, paper TuS2.

7*. J. C. Chen and S. Jüngling, "Efficient eigenmode calculations using imaginary-distance beam propagation method," *Integrated Photonics Research Technical Digest* (San Francisco, CA), February 17–9, 1994, paper ThF7.

8*. J. C. Chen and S. Jüngling, "Computation of higher order waveguide modes by imaginary distance beam propagation method," *Optics and Quantum Electronics*, vol. 29, pp. 199–205, March 1994.

9*. J. C. Chen, "A parallel approach to modeling optical waveguides," *Proceedings of the M.I.T. Student Workshop on Scalable Computing* (Cape Cod, MA), July 21–2, 1994, paper 17.

10*. S. Jüngling and J. C. Chen, "A study and optimization of eigenmode calculations using imaginary-distance beam propagation method," *IEEE J. Quantum Electronics*, vol. 30, pp. 2098–105, September 1994.

11*. J. C. Chen and C. Seo, "Novel reduction of losses in bent waveguides," *Optical Society of America Annual Meeting Technical Digest* (Dallas, TX), October 2–7, 1994, paper ThFF3.

12*. J. C. Chen, H. A. Haus, J. N. Winn, and J. D. Joannopoulos, "Narrow-band optical filters from photonic band gap gratings," *IEEE International Symposium on Guided-Wave Optoelectronics* (Brooklyn, NY), October 26–8, 1994, paper XIII.2.

13. P. S. Martin, J. C. Chen, C. G. Fonstad, and H. A. Haus, "Application of the spectral index method to laser diode design," *J. Lightwave Technology*, vol. 13, pp. 569–74, April 1995.

14*. J. C. Chen, H. A. Haus, S. Fan, and J. D. Joannopoulos, "Optical filters from photonic band gap air bridges," *European Conference on Integrated Optics* (Delft, Netherlands), April 4–9, 1995, paper ThC3.

15*. J. C. Chen, H. A. Haus, S. Fan, P. R. Villeneuve, J. D. Joannopoulos, K. Li, and R. T. Shin, "Optical filters from photonic band gap air bridges," *Proceedings of Photonics Society of Chinese-Americans Annual Meeting* (Baltimore, MD), May 20, 1995.

16. P. R. Villeneuve, S. Fan, I. Kurland, J. C. Chen, and J. D. Joannopoulos (invited), "Photonic band gap structures and devices," *Quantum Electronics and Laser Science Conference* (Baltimore, MD), May 21–6, 1995, paper QWH1.

17. P. R. Villeneuve, S. Fan, J. D. Joannopoulos, K.-Y. Lim, J. C. Chen, G. S. Petrich, L. A. Kolodziejski, and R. Reif, "Microcavities in channel waveguides," *Proceedings of a NATO Advanced Studies Institute on Photonic Band Gap Materials* (Elounda, Greece), June 18–30, 1995.

18. S. Jüngling and J. C. Chen (invited), "Imaginary distance beam propagation for passive and active waveguide structures," *Progress in Electromagnetic Research Symposium* (Seattle, WA), July 24–8, 1995.

19. S. Fan, J. N. Winn, A. Devenyi, J. C. Chen, R. D. Meade, and J. D. Joannopoulos, "Guided and defect modes in periodic dielectric waveguides," *J. Optical Society of America B*, vol. 12, pp. 1267–72, July 1995.

20*. J. C. Chen, H. A. Haus, J. N. Winn, S. Fan, and J. D. Joannopoulos, "Wide stop band optical filters from photonic band gap air bridges," in *Guided-Wave Optoelectronics: Device Characterization, Analysis, and Design* (New York: Plenum Press), 1995, pp. 477–83.

21*. J. C. Chen and K. Li, "Quartic perfectly matched layers for dielectric waveguides and gratings," *Microwave and Optical Technology Lett.*, vol. 10, pp. 319–23, December 20, 1995.

22*. J. C. Chen and C. Seo, "Low transition losses in bent rib waveguides," *J. Lightwave Technology*, April 1996, in press.

23*. J. C. Chen, H. A. Haus, S. Fan, P. R. Villeneuve, and J. D. Joannopoulos, "Optical filters from photonic band gap air bridges," submitted to *J. Lightwave Technology.*

24. J. C. Chen, P. R. Villeneuve, H. A. Haus, and J. D. Joannopoulos, "Narrowband transmission filters from highly resonant gratings," submitted to *Integrated Photonics Research Topical Meeting.* This filter uses a buried oxide geometry.

25. J. C. Chen, I. Kurland, S. Fan, P. R. Villeneuve, and J. D. Joannopoulos, "Microbends in a two dimensional array of photonic band gap rods," monthly photonic band gap seminar series, May 30, 1995. Hopefully, this FDTD calculation and A. Mekis' analytic treatment will be submitted to *Phys. Rev. Lett.* soon.

Appendix B

User notes for BPM program

Summary:

Although not a complete user manual,[1] this appendix gives instructions on how to use the program. In particular, I will detail the input and output files.

The program BPM, which stands for "Beam Propagation Method," can calculate the propagation of electromagnetic waves in 3 dimensional active and passive waveguide structures. Part of the finite difference solver has been developed by Prof. W. P. Huang's group. The shell has been written by J. C. Chen. Appropriate modifications to the imaginary distance propagation — a program option which can calculate waveguide modes more efficiently than using real propagation — have been developed by J. C. Chen and Dr. S. Jüngling.

The kernel of BPM, "VBPM3D" is based on a semi-vectorial finite difference implementation of the differential paraxial wave equation. The numerical implementation allows use of the whole range from a fully implicit to a fully explicit scheme.

The program can handle any arbitrary index distribution. Its interface is particularly well-suited for certain waveguide structures or types — bulk materials, rib waveguides, quantum wells, directional couplers, arbitrary rectangles, tapering geometries, multi-cladded fibers, and isolation trenches. With the choice of a complex index distribution, one can also model gain or loss.

[1] The source code has ample documentation.

The input field distribution is specified in three ways: 1) a gaussian field distribution, 2) an ASCII data file (in a matrix layout), 3) a fortran binary file (with phase information).

The program output can be specified to be one or several files containing electric or magnetic field distributions in the transverse direction. Slices of longitudinal distributions in the x-z plane can be chosen as well. Another output file contains the effective index evaluated at each propagation step. The output files are all written in the standard ASCII format so they can be read in by other programs like matlab or spyglass or other graphic programs. Several matlab routines are available, resulting in a more user friendly interface.

B.1 Input-output in a nutshell

This section briefly introduces how to specify the waveguide structure, how to run the program, and how to read and graph the results.[2] All files that belong to the same structure have the same basename, for example `test.*`. The input or output files do have different extensions such as `*.geom`, `*.sim`, `*.sol`, `*.dex` `*.e00`, `*.m1`, etc.

B.1.1 Input files

***.geom** contains the mesh size, step size, boundary condition of the geometry and how often the calculated field cross sections are stored in files.

***.sim** specifies the input field, the waveguide geometry, the carrier wavelength, and the reference index. The end of the file has information for calculating higher order eigenmodes.

***.sol** deals the matrix inversion. One can chose a forward Euler, backward Euler or Crank Nicholson scheme, specify E or H-fields, pick the number of iterations used in ORTHOMIN (sparse matrix solver).

[2]The gist of this section comes from Dr. Stephan Jüngling's 1993 report to the Swiss National Science Foundation.

***.mtl** can be used to specify any arbitrary waveguide structure. In this case, the file name (without extension) can be specified in the ***.geom** file replacing one of the common structure types (RIDGE, CPLR, ACPLR, etc.).

B.1.2 Output files

***.e00** contains the input field in ASCII format.

***.exx** where xx stands for 01, 02, etc. contains the cross sections of the field profiles that have been specified in *.geom.

***.field** contains the final field profile at the end of the simulation in binary format. It can be used as an input specification to continue the simulation for further propagation by using the DATAF option in the .geom file.

***.mx** is only written if the propagation direction is imaginary. It contains the final field profile of the x-th eigenmode in ASCII-format.

***.eigx** contains the field profile of the x-th eigenmode in binary format. It is used to get the (x+1)-th higher order eigenmode.

***.pwrn0** is an ASCII file containing information on the power in the cross section, and the current propagation constant at each propagation step.

***.sx** contains the x-th xz-slice data of the field distribution.

***.dexsx** contains the corresponding dielectric constant for the x-th field slice.

***.dump** contains further information written at each propagation step.

B.1.3 Structure types

Many common types of waveguide structures have been implemented. The user can specify one of the available structure-types in the .sim file then set the dimensions of

the waveguides. Additional types can be implemented easily, if the available types are not sufficient, but they have to be coded in fortran. Another option is to specify the indices at a grid of points in the ***.mtl** input file. The number of rows and columns in this ASCII file has to be the same as the dimensions nx and ny specified in the .geom file:

RIDGE	for a single ridge structure
CPLR	for a symmetric ridge waveguide coupler
ACPLR	for an asymmetric ridge waveguide coupler.
KLM	for materials with self phase modulation and gain.
NRIB	for ridge built on n-layers (thanks to Paul Martin).
WYC1	for ridge with conformal gratings (thanks to Woo-young Choi).
FIBE	for fibers with arbitrary number of claddings.
TFIB	tapered version of FIBE.
CHU2	for curved ridge and trench (thanks to Chulhun Seo).
RECT	for any geometry that can be decomposed into rectangles.
CTRE	curved and tapered version of RECT.

B.1.4 Modelling propagation

In order to run BPM, one has to adjust the parameters in the input files to the structure of interest. One suggestion is to run first a few BPM steps on a coarse mesh, in order to get a feeling whether the results look ok. A transverse step size in the order of half a wavelength should be reasonable.

The current version of BPM is coded in FORTRAN77. In order to keep the fortran code small and the executable code more efficient, we used some C-preprocessor statements to customize the code to the specific needs of the user. It also allows us to reduce the space of parameter storage in the memory during runtime. Several options are available, that can select the optimal code for the pure real or the imaginary distance propagation.

In order to run **bpm**, one can just type bpm at the command line prompt. The program starts with

```
welcome to BPM solver
enter the base name for inputs (base.geom,.sim,.sol)
```

Here one has to give the filename without extension. Make sure, that the three files *.sim *.geom and *.sol do exist and are matched properly to the structure of interest. and also prints some messages on the current status, like

```
reading test.geom ..
reading test.sim ...
processing gtype = /CPLR/...
```

During run-time several other warnings or numbers are written to the screen, but since they are subject to frequent change, they are not commented further.
One option should be pointed out here: One can always continue the simulation for another few steps by using the DATAF option in the *.sim file and by using the output field as a reentry for the simulation.

B.1.5 Calculating eigenmodes

The imaginary distance option can be used to determine the eigenmodes of the waveguides. Several parameters have to be adjusted correctly.

1. In the *.geom file, make sure the total propagation distance z is imaginary.
2. In the *.sim file, choose the n_0 so that it is 0.2 higher than the core index.
3. If you want higher order eigenmodes, adjust the `neig` and `nsub` parameters in the *.sim file, where the `neig` indicates the n-th eigenmode that is calculated, and `nsub` the frequency of subtraction of the lower order modes.

Note, that with the imaginary distance propagation, the numerical scheme and the step size are different from than of the real propagation. For a fast convergence, one should chose a pure implicit scheme, which corresponds to $\alpha = 1$ in the *.sol file and a very large step size (such as $\Delta z = 10^6$.[9]

Running the imaginary distance propagation, the program should print out a warning

WARNING: this program gives Nth eigenmode

to remind the user the current program mode.

B.2 A propagation example

In this appendix, I simulate the propagation of light down a waveguide. The main text of thesis has a few chapters of eigenmode analysis, so I don't feel the need to beat that subject to death. Let's take the example of side coupled waveguides or directional couplers. Such structures help form the Channel Dropping Filter.[124] The light is confined in the high index ($n = 1.96$) silicon nitrate layer, which is sandwiched between two silicon oxide layers ($n = 1.45$).

The input field distribution $E_x(x, y)$ is equal to the fundamental eigenmode of a single ridge structure (figure B-1). Since part of the field is in the eigenmode of the adjacent waveguide, part of the power leaks to the other guide. After 400 μm, a little more than half the power is transferred to the other guide (figure B-2). This field pattern resembles the symmetric (or fundamental) mode of the two waveguide system. After another 400 μm, all the power has transferred to the other waveguide. And power is starting to couple back into the original guide (figure B-3). Figure B-4 shows the amplitudes of the electric field for over 3 mm of propagation. We can see over two periods of oscillation. During each oscillation, the energy has coupled to the adjacent guide and returned to the initial guide.

Another way to view this phenomena considers the initial input — the eigenmode of a single waveguide — as a superposition of the fundamental symmetric and antisymmetric eigenmodes of the two waveguide system. The modal index of the fundamental symmetric eigenmode is higher than the index of the antisymmetric eigenmode. As a result, the modes travel with a different speed and "fall apart". Since the amplitudes of both eigenmodes are about equal, they interfere constructively or destructively in either ridge guide whenever a phase difference of a multiple

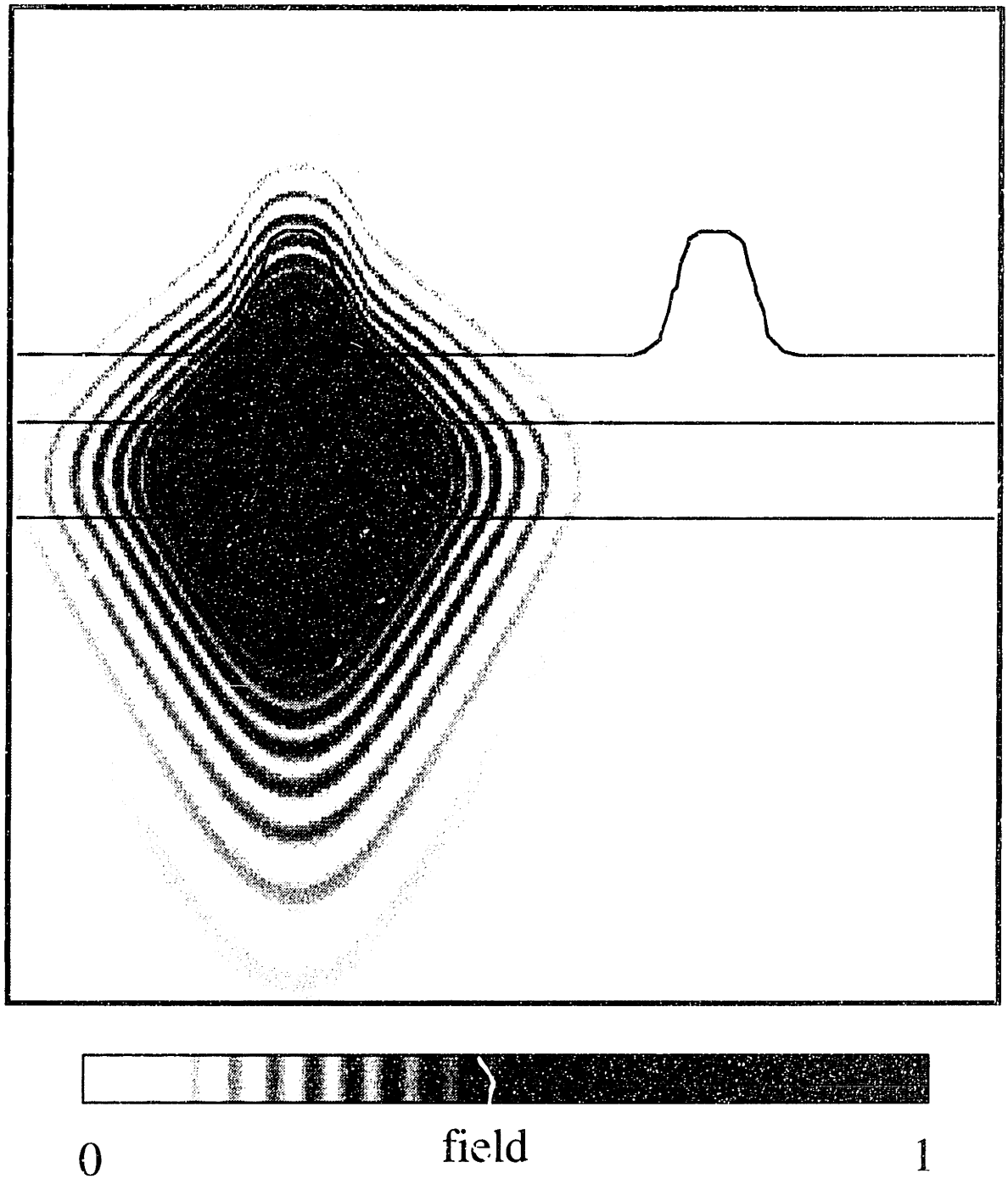

Figure B-1: Electric field at $z = 0\mu$m. The field is eigenmode of the left guide.

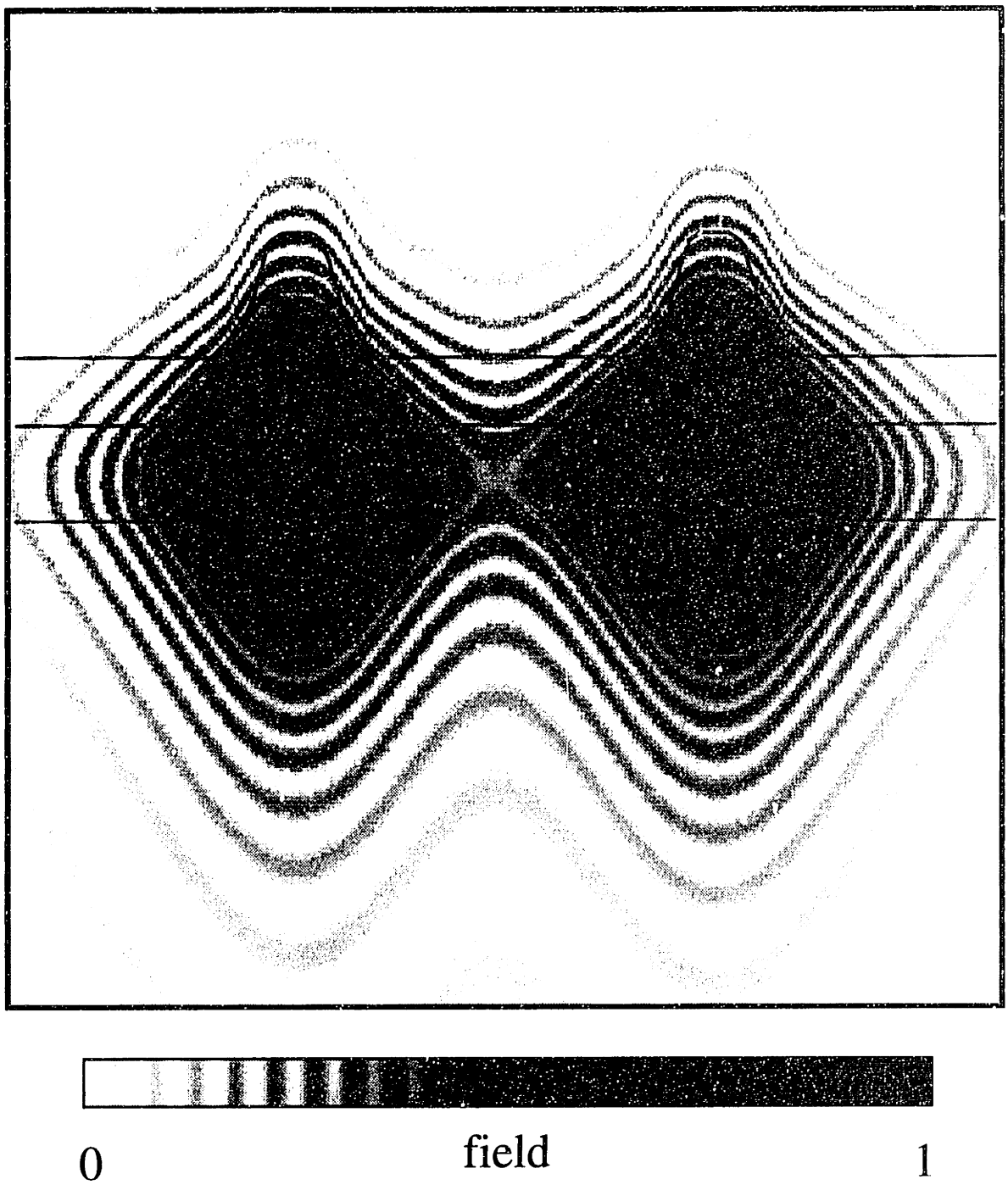

Figure B-2: Electric field at $z = 400\mu$m. About half the field is transferred to the adjacent guide.

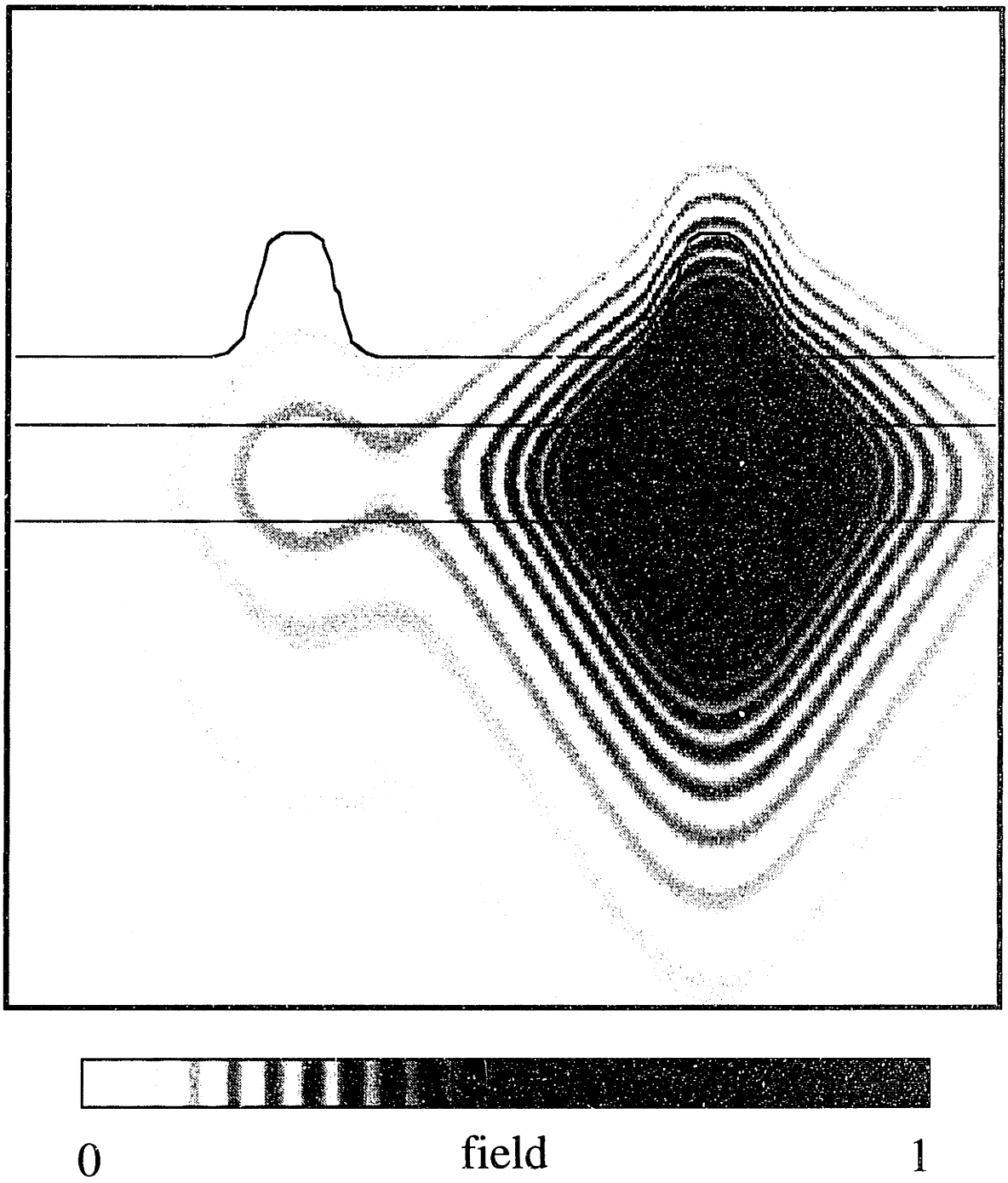

Figure B-3: Electric field at $z = 800\mu$m. Almost all the field is transferred to the adjacent guide.

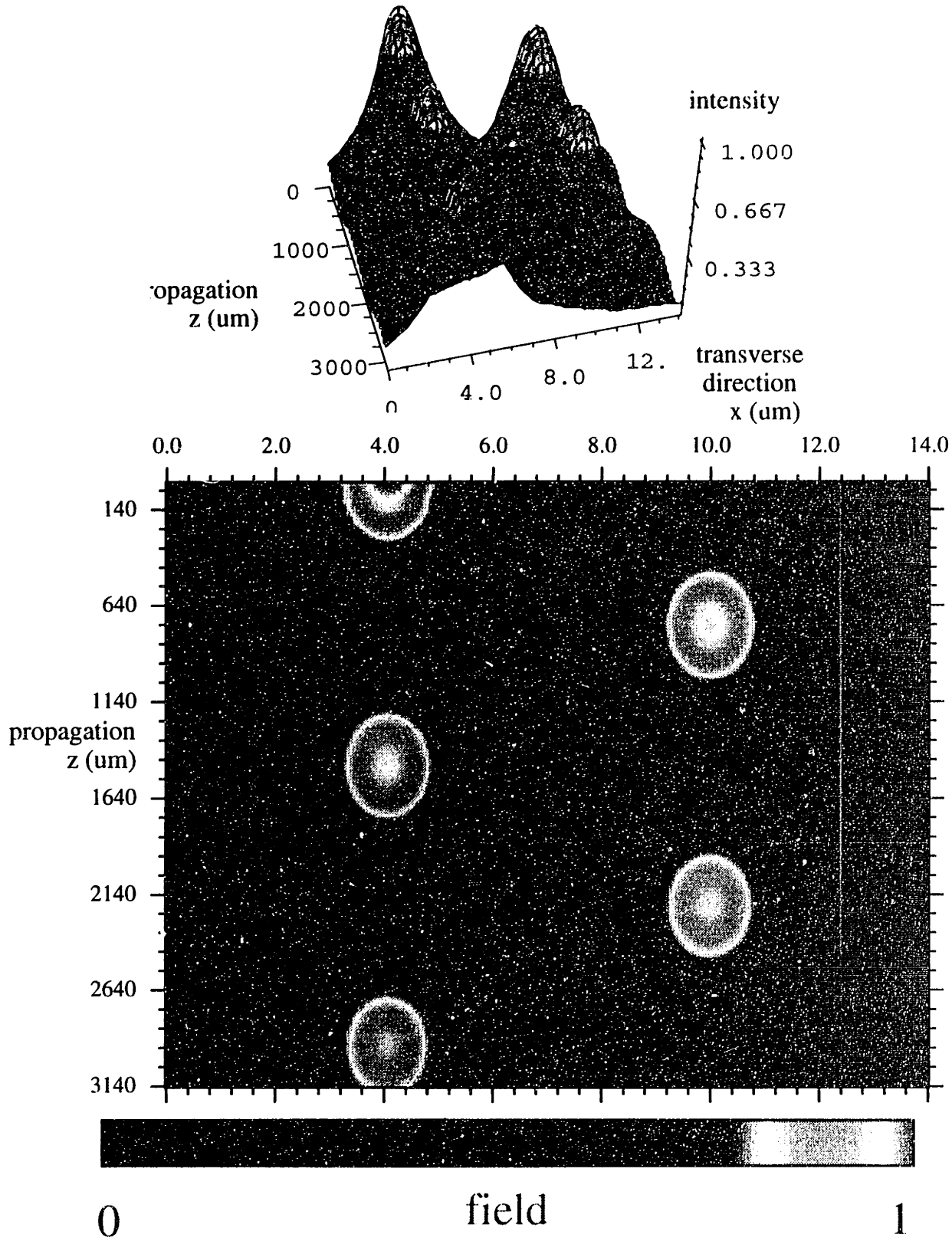

Figure B-4: Electric field propagates down a directional coupler. Notice how the amplitude oscillates between the two guides.

of π accrues. The interference results in a sinusoidal oscillation in energy (figure B-4).

Dependent on all the parameters that have to be determined in order to start the numerical computation, one has to keep in mind that the discrete system is really different from the physical world. By a choice of the wrong parameters for the computation, one may get strange results, with no resemblance to the physical system one wants to describe. One has to worry about the stability and convergence of the numerical scheme, or the accuracy of the result. The reader who is interested in numerical simulations should look into Numerical Recipes.[33] For even more details read Ames.[32] The interested reader can also consult the documented source code and our papers on BPM.

This program is rather user friendly. Just over the last couple years, the executable has been successfully used by many students and researchers: Marcie Black (S.M., Kimerling), Woo-young Choi (Ph.D., Fonstad), Stephan Jüngling[30,31,29,9,27] (postdoc, Haus), Mohammad (Jalal) Khan (S.B., Haus), Desmond Lim (S.M., Kimerling), Paul Martin[159] (Ph.D., Fonstad), Chulhun Seo[154,146] (visiting scientist, Haus & Fonstad), Constantine (Costas) Tziligakis (S.M., Ippen), and Vince Wong (Ph.D., Smith). It is not difficult.

Appendix C

User notes for vector FDTD program

C.1 Specifications

Here I will describe how to use the vector finite difference time domain (FDTD) code. This code is one of the few FDTD programs with the revolutionary Perfectly Matched Layers (PML). This comes from Dr. Kevin Li, a Ph.D. student of Prof. Kong and Dr. Shin. It includes my improvements to this new boundary condition. I have built the entire user interface. In addition, this code can now model nonuniform, dielectric geometries. As a result, we have calculated the reflection, transmission, and radiation through an arbitrary object. And for resonators, we have found the frequency, quality factor and field distribution of the high "Q" mode.

I will not describe the interface for the scalar-like finite difference time domain code because details of its operation are described in chapter 5. My collaborator, Josh Winn, also describes part of the code in his master's thesis.[176] This program can calculate energies and fluxes accurately, but for transmission studies the vector code with PML boundaries is far superior.

C.2 User interface

C.2.1 Transmission example

First, I will explain how to calculate the transmission and reflection for the air bridge with 33 notch pairs (figure 7-2). One must set parameters in three places: the source code `fdtd-2d.F`, the header file `type.h` and finally the input file.

In the source code, one chooses the size of the geometry, which extends from (-maxx,-maxy) to (maxx,maxy), by setting the parameter variables, `maxx` and `maxy`. The pulse width of the source defaults to 1/frequency. But this can be overridden; to change this, insert the proper scaling after the line, `pw=c0*pw`. For the bridge, I used the default pulse width but set `maxx = 50, maxy = 200`.

One should also chose the polarization — TE or TM — in header file `type.h`. For the notched bridge example, this file was

```
#define STOREEPS
c#define HZ
#define EZ
```

Since the line "`#define HZ`" is commented, only the sections of code that deal with TE waves are compiled. Therefore, the program will then calculate only the E_z (and H_x and H_y) polarizations; the H_z (and E_x and E_y) components will NOT be modelled. To model TM waves, uncomment the line with HZ and comment the line with EZ. This use of C preprocessor statements is portable and produces small executables, without sacrificing generality. The statement STOREEPS means that the dielectrics are stored in core memory so the program runs faster but uses more memory. If this statement were undefined, the dielectric arrays are not stored; instead, an array points to their dielectric values.

Next, I will describe the input file that generate figure 7-5. The input is from the keyboard, which the designers of C call STDIN.[1] The text following the '!' are comments, only for the user's benefit; the program reads but ignores them.

[1] In UNIX and DOS, a file can be redirected to STDIN with '<'.

```
2.664e-8 2.664e-8 1.e-8 !  dx dy dz in meters (520x30)
```

This is the grid size. Δz is ignored.

```
3 !  source time type (0 none, 1 cw, 3 pulse)
```

Here select type of input excitation. NOTE: a pulse is gaussian in time.

```
200.  !  source freq in ThZ
```

This is the source's carrier frequency.

```
-2 !  source transverse type (-2fund,-1file,0flat,>0sin)
```

The transverse profile of the source can be

- -3 the fundamental mode of a general waveguide (using Dr. Brent Little's mode solver[2]),
- -2 the fundamental mode of the waveguide (for a high index waveguides surrounded by a low index region),
- -1 read in from a file (prof.dat),
- 0 constant,
- >0 sinusoidal with >0 zeros.

```
-20 20 -490 -490 !  source location (xlo,xhi,ylo,yhi)
```

The location in grid points. The source must be a horizontal line, a vertical line or a point.

```
0 0 0 0 0 !  no spatial gaussian.  0 to end
```

Another input possibility is a gaussian in space. 0 means no gaussians.

```
2097152 !  number time steps nt
```

For efficient FFTs, this should be a power of 2. Δt is calculated, by dividing the CFL maximum (see (1.4)) by 1.05.

```
10000 !  number iterations between field files
```

[2]The algorithm comes from Vassallo's book.[177]

So, every 10000 time steps, all the fields will be written to disk. (At time $t = 1000$, the program write `ez.01`, `hx.01`, `hy.01` for TE and `hz.01`, `ex.01`, `ey.01` for TM. And at $t = 2000$, `ez.02`, etc.

```
2 !  number of points to monitor
```

The files `pt.ez` and `pt.hz` contain the fields for every time step. Getting the transmission and reflection spectrum requires two points — one before the filter and one after.

```
-999 -470 1 !  location of pt to be monitored (-999 for mode)
-999 500 1 !  location of pt to be monitored (-999 for mode)
```

The location of the points are given in (x,y,z) pairs. The unit is grid point location. If either x or y value equals -999, the fundamental mode as calculated in the source section is used.[3] Output goes to `pt.ez` with the first column the time step, the second the field-mode overlap at $y = -470$, and the third $y = 500$.

```
0 !  measure energy?  (0 none, 1 yes)
-30 30 -20 120 !  integrate over (xlo,xhi,ylo,yhi)
```

Should the energy inside a box be calculated? The next line specifies the dimensions in grid points.

```
0 !  number of flux lines (ExH)
```

This allows the calculation of flux crossing arbitrary line segments. 0 means no flux calculations.

This next section defines the dielectric constants over circular and rectangular regions. If two regions overlap in an area, the one entered last overrides.

```
0 !  obj type (0rect, 1circ, -1file, 999end)
```

[3]In the event that the field at position -999 is desired, the value can be set to something else. Just set parameter `imode`.

Choose 0 for rectangle. If -1 is chosen as the *first* object, the permittivity is read from a file `eps.out`.

```
11.56 -5 5 -10000 10000 !  epsilon,xlo,xhi,ylo,yhi
```

This rectangle with $\epsilon = 13$ extends from (-5,-10000) to (5,10000). The program is smart enough to notice that $y = 10000$ and $y = -10000$ are out of the computational region, so it sets $y = maxy$ and $y = -maxy$.

```
0 0 0 0 0 !  index to vary (0 for none) then init,fin,step
```

This line is useful for replicating a region. Since the first number is 0, no replication occurs.

```
0 !  obj type (0rect, 1circ, 999end)
1.  -5 -4 -180 -176 !  epsilon,xlo,xhi,ylo,yhi
4 140 10 5 10 !  index to vary (0 for none), fin,step,ind,step
```

This sets the notches on the bottom, left side of the quarter wave shift. The second line sets the location of first notch. The third line says the 4th integer on the second line is to be incremented by 10 until it equals 140, while the 5th integer is also incremented by 10.

```
0
1.  4 5 -180 -176 !  epsilon,xlo,xhi,ylo,yhi
4 140 10 5 10 !  index to vary (0 for none),fin,step,ind,step
```

This sets the notches on the top, left side of the quarter wave shift.

```
0
1.  -5 -4 155 159 !  epsilon,xlo,xhi,ylo,yhi
4 475 10 5 10 !  index to vary (0 for none), fin,step,ind,step
```

This sets the notches on the bottom, right side of the quarter wave shift.

```
0
1.  4 5 155 159 !  epsilon,xlo,xhi,ylo,yhi
4 475 10 5 10 !  index to vary (0 for none), fin,step,ind,step
```

This sets the notches on the top, right side of the quarter wave shift.

```
999 !  999 to run now
```

999 tells the program that the definition of dielectric regions or objects is finished.

The first ten or so cycles of E_z at $y = -470$ (see second column of `pt.ez`) should be FFT-ed to give the input spectrum. The FFT of remaining time steps gives the reflected spectrum. The FFT of the third column gives the transmission spectrum. Both the reflected and transmission spectrum need to be normalized by the input spectrum to yield the reflected and transmitted *amplitudes*.

C.2.2 Resonator example

Here I will describe how to calculate the Q of the air bridge with circular holes (chapter 8).

First of all, the air bridge is shorter so the maxx=50 and maxy=140. And in `type.h`, "#define HZ" should be uncommented. Here is the input file. I will comment on only those lines that differ from the previous example.

```
  1.739e-8 1.739e-8 1.e-8 !  dx dy dz in meters (50x140)


  0 !  source time type (0 none, 1 cw, 3 pulse)
200.  !  source freq in ThZ
-2 !  source transverse type (-2fund,-1file,0flat,>0sin)
-30 30 20 20 !  source location (xlo,xhi,ylo,yhi)


10.e10 0 54 10.  10.  !  F2I2F spatial gaussian (amplitude,xcent,ycent,wx,wy)
3.e10 0 40 10.  4.  !  F2I2F spatial gaussian (amplitude,xcent,ycent,wx,wy)
-3.e10 0 68 10.  4.  !  F2I2F spatial gaussian (amplitude,xcent,ycent,wx,wy)
0 0 0 0 0 !  no spatial gaussian.  0 to end
```

Note that there is NO time dependent source, but the initial field (at $t = 0$) is three gaussians in space. Their radius in the x and y directions are set

in the fourth and fifth columns. The first column sets the amplitude, and the second and third set the location of the gaussian's center. A line of zeros terminates the input.

```
40000 !  number time steps nt
10000 !  number iterations between field files, nslide


1 !  number of points to monitor
0 54 1 !  location of pt to be monitored (-999 for mode)
```

The temporal oscillations in monitored point, which is written to `pt.hz`, give the eigenmode frequency.

```
1 !  measure energy?  (0 none, 1 yes)
-30 30 -20 120 !  integrate over (xlo,xhi,ylo,yhi)
3 !  number of flux lines (ExH)
-12 12 120 120 !  flux over (xlo,xhi,ylo,yhi)
-30 30 120 120 !  flux over (xlo,xhi,ylo,yhi)
30 30 -20 120 !  flux over (xlo,xhi,ylo,yhi)
```

The fluxes and energies are written to `fl.hz` and `en.hz`. Here the fluxes $E \times H$ are calculated at three line segments.

```
0 !  obj type (0rect, 1circ, -1file, 999end)
13.  -12 12 -10000 10000 !  epsilon,xlo,xhi,ylo,yhi
0 0 0 0 0 !  index to vary (0 for none) then init,fin,step
1
1.  0 0 7.2 !  epsilon,xcent,ycent,radius
3 40 20 0 0 !  index to vary (0 for none), fin,step,ind,stop
1
1.  0 68 7.2 !  epsilon,xcent,ycent,radius
3 108 20 0 0 !  index to vary (0 for none), fin,step,ind,step
```

The dielectric objects or regions follow the same conventions as before. The circles are defined with the epsilon in first column, center position in

the next two, the radius in the last column. As usual, the units are in grid points.

```
999 !  999 to run now
```

At large times, the logarithm of energy from `en.hz` resembles a straight line. From the slope of this curvefitted line, the quality factor can be extracted. And at large times, the field files — `hz.*`, `ex.*`, `ey.*` — are the eigenmode. And the monitor file, `pt.hz`, can be fitted to a sine, giving the resonant frequency.

C.3 Program architecture

What comprises this program? Here is the bytes, dates and names of the source code.

```
  861 Sep 11 13:40 Makefile
16075 Sep 11 13:40 blprof.F
11625 Mar 24  1995 epabc.F
 2937 Mar 27  1995 escat.F
45655 Sep 11 16:19 fdtd-2d.F
 5938 Mar 19  1995 hpabc.F
 3200 Mar 27  1995 hscat.F
 7230 Sep 11 13:40 prof.F
   41 Apr 21  1995 type.h
```

`Makefile` is program that automates compilation of the code (for the Cray, HP, RS6000, Sun, etc.) so typing `make` will compile the code. `blprof.F` is Dr. Brent Little's mode solver. `epabc.F` and `hpabc.F` implement the PML boundary condition for electric and magnetic fields, respectively. `escat.F` and `hscat.F` propagate the electric and magnetic fields forward in time. `fdtd-2D.F` handles most of the input and output. It also evaluates energies and fluxes, and sets up the permittivity. `prof.F` is my mode solver. `type.h` is a header file that sets the polarization of the field and storage of the permittivity. For more details, see the documentation within the source code.

I would also like to give some advice on how to write more maintainable code. This unsolicited section is a reaction to some of the programs I have seen. This is written to those familiar with UNIX environment programming and those who know the common terminology found in computer science courses. If these concepts seem foreign, please consult your UNIX man pages[4] or read a textbook.[i78]

1. Familiarize yourself with your operating system's programming utilities. For example, in UNIX (which is the standard for the Crays, CM5's, and most workstations), helpful tools are `make`, which automates source code compilation, and `dbx`, which is a nice debugger. The `emacs` editor offers a FORTRAN mode. Type `ctrl-h m` to see the various commands. My favorite, `ctrl-c ctrl-r`, brings up a ruler. And emacs's `Meta-x compile`, used with `ctrl-x '`, lets one parse through errors automatically.

2. A shareware utility `ftnchek` acts as a FORTRAN version of C's `lint`. It checks FORTRAN code for possible errors and warns of nonportable constructs. You can ftp this from `netlib.att.com`.

3. It also helps to define all variables explicitly. This catches typos; use `implicit none`.

4. Be sure to document. This helps to refresh one's memory when one must add to the code.

5. When I started here, I used VAX 3100's (2 Megaflops), but later got access to faster workstations, IBM ES 9000 mainframes, Thinking Machine CM5, and mostly recently an one Gigaflop Cray C90. Writing portable, machine independent code made my life easier.

6. In large codes, some parameters have to be set in many subroutines. One can set these parameter statements for all these routine in only one place. One can use include files (not portable; necessitates recompilation of every affected subroutine). Or one can pass the parameters via subroutine calls.

[4] At the UNIX prompt, type `man` or `xman`.

7. Use archival tools to keep track of revision history and to store old versions compactly. Of the two standard ones (SCCS and RCS), I had good experience with `rcs`. For several source files, some recommend CVS. Personally, I just used `shar.3.50 -V`[5] then `rcs`. For details, `man rcsintro`.

8. Some codes are extremely versatile; they can do many things. Such programs are often too cumbersome to debug and too large to run. Introducing C preprocessor statements is a portable way to modularize a large source. For example, our bpm code used one cpp define statement for calculating higher order eigenmodes, one for updating neff every step, one for normalizing large fields, etc. Running `/lib/cpp` filters the code of extraneous, unused sections. And sometimes testing and debugging is helped by the ability to comment out sections.

To my fellow programmers, best wishes and happy coding!

C.4 Conclusion

I have explained the relevant input files, giving two practical examples of how to use the program. For example, I have shown how to calculate the reflection and transmission coefficients of arbitrary objects. This program can also find the properties of the high Q eigenmodes. And for the more curious, I have also given a brief overview of the program structure and some advice on writing "good" code.

[5]On athena, `add watchmaker`.

Bibliography

[1] J. V. Roey, J. van der Donk, and P. E. Lagasse, "Beam-propagation method: Analysis and assessment," *J. Opt. Soc. Am. B*, vol. 71, pp. 803–10, July 1981.

[2] Y. Chung and N. Dagli, "An assessment of finite difference beam propagation method," *IEEE J. Quant. Electron.*, vol. 26, pp. 1335–9, August 1990.

[3] B. M. A. Rahman and J. B. Davies, "Finite-element solution of integrat optical waveguides," *J. Lightwave Technol.*, vol. LT-2, pp. 682–8, October 1984.

[4] M. S. Stern, "Semivectorial polarised finite difference mehod for optical waveguides with arbitrary index profiles," *IEE Proc. J*, vol. 135, pp. 56–63, February 1988.

[5] W. P. Huang, S. T. Chu, and S. K. Chaudhuri, "A semivectorial finite-difference time-domain method," *IEEE Photon. Technol. Lett.*, vol. 3, pp. 803–6, September 1991.

[6] G. R. Hadley, "Transparent boundary condition for beam propagation," *Opt. Lett.*, vol. 16, pp. 624–6, May 1991.

[7] G. R. Hadley, "Transparent boundary condition for the beam propagation method," *IEEE J. Quantum Electron.*, vol. 28, pp. 363–70, January 1992.

[8] G. H. Song, "Transparent boundary conditions for beam-propagation analysis from the Green's function method," *J. Opt. Soc. Am. A*, vol. 10, pp. 896–904, May 1993.

[9] S. Jüngling and J. C. Chen, "A study and optimization of eigenmode calculations using imaginary-distance beam propagation method," *IEEE J. Quantum Electron.*, vol. 30, pp. 2098–105, September 1994.

[10] D. Yevick and M. Glasner, "Analysis of forward wide-angle light propagation in semi-conductor rib waveguides and integrated-optic structures," *Electron. Lett.*, vol. 25, pp. 1611–3, 1989.

[11] G. R. Hadley, "Wide-angle beam propagation using Padé approximant operators," *Opt. Lett.*, vol. 17, pp. 1426–8, October 1992.

[12] W. P. Huang and C. L. Xu, "A wide-angle vector beam propagation method," *IEEE Photon. Technol. Lett.*, vol. 4, pp. 1118–20, October 1992.

[13] H. J. W. M. Hoekstra, G. J. M. Krijnen, and P. V. Lambeck, "New formulation of the beam propagation method based on the slowly varying envelope approximation," *Optics Comm.*, vol. 97, pp. 301–3, April 1993.

[14] P. Kaczmarski, "Bidirectional beam propagation method," *Electron. Lett.*, vol. 24, pp. 675–6, May 26, 1988.

[15] R. Baets, P. Kaczmarski, and P. Vankwikelberge, "Design and modelling of passive and active optical waveguide devices," in *Waveguide Optoelectronics* (J. H. Marsh and R. M. D. L. Rue, eds.), pp. 21–71, Kluwer Academic Publishers, 1992.

[16] H.-P. Nolting and R. März, "Results of benchmark tests for different numerical BPM algorithms," *J. Lightwave Technol.*, vol. 13, pp. 216–24, February 1995.

[17] A. Behie and P. K. W. Vinsome, "Block iterative methods for fully implicit reservoir simulations," *Soc. of Pet. Eng. J.*, pp. 658–68, October 1982.

[18] M. D. Feit and J. A. Fleck, Jr., "Light propagation in graded-index optical fibers," *Appl. Optics*, vol. 17, pp. 3990–8, December 1978.

[19] M. D. Feit and J. A. Fleck, Jr., "Computation of mode eigenfunctions in graded-index optical fibers by the propagating beam method," *Appl. Optics*, vol. 19, pp. 2240–6, July 1980.

[20] M. Gault, P. A. Mawby, and M. S. Towers, "Solution to the wave equation in the numerical simulation of buried heterostructure lasers," *IEE Proc. J*, vol. 140, pp. 44–8, February 1993.

[21] D. Yevick and B. Hermansson, "Numerical analysis of the modal eigenfunctions of chirped and unchirped multiple-stripe-geometry laser arrays," *J. Opt. Soc. Am. A*, vol. 4, pp. 379–90, February 1987.

[22] R. P. Ratowsky, J. A. Fleck, Jr., and M. D. Feit, "Helmholtz beam propagation in rib waveguides and couplers by iterative Lanczos reduction," *J. Opt. Soc. Am. A*, vol. 9, pp. 265–73, February 1992 1992.

[23] D. Yevick and B. Hermansson, "New formulations of the matrix beam propagation method: Application to rib waveguides," *IEEE J. Quantum Electron.*, vol. 25, pp. 221–9, February 1989.

[24] D. Yevick and B. Hermansson, "New approach to lossy optical waveguides," *Electron. Lett.*, vol. 21, pp. 1029–30, October 1985.

[25] R. J. Hawkins, "Propagation properties of single-mode dielectric waveguide structures: A path integral approach," *Appl. Opt.*, vol. 26, pp. 1183–8, April 1987.

[26] D. Yevick and W. Bardyszewski, "Correspondence of variational finite-difference (relaxation) and imaginary-distance propagation methods for modal analysis," *Opt. Lett.*, vol. 17, pp. 329–30, March 1992.

[27] S. Jüngling and J. C. Chen, "Imaginary distance beam propagation for passive and active waveguide devices," in *Progress in Electromagnetic Research Symposium* (Seattle, WA), July 24–8, 1995. paper MH5.

[28] C. L. Xu, W. P. Huang, and S. K. Chaudhuri, "Efficient and accurate vector mode calculations by beam propagation method," *J. Lightwave Technol.*, vol. 11, pp. 1209–15, July 1993.

[29] J. C. Chen and S. Jüngling, "Efficient eigenmode calculations using imaginary-distance beam propagation method," in *Integrated Photonics Research Conference* (San Franscico), February 17–9, 1994.

[30] S. Jüngling, J. C. Chen, and F. X. Kärtner, "Novel calculation of higher order mode of waveguides using beam propagation method," in *Optical Society of America Annual Meeting* (Toronto, Canada), October 3–8, 1993. paper TuS2.

[31] J. C. Chen and S. Jüngling, "Computation of higher order waveguide modes by imaginary-distance beam propagation method," *Optics and Quantum Electron.*, vol. 26, pp. S199–205, March 1994.

[32] W. F. Ames, *Numerical Methods for Partial Differential Equations.* Boston: Academic Press, 3rd ed., 1992.

[33] W. H. Press, B. P. Flannery, S. A. Teukolsky, and W. T. Vetterling, *Numerical Recipes: The Art of Scientific Computing (FORTRAN Version).* Cambridge: Cambridge University Press, 1989.

[34] K. S. Yee, "Numerical solution of initial boundary value problems involving Maxwell's equations in isotropic media," *IEEE Trans. Ant. Prop.*, vol. AP-14, pp. 302–7, May 1966.

[35] J. C. Chen, "A parallel approach for modelling optical waveguides," in *Proceedings of the 1994 M.I.T. Student Workshop on Scalable Computing* (Cape Cod, MA), July 21–2, 1994. paper 17.

[36] T. G. Moore, J. G. Blaschak, A. Taflove, and G. A. Kriegsmann, "Theory and application of radiation boundary operators," *IEEE Trans. Antennas Propagat.*, vol. 36, pp. 1797–1812, December 1988.

[37] B. Engquist and A. Majda, "Absorbing boundary conditions for the numerical simulation of waves," *Math. Computat.*, vol. 31, no. 139, pp. 629–51, 1977.

[38] G. Mur, "Absorbing boundary conditions for the finite difference approximation of the time-domain electromagnetic-field equations," *IEEE Trans. Electromag. Compat.*, vol. EMC-23, pp. 377–82, November 1981.

[39] R. L. Higdon, "Absorbing boundary conditions for difference approximations to the multi-dimensional wave equation," *Math. Comput.*, vol. 47, pp. 437–459, October 1986.

[40] L. N. Trefethen and L. Halpern, "Well-posednesss of one-way wave equations and absorbing boundary conditions," *Math. Computat.*, vol. 47, pp. 421–35, October 1986.

[41] J. G. Blaschak and G. A. Kriegsmann, "A comparative study of absorbing boundary conditions," *J. Comput. Phys.*, vol. 77, pp. 109–139, 1988.

[42] E. L. Lindman, ""Free-space" boundary conditions for the time dependent wave equation," *J. Comput. Phys.*, vol. 18, pp. 66–78, 1975.

[43] P. A. Tirkas, C. A. Balanis, and R. A. Renaut, "Higher order absorbing boundary-conditions for the finite-difference time-domain method," *IEEE Trans. Antennas Propagat.*, vol. 40, pp. 1215–1222, October 1992.

[44] J. Fang, "Investigation of the stability of absorbing boundary conditions for the time-domain finite-difference method," in *IEEE Antennas and Propagat. Soc. Int. Symposium*, vol. 1 (Chicago, IL), pp. 548–551, July 1992.

[45] K. K. Mei and J. Fang, "Superabsorption—A method to improve absorbing boundary conditions," *IEEE Trans. Antennas Propagat.*, vol. 40, pp. 1001–1010, September 1992.

[46] A. Bayliss and E. Turkel, "Radiation boundary conditions for wave-like equations," *Comm. Pure Appl. Math.*, vol. 33, pp. 707–725, 1980.

[47] A. Bayliss, M. Gunzburger, and E. Turkel, "Boundary conditions for the numerical solution of elliptic equations in exterior regions," *SIAM J. Appl. Math.*, vol. 42, no. 2, pp. 430–451, 1982.

[48] G. A. Kriegsmann, A. Taflove, and K. R. Umashankar, "A new formulation of electromagnetic wave scattering using an on-surface radiation boundary condition approach," *IEEE Trans. Antennas Propagat.*, vol. AP-35, pp. 153–61, February 1987.

[49] J.-P. Berenger, "A perfectly matched layer for the absorption of electromagnetic waves," *J. Computat. Phys.*, vol. 114, pp. 185–200, October 1994.

[50] J. D. Moerloose and M. A. Stuchly, "Behavior of Berenger's ABC for evanescent waves," *IEEE Microwave Guided Wave Lett.*, vol. 5, pp. 1344–6, October 1995.

[51] R. Holland, "Finite-difference time-domain (FDTD) analysis of magnetic diffusion," *IEEE Trans. Electromagn. Compat.*, vol. 36, pp. 32–39, February 1994.

[52] C. M. Rappaport, "Perfectly matched absorbing boundary conditions based on anisotropic lossy mapping of space," *IEEE Microwave Guided Wave Lett.*, vol. 5, pp. 90–92, March 1995.

[53] Ü. Pekel and R. Mittra, "Mesh truncation in the Finite-Element Freqeuency Domain with a Perfectly Matched Layer (PML) applied in conjunction with analytic and numerical absorbing boundary conditions," *Microwave Opt. Technol. Lett.*, vol. 9, pp. 176–80, July 1995.

[54] A. Taflove, "Advances in finite-difference time-domain (FD-TD): Numerical modeling techniques for Maxwell's equations," in *Ninth International Conference on Antennas and Propagation* (Eindhoven, The Netherlands), pp. 53–8, IEE, April 4–7, 1995.

[55] J. C. Chen and K. Li, "Quartic perfectly matched layers for dielectric waveguides and gratings," *Microwave Opt. Technol. Lett.*, December 20, 1995.

[56] D. S. Katz, E. T. Thiele, and A. Taflove, "Validation and extension to three dimensions of the Berenger PML absorbing boundary condition for FD-TD meshes," *IEEE Microwave Guided Wave Lett.*, vol. 4, pp. 268–70, August 1994.

[57] C. E. Reuter, R. M. Joseph, E. T. Thiele, D. S. Katz, and A. Taflove, "Ultrawideband absorbing boundary condition for termination of waveguiding structures in FD-TD simulations," *IEEE Microwave Guided Wave Lett.*, vol. 4, pp. 344–6, October 1994.

[58] E. A. Navarro, C. Wu, P. Y. Chung, and J. Litva, "Application of PML superabsorbing boundary condition to non-orthogonal FDTD," *Electron. Lett.*, vol. 30, pp. 1654–6, September 1994.

[59] W. C. Chew and W. H. Weedon, "A 3D perfectly matched medium from modified Maxwell's equations with stretched coordinates," *Microwave Opt. Technol. Lett.*, vol. 7, pp. 599–604, September 1994.

[60] Ü. Pekel and R. Mittra, "A finite element-method frequency domain application of the Perflectly Matched Layer (PML) concept," *Microwave Opt. Technol. Lett.*, vol. 9, pp. 117–22, June 20, 1995.

[61] C. Eswarappa and W. J. R. Hoefer, "Implementation of Berenger's absorbing boundary conditions in TLM by interfacing FDTD perfectly matched layers," *Electron. Lett.*, vol. 31, pp. 1264–6, July 20, 1995.

[62] K. L. Shlager and J. B. Schneider, "A selective survey of the finite-difference time-domain literature," *IEEE Antennas Propagat. Magazine*, vol. 37, pp. 39–57, August 1995.

[63] E. K. Miller, "Time-domain modeling in electromagnetics," *J. Electromag. Waves and Appl.*, vol. 8, pp. 1125–72, September 1994.

[64] J. A. Kong, *Progress in Electromagnetic Research (PIER)*. New York: Elsevier, multi-volume series, 1989–.

[65] K. S. Kunz and R. J. Luebbers, *The Finite Difference Time Domain Method for Electromagnetics.* Boca Raton, FL: CRC Press, 1993.

[66] A. Taflove, *Computational Electrodynamics: The Finite-Difference Time-Domain Method.* Boston, MA: Artech House, 1995.

[67] P. H. Aoyagi, J.-F. Lee, and R. Mittra, "A hybrid Yee algorithm / scalar-wave equation approach," *IEEE Trans. Microwave Theory and Techniques*, vol. 41, pp. 1593–600, September 1993.

[68] J. C. Chen, H. A. Haus, J. N. Winn, and J. D. Joannopoulos, "Narrow-band optical filters from photonic band gap gratings," in *IEEE International Symposium on Guided Wave Optoelectronics* (Brooklyn, NY), October 26–28, 1994. paper XIII.2.

[69] J. C. Chen, H. A. Haus, J. N. Winn, S. Fan, and J. D. Joannopoulos, "Wide stop band optical filters from photonic band gap air bridges," in *Guided Wave Optoelectronics: Device Characterization, Analysis and Design* (T. Tamir, H. Bertoni, and G. Griffel, eds.), Plenum Press, in press.

[70] S. Fan, P. R. Villeneuve, R. D. Meade, and J. D. Joannopoulos, "Guided and defect modes in periodic dielectric waveguides," *Appl. Phys. Lett.*, vol. 65, pp. 1466–8, September 12, 1994.

[71] J. C. Chen, H. A. Haus, S. Fan, P. R. Villeneuve, J. D. Joannopoulos, K. Li, and R. T. Shin, "Optical filters from photonic band gap air bridges," in *Proceedings of the Photonics Society of Chinese-Americans Annual Meeting* (Baltimore, MD), May 21, 1995.

[72] J. C. Chen, H. A. Haus, S. Fan, P. R. Villeneuve, and J. D. Joannopoulos, "Optical filters from photonic band gap air bridges." submitted to *J. Lightwave Technol.*, 1995.

[73] S. Fan, J. N. Winn, A. Devenyi, J. C. Chen, R. D. Meade, and J. D. Joannopoulos, "Guided and defect modes in periodic dielectric waveguides," *J. Opt. Soc. Am. B*, vol. 12, pp. 1267–72, July 1995.

[74] J. D. Joannopoulos, R. D. Meade, and J. N. Winn, *Photonic Crystals: Molding the Flow of Light.* Princeton, NJ: Princeton University Press, 1995.

[75] E. Yablonovitch, T. J. Gmitter, and K. M. Leung, "Photonic band-gap structure: The face-centered-cubic case employing non-spherical atoms," *Phys. Rev. Lett.*, vol. 67, pp. 2295–8, October 21, 1991.

[76] S. Satpathy, Z. Zhang, and M. R. Salehpour, "Theory of photon bands in three-dimensional periodic dielectric structures," *Phys. Rev. Lett.*, vol. 64, pp. 1239–42, March 12, 1990.

[77] K. M. Leung and Y. F. Liu, "Photon band structures: The plane-wave method," *Phys. Rev. B.*, vol. 41, pp. 10188–90, May 15, 1990.

[78] K. M. Leung and Y. F. Liu, "Full vector wave calculation of photonic band structures in face-centered-cubic dielectric media," *Phys. Rev. Lett.*, vol. 65, pp. 2646–9, November 19, 1990.

[79] R. D. Meade, A. M. Rappe, K. D. Brommer, J. D. Joannopoulos, and O. L. Alherhand, "Accurate theoretical analysis of photonic band-gap materials," *Phys. Rev. B*, vol. 48, pp. 8434–7, September 1993.

[80] H. S. Sözüer, J. W. Haus, and R. Inguva, "Photonic bands: Convergence problems with plane wave method," *Phys. Rev. B*, vol. 45, pp. 296–302, June 15, 1992.

[81] P. R. Villeneuve and M. Piché, "Photonic bandgaps: What is the best numerical representation of periodic structures," *J. Mod. Optics*, vol. 41, pp. 241–56, February 1994.

[82] J. B. Pendry and A. MacKinnon, "Calculation of photon dispersion relation," *Phys. Rev. Lett.*, vol. 69, pp. 2772–5, November 9, 1992.

[83] J. B. Pendry, "Photonic band structure," *J. Mod. Optics*, vol. 41, no. 2, pp. 209–29, 1994.

[84] M. Scalora and M. E. Crenshaw, "A beam propagation method that handles reflections," *Optics Commun.*, vol. 108, pp. 191–6, June 1994.

[85] K. M. Leung, "Defect modes in photonic band structures: A Green's function approach using vector Wannier functions," *J. Opt. Soc. Am. B*, vol. 10, pp. 303–6, February 1993.

[86] K. M. Leung and Y. Qiu, "Defect modes in photonic band structures: A Green's function approach using vector Wannier functions," *Phys. Rev. B*, vol. 48, pp. 7767–71, September 15, 1993.

[87] S. John, "Strong localization of photons in certain disordered dielectric superlattices," *Phys. Rev. Lett.*, vol. 58, pp. 2486–9, June 8, 1987.

[88] E. Yablonovitch, "Photonic band structure: The face-centered-cubic case," *Phys. Rev. Lett.*, vol. 63, pp. 1950–3, October 30, 1989.

[89] K. M. Ho, C. T. Chan, and C. M. Soukoulis, "Existence of photonic band gap in periodic dielectric structures," *Phys. Rev. Lett.*, vol. 65, pp. 3152–5, December 17, 1990.

[90] H. S. Sözüer and J. W. Haus, "Photonic bands: simple-cubic lattice," *J. Opt. Soc. Am. B*, vol. 10, pp. 296–302, February 1993.

[91] P. R. Villeneuve and M. Piché, "Photonic band gaps in two-dimensional square lattices: Square and circular rods," *Phys. Rev. B*, vol. 46, pp. 4973–5, August 15, 1992.

[92] A. A. Maradudin and A. R. McGurn, "Photonic band gaps in two-dimensional square lattices: square and circular rods," *Phys. Rev. B*, vol. 46, pp. 4973–5, August 15, 1992.

[93] P. R. Villeneuve and M. Piché, "Photonic band gaps in two-dimensional square and hexagonal lattices," *Phys. Rev. B*, vol. 46, pp. 4969–72, August 15, 1992.

[94] A. A. Maradudin and A. R. McGurn, "Photonic band gaps in two-dimensional square and hexagonal lattices," *Phys. Rev. B*, vol. 46, pp. 4969–72, August 15, 1992.

[95] S. L. McCall, P. M. Platzman, R. R. Dalichaouch, D. Smith, and S. Schultz, "Microwave propagation in two-dimensional dielectric lattices," *Phys. Rev. Lett.*, vol. 67, pp. 2017–20, October 7, 1991.

[96] W. M. Robertson, G. Arjavalingam, R. D. Meade, K. D. Brommer, A. M. Rappe, and J. D. Joannopoulos, "Measurement of photonic band structure in a two-dimensional periodic dielectric array," *Phys. Rev. Lett.*, vol. 68, pp. 2023–6, March 20, 1992.

[97] E. Ozbay, E. Michel, G. Tuttle, R. Biswas, K. M. Ho, J. Bostak, and D. M. Bloom, "Terahertz spectroscopy of three-dimensional photonic band-gap crystals," *Opt. Lett.*, vol. 19, pp. 1155–7, August 1, 1994.

[98] K.-M. Ho, C. T. Chan, C. M. Soukoulis, R. Biswas, and M. Sigalas, "Photonic band gaps in three dimensions: new layer-by-layer periodic structures," *Solid State Comm.*, vol. 89, pp. 413–6, February 1994.

[99] E. R. Brown, K. Agi, C. Dill, III, C. D. Parker, and K. J. Malloy, "A new face-centered-cubic photonic crystal for microwave and millimeter-wave applications," *Microwave Opt. Technol. Lett.*, vol. 7, pp. 777–9, December 5, 1994.

[100] S. Fan, P. R. Villeneuve, and J. D. Joannopoulos, "Theoretical investigation of fabrication-related disorder on the properties of photonic crystals," *J. Appl. Phys.*, vol. 78, pp. 1415–8, August 1, 1995.

[101] P. L. Gourley, J. R. Wendt, G. A. Vawter, T. M. Brennan, and B. E. Hammons, "Optical properties of two-dimensional photonic lattices fabricated as honeycomb nanostructures in compound semiconductors," *Appl. Phys. Lett.*, vol. 64, pp. 687–9, February 7, 1994.

[102] J. M. Gerard, A. Izraël, J. Y. Marzin, R. Padjen, and F. R. Ladan, "Photonic bandgap of two-dimensional dielectric crystals," *Solid-State Electronics*, vol. 37, pp. 1341–4, April-June 1994.

[103] T. Krauss, Y. P. Song, S. THoms, C. D. W. Wilkinson, and R. M. DelaRue, "Fabrication of 2-D photonic bandgap structures in GaAs/AlGaAs," *Electron. Lett.*, vol. 30, pp. 1444–6, August 18, 1994.

[104] K. Inoue, M. Wada, K. Sakoda, A. Yamanaka, M. Hayashi, and J. W. Haus, "Fabrication of two-dimensional photonic band structure with near-infrared band gap," *Jpn. J. Appl. Phys. Pt. 2*, vol. 33, pp. L1463–5, October 1994.

[105] U. Gruning, V. Lehmann, and C. Engelhardt, "Two-dimensional infrared photonic band gap structure based on porous silicon," *Appl. Phys. Lett.*, vol. 66, pp. 3254–6, June 12, 1995.

[106] A. Scherer, C. C. Cheng, E. Yablonovitch, and C. Arbet-Engels, "Fabrication of photonic bandgap structures in the optical wavelength range," in *Optical Society of America Annual Meeting* (Portland, OR), September 11–5, 1995. paper ThT3.

[107] E. Yablonovitch, T. J. Gmitter, R. D. Meade, A. M. Rappe, K. D. Brommer, and J. D. Joannopoulos, "Donor and acceptor modes in photonic band strucure," *Phys. Rev. Lett.*, vol. 67, pp. 3380–3, December 9, 1991.

[108] P. R. Villeneuve, S. Fan, J. D. Joannopoulos, K. Y. Lim, G. S. Petrich, L. A. Kolodziejski, and L. R. Reif, "Air-bridge microcavity," *Appl. Phys. Lett.*, vol. 67, pp. 167–9, July 1995.

[109] S. John, "Localization of light," *Physics Today*, vol. 44, pp. 32–40, May 1991.

[110] E. Ozbay, G. Tuttle, M. Sigalas, C. Soukoulis, and K. M. Ho, "Defect structures in a layer-by-layer photonic band-gap crystal," *Phys. Rev. B*, vol. 51, pp. 13961–5, September 15, 1995.

[111] E. Yablonovitch, "Inhibited spontaneous emission in solid-state physics and electronics," *Phys. Rev. Lett.*, vol. 58, pp. 2059–62, May 18, 1987.

[112] J. Martorell and N. M. Lawandy, "Observation of inhibited spontaneous emission in a periodic dielectric structure," *Phys. Rev. Lett.*, vol. 65, pp. 1877–80, October 8, 1990.

[113] G. Kurizki and A. Z. Genack, "Suppression of molecular interactions in periodic dielectric structures," *Phys. Rev. Lett.*, vol. 61, pp. 2269–7, November 7, 1988.

[114] A. G. Kofman, G. Kurizki, and B. Sherman, "Spontaneous and induced atomic decay in photonic band structures," *J. Mod. Optics*, vol. 41, pp. 353–84, February 1994.

[115] S. John and T. Quang, "Spontaneous emission near the edge of a photonic band gap," *Phys. Rev. A*, vol. 50, pp. 1764–9, August 1994.

[116] S. John and T. Quang, "Localization of superradiance near a photonic band gap," *Phys. Rev. Lett.*, vol. 74, pp. 3419–22, April 24. 1995.

[117] E. Yablonovitch, "Photonic band-gap structures," *J. Opt. Soc. Am. B*, vol. 10, pp. 283–95, February 1993.

[118] E. R. Brown, C. D. Parker, and E. Yablonovitch, "Radiation properties of a planar antenna on a photonic-crystal substrate," *J. Opt. Soc. Am. B*, vol. 10, pp. 404–7, February 1993.

[119] R. D. Meade, A. Devenyi, J. D. Joannopoulos, O. L. Alherhand, D. A. Smith, and K. Kash, "Novel applications of photonic band gap materials: Low loss bends and high Q cavities," *J. Appl. Phys.*, vol. 75, p. 4753, May 1994.

[120] A. Y. Cho, A. Yariv, and P. Yeh, "Observation of confined propagation in bragg waveguides," *Appl. Phys. Lett.*, vol. 30, pp. 471–2, May 1, 1977.

[121] M. A. Duguay, Y. Kokubun, T. L. Koch, and L. Pfeiffer, "Antiresonant reflecting optical waveguides in SiO_2-Si multilayer structures," *Appl. Phys. Lett.*, vol. 49, pp. 13–5, July 7, 1986.

[122] J. D. Joannopoulos, "Low loss bends in semiconductor optical waveguides for photonic integrated circuits." disclosure for M.I.T. Technology Office, July 1992.

[123] H. A. Haus and Y. Lai, "Narrow-band optical channel-dropping filter," *J. Lightwave Technol.*, vol. 10, no. 1, pp. 57–62, 1992.

[124] J. N. Damask, "A new photonic device — the integrated resonant channel-dropping filter," Master's thesis, Massachusetts Institute of Technology, Cambridge, MA, 1993.

[125] J. N. Damask, V. V. Wong, J. Ferrera, H. I. Smith, and H. A. Haus, "Optical distributed-feedback channel-dropping filters: design and fabrication," in *Proceedings of IEEE Lasers and Electro-Optics Society 1993 Annual Meeting* (San Jose, CA), pp. 355–6, November 15–8, 1993.

[126] J. N.Damask and H. A. Haus, "Wavelength-division multiplexing using channel-dropping filters," *J. Lightwave Technol.*, vol. 11, pp. 424–8, March 1993.

[127] J. N. Damask, J. Ferrera, V. V. Wong, H. I. Smith, and H. A. Haus, "Limitations and solutions for the use of integrated lambda/4-shifted distributed bragg resonators in wavelength- division multiplexing applications," in *Proceedings of the SPIE — The International Society for Optical Engineering*, vol. 2213 (Lindau, Germany), pp. 137–51, April 13–4, 1994.

[128] V. V. Wong, J. Ferrera, J. N. Damask, J. M. Carter, E. E. Moon, H. A. Haus, H. I. Smith, and S. Rishton, "Spatial-phase-locked electron-beam lithography and x-ray lithography for fabricating first-order gratings on rib," *J. Vac. Sci. Technol. B*, vol. 12, pp. 3741–5, November–December 1994.

[129] K.-Y. Lim, "The fabrication of photonic bandgap bridge resonator structure," Master's thesis, Massachusetts Institute of Technology, Cambridge, MA, 1994.

[130] P. R. Villeneuve and M. Piché, "Photonic bandgaps in periodic dielectric structures," *Prog. Quant. Electron.*, vol. 18, no. 2, pp. 153–200, 1994.

[131] Working Group 1 of COST 216, "Comparison of different modelling techniques for longitudinally invariant integrated optical waveguides," *IEE Proc. J*, vol. 136, pp. 273–280, October 1989.

[132] H. Kogelnik, "Theory of optical waveguides," in *Guided-Wave Optoelectronics* (T. Tamir, ed.), Springer-Verlag, 1990.

[133] P. Kendall, M. J. Adams, S. Richtie, and M. J. Robertson, "Theory for calculating the approximate values for the propagation constants of an optical rib waveguide by weighting the refractive indices," *IEE Proc. A*, vol. 134, pp. 699–702, September 1987.

[134] M. Ohtaka, M. Matsuhara, and N. Kumagai, "Analysis of the guided modes in slab-coupled waveguides using a variational method," *IEEE J. Quantum Electron.*, vol. QE-12, pp. 378–82, July 1976.

[135] W. P. Huang and H. A. Haus, "A simple variational approach to optical rib waveguides," *J. Lightwave Technol.*, vol. 9, pp. 56–61, January 1991.

[136] P. N. Robson and P. C. Kendall, *Rib Waveguide Theory by the Spectral Index Method.* Taunton, Somerset, England: Research Studies Press and Wiley, 1990.

[137] B. M. A. Rahman, F. A. Fernandez, and J. B. Davies, "Review of finite element methods for microwave and optical waveguides," *Proc. IEEE*, vol. 79, pp. 1442–8, October 1991.

[138] W. P. Huang, C. L. Xu, S. T. Chu, and S. K. Chaudhuri, "The finite-difference vector beam propagation method: Analysis and assessment," *J. Lightwave Technol.*, vol. 10, pp. 295–305, March 1992.

[139] C. F. Gerald and P. O. Wheatley, *Applied Numerical Analysis.* New York: Addison-Wesley, 3rd ed., 1984.

[140] D. B. Mortimore, "Wavelength-flattened fused couplers," *Electron. Lett.*, vol. 21, pp. 742–3, August 1985.

[141] A. Takagi, K. Jinguji, and M. Kawachi, "Design and fabrication of broad-band silica-based optical waveguide couplers with asymmetric structure," *IEEE J. Quantum Electon.*, vol. 28, pp. 848–55, April 1992.

[142] H. Yanagawa, S. Nakamura, I. Ohyama, and K. Ueki, "Broad-band high-silica optical waveguide star coupler with asymmetric directional coupler," *J. Lightwave Technol.*, vol. 8, pp. 1292–7, September 1990.

[143] A. Wakatsuki, K. Okamoto, and O. Mikami, "Proposed semiconductor narrow-band wavelength filter using directional couplers," *Electon. Lett.*, vol. 26, pp. 1573–5, September 1990.

[144] O. Leminger and R. Zengerle, "Narrow-band directional couplers made of dissimilar single-mode fibers with different cladding refractive indices," *J. Lightwave Technol.*, vol. 8, pp. 1289–91, September 1990.

[145] S. V. Burke, P. C. Kendall, S. Ritchie, M. J. Robertson, and P. N. Robson, "Analysis of rib waveguide coupler filters," *IEE Proc. J*, vol. 139, pp. 59–65, February 1992.

[146] J. C. Chen and C. Seo, "Application of spectral index method to laser diode design," *J. Lightwave Technol.*, April 1996, in press.

[147] E. A. J. Marcatili, "Bends in optical dielectric guides," *The Bell System Tech. J.*, vol. 48, pp. 2103–2132, September 1969.

[148] D. Marcuse, "Bending loss of the asymmetric slab waveguide," *The Bell System Tech. J.*, vol. 50, pp. 2551–61, October 1971.

[149] E.-G. Neumann, "Curved dielectric optical waveguide with reduced transition losses," *IEE Proc.*, Pt. H, vol. 129, pp. 278–30, October 1982.

[150] E.-G. Neumann, "Low loss dielectric optical waveguide bends," *Fiber and Integrated Optics*, vol. 4, no. 2, pp. 203–11, 1982.

[151] M. Majd, B. Schüppert, and K. Petermann, "Low-loss Ti:$LiNbO_3$-waveguide bends prepared by MgO indiffusion," *J. Lightwave Technol.*, vol. 8, pp. 1670–4, November 1990.

[152] J. Yamauchi, M. Ikegaya, and H. Nakano, "Bend loss of step-index slab waveguides with a trench section," *Microwave and Optical Tech. Lett.*, vol. 5, pp. 251–4, June 1992.

[153] M. K. Smit, E. C. M. Pennings, and H. Blok, "A normalized approach to the design of low-loss optical waveguide bends," *J. Lightwave Technol.*, vol. 11, pp. 1737–42, November 1993.

[154] J. C. Chen and C. Seo, "Novel reduction of losses in bent waveguides," in *Optical Society of America Annual Meeting Technical Digest* (Dallas, TX), October 2-7, 1994. paper ThFF3.

[155] P. P. Lagasse, G. Franssens, P. Kaczmarski, H. Nolting, C. Weinert, N. Baken, H. Bastiaansen, J. van der Tol, E. E. Pennings, G. Krijnen, H. H. Hoekstra, T. Popma, A. Tervonen, O. Leminger, G. Zesch, J. Gu, R. Taylor, D. Robbins, J. Buus, I. Croston, D. Catzula, A. Galtarossa, C. Someda, M. Potenza, J. Gerdes, and R. Pregla, "COST-216 comparative study of S-bend and directional coupler analysis methods," in *ECOC 90: 16th European Conference on Optical Communication* (Amsterdam, Netherlands), pp. 175–8, September 16–20, 1990.

[156] M. Heiblum and J. H. Harris, "Analysis of curved optical waveguides by conformal transformation," *IEEE J. Quantum Electron.*, vol. QE-11, pp. 75–83, February 1975.

[157] R. Baets and P. E. Lagasse, "Loss calculation and design of arbitrarily curved integrated-optic waveguides," *J. Opt. Soc. Am.*, vol. 73, pp. 177–82, February 1983.

[158] J. Saijonmaa and D. Yevick, "Beam-propagation analysis of loss in bent optical waveguides and fibers," *J. Opt. Soc. Am.*, vol. 73, pp. 1785–91, December 1983.

[159] P. S. Martin, J. C. Chen, C. G. Fonstad, and H. A. Haus, "Application of spectral index method to laser diode design," *J. Lightwave Technol.*, vol. 13, pp. 569–74, April 1995.

[160] M. Sigalas, C. M. Soukoulis, E. N. Economou, C. T. Chan, and K. M. Ho, "Photonic band gaps and defects in two dimensions: Studies of the transmission coefficient," *Phys. Rev. B.*, vol. 48, pp. 121–6, November 1993.

[161] J. W. Haus, "A brief review of theoretical results for photonic band structure," *J. Mod. Optics*, vol. 41, no. 2, pp. 195–207, 1994.

[162] H. A. Haus, "Distributed feedback structures," in *Waves and Fields in Optoelectronics*, Englewood Cliffs, NJ: Prentice-Hall, Inc., 1984.

[163] H. A. Haus, "The radiation Q of open photonic-gap bridge resonators." internal RLE memo, 1994.

[164] A. T. Perlik, T. Opsahl, and A. Taflove, "Predicting scattering of electromagnetic fields using FD-TD on a Connection Machine," *IEEE Trans. Magnetics*, vol. 25, pp. 2910–2, July 1989.

[165] A. T. Perlik and S. C. Moraites, "Electromagnetic wave analysis using FD-TD and its implementation on the Connection Machine," in *PIER 7: Computational Electromagnetics and Supercomputer Architecture* (T. Cwik and J. Patterson, eds.), Cambridge, MA: EMW Publishing, 1993.

[166] D. B. Davidson and R. W. Ziolkowski, "A connection machine (CM-2) implementation of a three-dimensional parallel finite difference time-domain code for

electromagnetic field simulation," *Int. J. of Numerical Modelling: Electronic Networks, Devices and Fields*, vol. 8, pp. 221–32, May–August 1995.

[167] W. H. Weedon, W. C. Chew, and C. M. Rappaport, "Computationally efficient FDTD simulation of open-region scattering problems on the Connection Machine CM-5," in *IEEE Antennas and Propagat. Soc. Int. Symposium*, vol. 1 (Seattle, WA), pp. 376–379, June 1994.

[168] Z. Bi, K. Wu, C. Wu, and J. Litva, "A dispersive boundary condition for microstrip component analysis using the FD-TD method," *IEEE Trans. Microwave Theory Tech.*, vol. 40, pp. 774–7, April 1992.

[169] C. J. Railton, E. M. Daniel, D.-L. Paul, and J. P. McGeehan, "Optimized absorbing boundary conditions for the analysis of planar circuits using the finite difference time domain method," *IEEE Trans. Microwave Theory Tech.*, vol. 41, pp. 290–7, February 1993.

[170] K. Naishadham and X. P. Lin, "Application of spectral domain Prony's method to the FDTD analysis of planar microstrip circuits," *IEEE Trans. Microwave Theory Tech.*, vol. 42, pp. 2391–8, December 1994.

[171] C. Wu, E. A. Narro, P. Y. Chung, and J. Litva, "Modeling of waveguide structures using the nonorthogonal FDTD method with a PML absorbing boundary," *Microwave Opt. Technol. Lett.*, vol. 8, pp. 226–8, March 1995.

[172] Ü. Pekel and R. Mittra, "A finite-element-method frequency-domain application of the perflectly matched layer (PML) concept," *Microwave Opt. Technol. Lett.*, vol. 9, pp. 117–22, June 1995.

[173] W. V. Andrew, C. A. Balanis, and P. A. Tirkas, "A comparison of Berenger Perfectly Matched Layer and the Lindman higher-order ABC's for the FDTD method," *IEEE Microwave Guided Wave Lett.*, vol. 5, pp. 192–4, June 1995.

[174] P. R. Villeneuve, S. Fan, J. D. Joannopoulos, K.-Y. Lim, J. C. Chen, G. S. Petrich, L. A. Kolodziejski, and R. Reif, "Microcavities in channel waveguides,"

in *Proceedings of a NATO Advanced Studies Institute on Photonic Band Gap Materials* (Elounda, Greece), May 26–30, 1995.

[175] S. Fan, "How to calculate transmission for 3D FDTD." private communication, January 1995.

[176] J. N. Winn, "Dynamic studies of photonic crystals," Master's thesis, Massachusetts Institute of Technology, Cambridge, MA, 1994.

[177] C. Vassallo, *Optical Waveguide Concepts.* Amsterdam: Elsevier, 1991.

[178] D. Gilly and the staff of O'Reilly & Associates, Inc., *UNIX in a Nutshell: System V Edition: A Desktop Quick Reference.* Sebastopol, CA: O'Reilly & Associates, 2nd ed., 1992.